Interactions Between Nanoparticles and Biological Charged Lines: Biological Mimics of Protein-DNA Complexes and Microtubules as Drug Targets

by

Erika N. Cline

A dissertation submitted in partial fulfillment
of the requirements for the degree of
Doctor of Philosophy
(Cellular and Molecular Biology)
in The University of Michigan
2013

Doctoral Committee:

Professor Nils G. Walter, Chair
Assistant Professor Julie S. Biteen
Professor David R. Engelke
Professor Ronald G. Larson
Professor Edgar Meyhöfer

For my grandparents, Jack & Shirley Cline and George & Wilma Landon;

my parents, Bob & Debbie Cline;

and my wife, Stephanie.

ACKNOWLEDGEMENTS

I would like to thank my advisor Nils Walter, for all of the guidance he has provided me over the years. The past and present members of the Walter lab for their help with experiments and for making the lab an enjoyable place to work. The past and present members of our EFRI collaboration, especially Ron Larson and Shi Yu for many helpful discussions, Ming-Hsin Li and Seok Ki Choi for synthesis and modification of many different nanoparticles utilized in this dissertation, and Ashwin Panday and other members of the Guo lab for much help with nanofabrication. The members of my dissertation committee for their guidance. Jeff Herbstman and Min Su of the Skiniotis lab for training in TEM. The members of the Meyhöfer lab—Jenna Campbell, Charles Chang Jiang, and Neha Kaul—for supplying tubulin and the knowledge to work with it. And finally, the creators of this LaTex template, for making my life a whole lot easier.

TABLE OF CONTENTS

LIST OF FIGURES

Figure

LIST OF APPENDICES

Appendix

LIST OF ABBREVIATIONS

λ linear charge density or bacteriophage lambda

σ surface charge density

1D one-dimensional

2D two-dimensional

3D three-dimensional

AuNPs gold nanoparticles

CH_2Cl_2 methylene chloride

Cy Cy5 Cyanine dye

DI deionized

DIG digoxygenin

DMAET 2-dimethylaminoethanethiol

DMAP 4-dimethylaminopyridine

DMF dimethylformamide

DTT dithiothreitol

EDC 1-ethyl-3-(3-dimethylaminopropyl) carbodiimide hydrochloride

EGTA Ethylene glycol tetraacetic acid

ESI electrospray ionization

FIONA fluorescence imaging with one nanometer accuracy

FRET fluorescence resonance energy transfer

G3 generation 3

G5 generation 5

GMPCPP GpCpp

GPC gel permeation chromatography

GSH glutathione

GTP guanosine triphosphate

H_3PO_4 phosphoric acid

HRMS high-resolution mass spectrometry

LMV large multilamellar vesicle

MAPs microtubule-associated proteins

MeOH methanol

MES 2-(*N*-morpholino)ethanesulfonic acid

$MgCl_2$ magnesium chloride

MHz megahertz

MS mass spectrometry

MSD mean square displacement

MTs microtubules

MWCO molecular weight cut off

$NaHCO_3$ sodium bicarbonate

NaOH sodium hydroxide

NHS N-hydroxysuccinimide

NMR nuclear magnetic resonance

OSS oxygen scavenging system

PAMAM polyamidoamine

PBS phosphate buffered saline

PCA protocatechuate acid

PCD protocatechuate-3,4-dioxygenase

PDE Phosphodiesterase I

PDI polydispersity index

PX paclitaxel

QDs quantum dots

SMRT single-molecule, real-time

TEA triethylamine

TEM transmission electron microscopy

TIRFM total internal reflection fluorescence microscopy

TLC thin-layer chromatography

TMR 5-(6)-carboxytetramethylrhodamine succimidyl ester

Tub tubulin

UPLC ultra performance liquid chromatography

ZMWs zero-mode waveguides

ZP zeta potential

ABSTRACT

Interactions Between Nanoparticles and Biological Charged Lines: Biological Mimics of Protein-DNA Complexes and Microtubules as Drug Targets

by

Erika N. Cline

Chair: Nils G. Walter

DNA-binding proteins use a combination of the following mechanisms to find their DNA target sites: "hopping" or "jumping" along DNA (3D diffusion), intersegment transfer, sliding (1D diffusion), and site-specific recognition. In particular, the process of sliding is not well understood. It has been hypothesized that while sliding, proteins are "loosely" associated with DNA via electrostatic interactions between cationic residues on the protein and anionic phosphate groups on the DNA backbone. To test this hypothesis, a biomimetic model of sliding was created in which the protein was replaced with cationic particles and the DNA with anionic "linear" molecules. The model system utilized in this dissertation was a nanoparticle-microtubule system. Microtubules were chosen because like DNA, they are "linear", negatively-charged biopolymers. Using total internal reflection fluorescence microscopy (TIRFM), it was found that aggregated cationic particles can slide along microtubules. Accordingly, it was hypothesized that the roughened surface of the aggregates mimics the protein conformation complementarity occurring in the cell, and that this complementarity

and the juxtaposition of cationic residues within the protein's DNA binding pocket are crucial to protein sliding.

Next, specific binding site recognition was incorporated into the model based on paclitaxel. Paclitaxel is known to bind microtubules and hyperstabilize them. For this cytotoxic property, it is marketed as an anti-cancer drug, although it causes detrimental side effects due to its water insolubility and promiscuity. Accordingly, testing the microtubule binding properties of the paclitaxel-conjugated nanoparticles was of interest. Using TIRFM and transmission electron microscopy (TEM), it was found that paclitaxel-conjugated G5 PAMAM dendrimers affect microtubules by: (1) promoting polymerization; (2) stabilizing microtubules; and (3) bundling microtubules. The latter is independent of paclitaxel and due instead to a combination of electrostatic interactions involving protonatable amines in the dendrimer core, and hydrophobic interactions between the fluorescent labels on the dendrimer (Cy5) and tubulin (TMR). These results warrant further investigation into the toxicity of the cationic dendrimer core before further consideration as paclitaxel delivery platforms. Finally, it is demonstrated that paclitaxel-conjugated gold nanoparticles also show promise as targeted delivery platforms as they polymerize, stabilize, and bundle microtubules in a paclitaxel-dependent manner.

CHAPTER I

A Journey Towards Modeling Protein Sliding Along DNA: A Logical Detour into Microtubules as Drug Targets

1.1 Introduction

DNA-binding proteins play important roles in regulating and driving gene expression, a crucial cellular function. In the cell, it is often necessary for the level of RNA or protein expression to be quickly altered, requiring DNA-binding proteins to rapidly locate their specific binding (target) sites. However, this is no trivial task for the protein. Consider a human cell, which packs $\approx$ 3 billion base pairs ($\approx$ 1 m of linear DNA)[1] into a nucleus which is on the order of 10 μm in diameter.[2] In contrast, a protein's DNA target site is on the scale of nanometers, which creates daunting thermodynamic and kinetic challenges for the protein to overcome while locating its target site.

Given that proteins are able to locate their target sites *in vivo* 100 times faster than the diffusion limit predicted by theory (this prediction reflects only the time taken to arrive at the target site, not recognize it; recognition would take even more time), and 1000 times faster than the DNA-protein association rates measured *in vitro*,[3] it is apparent that DNA-binding proteins employ mechanisms other than

three-dimensional (3D) diffusion to locate their target sites. However, the exact mechanisms employed by these proteins to rapidly locate their target sites are not yet fully understood.

1.2 Target Site Search Mechanisms Employed by DNA-Binding Proteins

DNA-binding proteins employ a combination of the following mechanisms to locate their target sites (Figure 1.1): hopping (3D diffusion: protein randomly collides with DNA, dissociates if not at target site, and reassociates close by), jumping (3D diffusion: same as hopping but reassociation is far from site of dissociation) intersegment transfer (between segments of DNA brought close by looping, etc.), sliding (one-dimensional (1D) diffusion), and finally, target site recognition.[4–6] This dissertation will focus on the mechanisms of sliding and target site recognition.

Sliding serves to increase the probability of the protein finding its target site by restricting the normal 3D Brownian diffusion of the protein in the cytoplasm to one dimension along the DNA. Consequently, this allows the protein to sample more than one small area on the DNA each time it comes into contact with the DNA. However, this 1D diffusion along DNA is not sufficiently fast for a single protein to locate the target site quickly enough if rapid response times are required by the cell.[6] Accordingly, it has been hypothesized that the cell regulates the copy number of proteins per cell based on the response time needed. Based on the copy number, the proteins will either be more likely to locate their target site using 3D diffusion (if the copy number is high), or 1D diffusion (if the copy number is low).[7] This does not imply that a protein will exclusively find its target search using one method based on its copy number, only that the probability of the protein finding its target site utilizing one method or the other increases.

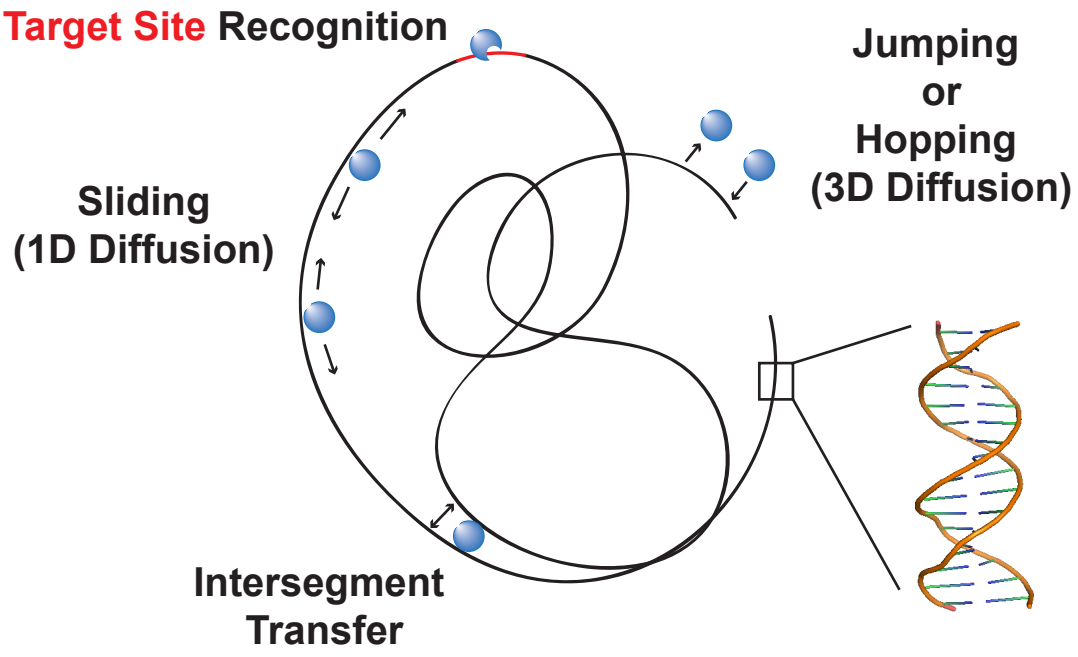

Figure 1.1: DNA target site search mechanisms employed by DNA-binding proteins

1D diffusion of various DNA-binding proteins has been observed using various single-molecule microscopy techniques *in vitro*[8–12] as well as *in vivo*.[13] However, it is still not entirely understood how 1D diffusion occurs. In order for a DNA-binding protein to diffuse in 1D along DNA, it must be associated with the DNA tightly enough to sense the DNA bases, but loosely enough to move rapidly along the DNA. This loose association is thought to be primarily mediated by electrostatic interactions between cationic residues on the protein and anionic charges on the phosphates groups of the DNA.[14,15] In support of this hypothesis, it has been observed that an increase in salt concentration correlates with a decrease in protein sliding *in vitro*.[5,8,16,17] Once the protein reaches its target site, it strongly interacts with the bases of the target site that "match" residues in the protein's DNA-binding site *via* hydrogen bonds, hydrophobic interactions, and water-mediated interactions.[18] By contrast to the salt dependence of the non-specific interactions mediating sliding, target site recognition is not significantly dependent on salt concentration.[19,20]

If sliding is indeed primarily mediated by electrostatics, then it should be possible to synthetically model this process with charged components of the approximate size and shape of the protein and DNA (Figure 1.2). If a cationic nanoparticle (acting as the protein analog) is able to slide along an anionic nanoline (acting as the DNA analog) at rates comparable to those observed for proteins sliding along DNA (see for example[8–12]), this would be compelling evidence that the biological process of a DNA-binding protein sliding along DNA is driven by electrostatics. Furthermore, this would enable precise determination of the charge densities, sizes, and shapes of the individual components required for sliding to occur. In addition, such artificial biosensing and actuation models have great promise for myriad future biomedical applications.[21]

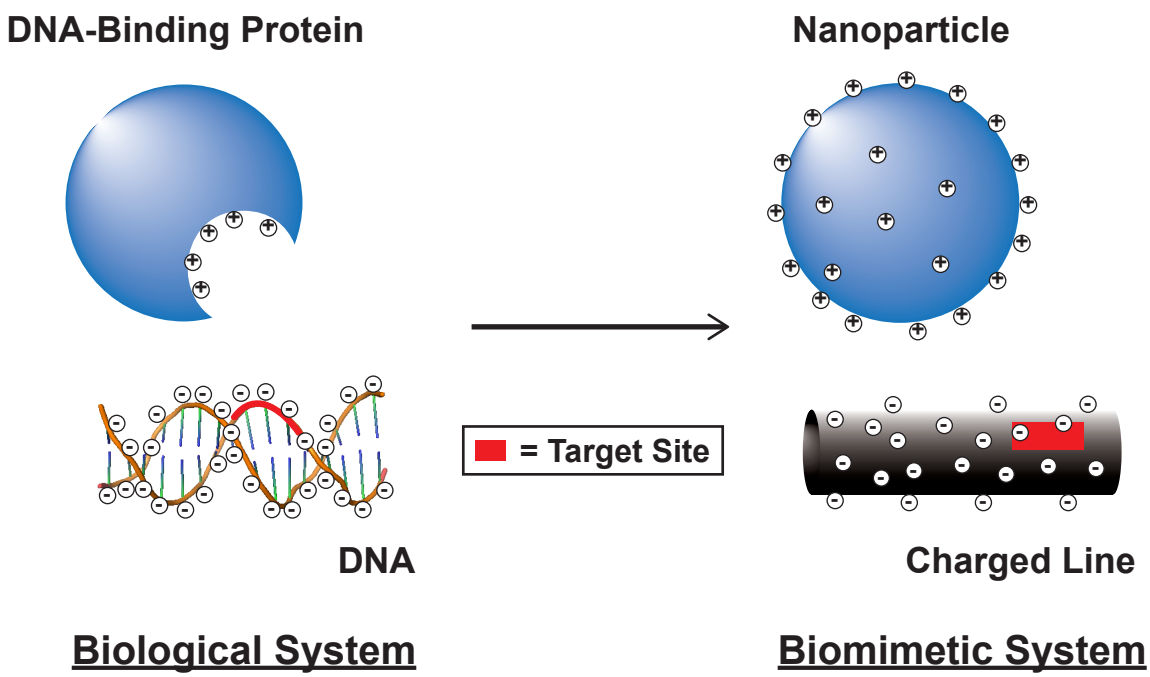

Figure 1.2: Biomimetic model of DNA-binding proteins. DNA-binding proteins are replaced with cationic nanoparticles of comparable size and DNA is replaced with anionic nanolines. A target site may also be engineered onto the nanoline to study target site recognition.

1.3 Steps Towards Modeling Protein Sliding Along DNA

While there are many examples of directed diffusion that exploit various chemical and physical phenomena,[22] no synthetic model of random diffusion driven entirely by electrostatics has been demonstrated to date. Since developing an entirely synthetic model is a considerable step above the entirely biological system, a logical first step would be to replace either the protein or the DNA with a synthetic or biologic analog, while using the natural biological form of the other component.

Nanoparticles are good candidates for protein mimics as their size, shape, charge density, and other surface properties can be well controlled during synthesis. Both inorganic[23] and organic particles may be suitable for this function. For example, the organic polymeric PAMAM dendrimers have already shown promise as mimics of histones.[24] While there are no known examples of electrostatically-driven nanoparticle diffusion along DNA, there is, however, at least one demonstration in the literature of electrostatically-driven nanoparticle diffusion along microtubules. This study shows that polystyrene nanoparticles carrying high cationic surface charges are able to slide along microtubules, and furthermore, the surface charge density affects the diffusion coefficient and duration of microtuble interaction.[25]

Microtubules may be considered electrostatic analogs of DNA as both can be reduced to negatively charged "linear" biopolymers (Figure 1.3). Due to their negative charge, microtubules would provide opportunities for electrostatic interactions with cationic nanoparticles. However, as microtubules are composed of protein and not nucleic acid, they would provide no specific DNA sequence information, making it possible to study the effect of electrostatics on DNA-binding protein movement independent of DNA sequence information.

Although DNA and microtubules are both approximately "linear" and negatively charged, there are a few obvious structural and chemical differences that must be considered. First, microtubules are much greater in diameter than DNA (Figure 1.3).

Therefore if cationic nanoparticles are able to slide along microtubules, they may slide in a two-dimensional (2D) trajectory rather than a 1D trajectory. However, it should be noted that DNA-binding proteins have also been observed to slide along DNA in two dimensions when encountering obstacles on the DNA.[26] Next, because microtubules are cylindrical in structure and not helical, the nanoparticles will likely not slide along the microtubules in a helical manner like proteins do along DNA.[26–28] Finally, microtubules have a lower linear charge density than DNA by $\approx$ 24-fold. In spite of these structural and chemical difference between microtubules and DNA, an observation of nanoparticles (with cationic surface charge densities comparable to DNA-binding proteins) sliding along microtubules (at rates comparable to 1D diffusion coefficients of DNA-binding proteins sliding along DNA) would still support the hypothesis that electrostatics play a significant role in protein sliding. While there are many other options for biologic or synthetic analogs of both proteins and DNA, this dissertation will focus on the utilization of nanoparticles as protein analogs, and microtubules as DNA analogs.

1.4 Using Paclitaxel to Specifically Target Nanoparticles to Microtubules

An important component of the search of DNA-binding proteins for their target site on the DNA is the target site itself. Therefore, a complete model of protein sliding would also incorporate a target site onto the DNA analog. As microtubules are biological molecules, they contain natural target sites for other naturally occurring molecules. Paclitaxel is one example of a naturally occurring microtubule binding molecule. It is known to bind in a 1:1 ratio to the β-subunit of tubulin dimers in the microtubule lumen (Figure 1.4).

Paclitaxel binding hyperstabilizes microtubules against depolymerization, which

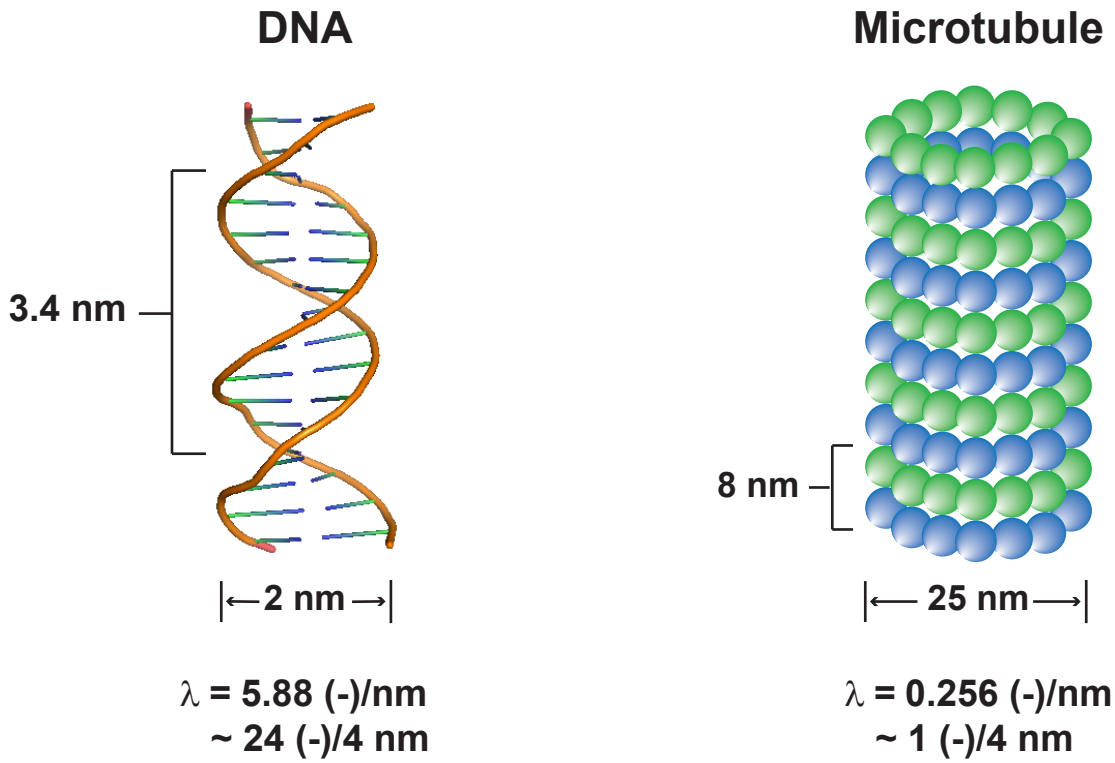

Figure 1.3: Comparison of the dimensions and linear charge densities (λ) of DNA and microtubules

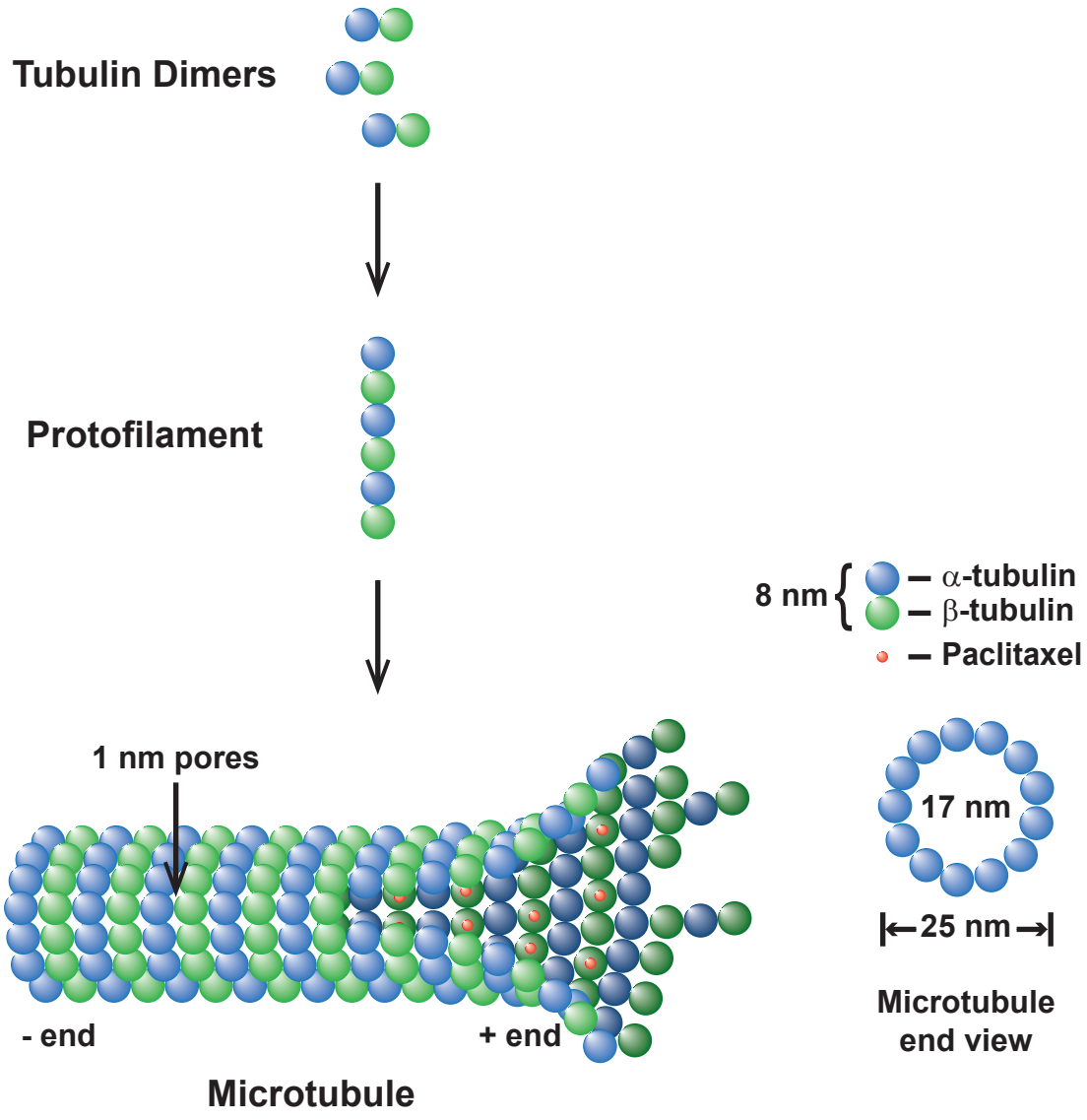

Figure 1.4: Microtubule polymerization, structure, and the paclitaxel binding sites on β-tubulin. Paclitaxel can bind microtubules at a 1:1 ratio with tubulin dimers, but is illustrated here at a lower concentration than the dimers.

in vivo, arrests cell division, particularly of rapidly dividing cells.[29] It is because of these cytotoxic properties that paclitaxel is marketed as an anti-cancer drug (Taxol®, Bristol-Myers Squibb, New York, NY). Therefore, targeting nanoparticles to microtubules with paclitaxel may also be of interest as a potential targeted drug delivery strategy. Indeed there is great interest in developing a targeted delivery strategy for paclitaxel. Paclitaxel has been proven a successful cancer drug on its own,[29] however it currently causes detrimental side effects in patients. This is partly due to the fact that paclitaxel is poorly water soluble and consequentally, is currently solubilized in a mixture of polyethoxylated castor oil and ethanol prior to injection into the patient.[30] These toxic solubilizing agents, along with the promiscuous cytotoxicity of paclitaxel and the fact that it has a high binding affinity for plasma proteins, are reasons that paclitaxel causes detrimental side effects and decreased drug efficiency.[30] Accordingly, numerous targeted delivery strategies for paclitaxel that aim to overcome its limitations are currently being explored experimentally and in clinical trials.[30–32]

1.5 Thesis Objectives

The overall goal that inspired this dissertation was to develop a synthetic mimic of protein sliding along DNA, in order to learn more about the physicochemical properties driving this important biological process. The first objective of this dissertation describes one of the initial steps taken towards this goal, in which nanoparticles were utilized as protein analogs and microtubules as DNA analogs. As a next step, paclitaxel was used to specifically target the nanoparticles to the microtubules, in order to mimic the specific interaction between DNA-binding proteins and their target sites. Due to the cytotoxic nature of paclitaxel, this naturally lead to the second objective of this dissertation, the investigation of the suitability of these paclitaxel-conjugated nanoparticles as a targeted cancer drug delivery strategy. One finding from this investigation was that the core of the chosen nanoparticle, the G5 PAMAM dendrimer,

induces bundling of microtubules, even when it is not conjugated with paclitaxel. This finding leads to the final two objectives of this dissertation: (1) an investigation of the suitability of paclitaxel-conjugated gold nanoparticles as a targeted cancer drug delivery platform; and (2) an investigation of the properties of G5 PAMAM dendrimers that induce microtubule bundling.

CHAPTER II

Towards Developing a Biosynthetic Mimic of the Target Site Search Employed by DNA-Binding Proteins[1]

2.1 Introduction

DNA-binding proteins play many important roles in the cell, including regulating and driving gene expression. The subset of DNA-binding proteins that bind specific (target) sites on the DNA have a daunting task in finding their site among the vast amount of DNA compacted in the cell. An early confirmation that the cell has some mechanism(s) to overcome the apparent thermodynamic and kinetic obstacles involved in the protein's target site search was the observation that one DNA-binding protein, the lac-repressor, was able to locate its target site faster than the diffusion limit would predict if the protein utilized three-dimensional (3D) diffusion alone.[33] It has since been established that DNA-binding proteins employ a combination of search mechanisms to increase the efficiency of their search (Figure 1.1): intradomain association and dissociation (3D diffusion or "hopping"), intersegment transfer (hopping between close DNA segments), and sliding (one-dimensional (1D) diffusion).[4,5]

[1]All tubulin was obtained from Edgar Meyhöfer. All modification and characterization of dendrimers and polystyrene particles was done by Ming-Hsin Li. The polyacrylamide particles were synthesized by Ming Qin. The QDs were synthesized by Seung-Ho Jung.

Sliding increases the efficiency of the protein's search by restricting the normal 3D Brownian diffusion of the protein in the cytoplasm to one dimension along the DNA.

Although 1D diffusion of various DNA-binding proteins has been observed by single-molecule techniques *in vitro*[8–12] and *in vivo*,[13] it is still not entirely understood how this process occurs. Theoretically, in order for a DNA-binding protein to locate its target site by sliding along DNA, it must be associated loosely enough to move rapidly, but tightly enough to sense the sequences it is passing over. This loose association is thought to be provided by electrostatic interactions between cationic residues on the protein and anionic charges on the phosphates groups of the DNA.[14,15] Indeed, it has been observed *in vitro* that an increase in salt concentration correlates with a decrease in protein sliding.[5,8,16,17]

The primary objective that inspired this dissertation was to confirm that sliding is primarily mediated by electrostatics by creating a synthetic model of this process using charged components of the approximate size and shape of the protein and DNA. If a cationic nanoparticle (acting as the protein analog) is able to slide along an anionic nanoline (acting as the DNA analog), this would be compelling evidence that the biological process of a DNA-binding protein sliding along DNA is driven by electrostatics. Furthermore, this would enable precise determination of the charge densities, sizes, and shapes of the individual components required for sliding to occur. While there are many examples of directed diffusion that exploit various chemical and physical phenomena,[22] no synthetic model of random diffusion driven entirely by electrostatics has been demonstrated in the literature to date.

Since developing such a model is a considerable step above the entirely biological system, the current study takes a preliminary step by replacing the protein with a synthetic analog, but the DNA with a biological analog. The synthetic protein analogs chosen for this study are nanoparticles and the biological DNA analogs chosen are microtubules. Nanoparticles were chosen as protein mimics because their size,

shape, charge density, and other surface properties can be well controlled during synthesis. Microtubules were chosen as electrostatic DNA analogs as both are "linear" biopolymers with negative surface charges. Microtubules would provide opportunities for van der Waals and electrostatic interactions with cationic nanoparticles, but no specific DNA sequence information. In fact, there is already one example in the literature of cationic nanoparticles sliding along microtubules.[25]

The overall aim of the current study was to characterize the contribution of nanoparticle material, size, and charge density to nanoparticle kinetics of sliding along microtubules. First, we tested the ability of cationic polyacrylamide particles to slide along microtubules. When it became apparent that the polyacrylamide particles tested did not carry a high enough charge density to exhibit prolonged association with microtubules, polystyrene particles with a higher charge density were tested. Preliminary results show that these highly cationic polystyrene particles are indeed able to slide along microtubules, but only when significantly aggregated to obtain a diameter $\approx$ 40 times greater. Finally, in order to more closely model the protein searching process, two different nanoparticles closer in size to DNA-binding proteins ($\approx$ 5 nm) were tested for the ability to slide along microtubules. First, inorganic nanoparticles—DMAET-stabilized CdHgTe quantum dots (QDs)—were tested.[23] Like the polyacrylamide particles, these particles did not carry a high enough charge density to exhibit any prolonged interactions with microtubules. Next, organic nanoparticles—generation 5 (G5) polyamidoamine (PAMAM) dendrimers—were tested. Ideally, these particles have 128 end groups which can be easily modified through chemical reactions. This enables the charge density of the particles to be very precisely altered, from a neutral surface charge density to a very high surface charge density. At the time that this dissertation was written, no dendrimer sliding along microtubules has been observed with the conditions and dendrimer charge densities tested, however, many dendrimer-microtubule binding interactions were ob-

served with high cationic charge densities and high dendrimer concentrations.

2.2 Materials and Methods

Materials

2-(*N*-morpholino)ethanesulfonic acid (MES), magnesium chloride ($MgCl_2$), and guanosine triphosphate (GTP) were all purchased from Fisher Scientific (Waltham, MA). Ethylene glycol tetraacetic acid (EGTA), paclitaxel, protocatechuate acid (PCA), protocatechuate-3,4-dioxygenase (PCD), and 3-methacryloxylpropyltrimethoxysilane from Sigma-Aldrich (St. Louis, MO); Trolox from Acros Organics (Geel, Belgium); 5-(6)-carboxytetramethylrhodamine succimidyl ester (TMR) from Molecular Probes (Eugene, OR); and Cy5 Cyanine dye (Cy) succimidyl ester from GE Healthcare Life Sciences (Piscataway Township, NJ).

Tubulin Purification and Polymerization

Tubulin was purified from bovine brain and fluorescently labeled with TMR by Neha Kaul, Jenna Campbell, and Charles Chang Jiang in Edgar Meyhöfer's lab. Briefly, tubulin was purified from bovine brain by two cycles of microtubule polymerization in the presence of a high-molarity PIPES buffer.[34] Tubulin was TMR-labeled by reacting polymerized microtubules with a 20-fold excess of TMR at room temperature for 30 min. Competent, TMR-labeled tubulin was purified from this mixture by repeated depolymerization and polymerization.[35]

For all experiments, microtubules were polymerized by incubating 2 mg/mL ($\approx$ 20 μM) α/β-tubulin dimers (using a mix of TMR-labeled and unlabeled tubulin dimers to achieve a final ratio of 1 TMR dye per 20 dimers, as determined by UV-Vis, where noted) with 4 mM $MgCl_2$ and 1 mM GTP in $MEM80_{6.8}$ buffer (80 mM MES-KOH, pH 6.8, 1 mM EGTA, 2 mM $MgCl_2$) at 37 °C for 30 min. After polymerization, the

microtubules were stabilized with 10 μM paclitaxel.

TIRFM

Imaging chambers were prepared by affixing a cover glass (No. 1.5, 24x30 mm, VWR, Radnor, PA) to a glass slide (Fischer Scientific, Waltham, MA) with double-sided sticky tape. After the imaging solution was flown into the imaging channel, the channel was sealed with candle wax. Images were taken on an inverted fluorescence microscope (model IX81, Olympus, Center Valley, PA) using a 60x objective lens. Samples were illuminated at either 532 nm (for TMR; type Compass 315M, Coherent Inc., Santa Clara, CA) or 635 nm (for Cy5; type Cube 640-100C, Coherent Inc., Santa Clara, CA) at the critical angle, using a cellˆ TIRF^{TM} Illuminator (Olympus, Center Valley, PA). Fluorescent emissions were split into four separate channels using a QV2 Quad View Imaging System (Photometrics, Tuscon, AZ) and projected onto an EMCCD camera (model Evolve 512, Photometrics, Tuscon, AZ). Fluorescent images were viewed using MetaMorph software (Molecular Devices, Sunnyvale, CA) and further processed using either ImageJ (NIH) and/or MATLAB (The MathWorks, Inc., Natick, MA).

Polyacrylamide Nanoparticles

The polyacrylamide nanoparticles used in this study were synthesized, and kindly provided by, Ming Qin, member of Raoul Kopelman's lab at the University of Michigan. Two distinct batches were provided: (1) 38 $\pm$ 10 nm particles with surface charge density σ = 0.05 (+)/nm^2; and (2) 80 nm particles (standard deviation of diameter unknown) with σ = 0.03 (+)/nm^2 as determined by Ming Qin using zeta potential (ZP) measurement. Both batches were labeled with methylene blue to enable fluorescent detection.[36] These particles will be referred to throughout the text as PAA38 or PAA80, respectively, according to their diameters. When it became

apparent that these particles were not charged enough to interact with microtubules, an attempt was made to increase the particle charge density of PAA38. This was done with the help of Ming-Hsin Li and Seok-Ki Choi, members of James R. Baker's lab, formerly of the University of Michigan, using the amination methods of Minoura *et al.*[25] which utilize ethylenediamine. However, zeta potential measurement showed that the result of this amination reaction was an aggregated population of particles (the particle diameter increased from 38 ± 5 nm to 100 ± 7 nm) with a zeta potential measurement of -5 ± 3 mV, likely implying that particles with charge densities both positive and negative are present, resulting in an average charge density close to 0 (neutral).

Probing for Co-localization of Polyacrylamide Nanoparticles and Microtubules by TIRFM

TMR-labeled, paclitaxel-stabilized microtubules were polymerized and stabilized as described above (see section Tubulin purification and polymerization). These microtubules were flowed into a slide imaging channel at 0.3 μM tubulin. After allowing the microtubules 10 min to fall to the coverslip surface, the tubulin remaining in solution was washed away using 3 flow channel volumes of MEM30 (30 mM MES, pH 6.8, 0.3 mM $MgCl_2$, 25 mM KCl, 0.003% NP40) containing OSS and 10 μM paclitaxel. Then 3 fM of either (1) PAA38; or (2) PAA80 and oxygen scavenging system (OSS; 5 mM PCA, 50 nM PCD, 2 mM Trolox) were flowed into the imaging channel in $MEM80_{6.8}$ at room temperature. The mixture was then visualized by TIRFM. All coverslips used for these experiments were spin-coated with polystyrene prior to attachment to the microscope slide by Shi Yu, member of Ron Larson's lab at the University of Michigan.

Polystyrene Nanoparticles

50 ± 5 nm, amine-terminated, polystyrene particles were purchased from Sigma-Aldrich (St Louis, MO). The charge density of these particles, $\sigma = 0.13$ (+)/nm^2, was determined by Ming-Hsin Li, member of James R. Baker's lab, formerly of the University of Michigan, using zeta potential measurement. Ming-Hsin Li also labeled these particles with, on average, 5-6 Cy5 dyes per particle to enable detection by TIRFM. These particles will be referred to as Cy-PS throughout the text.

Co-localization of Cy-PS and Microtubules by TIRFM

TMR-labeled, paclitaxel-stabilized microtubules were polymerized and stabilized as described above (see section Tubulin purification and polymerization). These microtubules were flowed into a slide imaging channel at 0.3 μM tubulin. After allowing the microtubules 10 min to fall to the coverslip surface, the tubulin remaining in solution was washed away using 3 flow channel volumes of MEM30 containing OSS and 10 μM paclitaxel. Then 1 nM of Cy-PS was added to the imaging channel in MEM30 containing OSS and 10 μM paclitaxel. The resulting mixture was then visualized by TIRFM.

Particle Tracking

Particle tracking was done with the help of Anthony Manzo, former member of Nils Walter's lab, using his custom MATLAB scripts for FIONA (fluorescence imaging with one nanometer accuracy) particle tracking. Briefly, the position of a particle relative to its first detected position was extracted over time by fitting the diffraction-limited point-spread function of the particles in a 5-min sequence of TIRFM images (time resolution 0.1 s) to two-dimensional Gaussians with a precision of 10-30 nm.[37]

DMAET-stabilized Quantum Dots

2-dimethylaminoethanethiol (DMAET)-stabilized quantum dots (QDs) were synthesized by Seung-Ho Jung, former member of Nick Kotov's lab at the University of Michigan. These particles were determined to be 4.3 nm in diameter (standard deviation unknown) with a surface charge of $\sigma = .09$ (+)/nm^2 by Seung-Ho using zeta potential measurement. These particles will be referred to as DMAET-QDs throughout the text.

Probing for Co-localization of DMAET-QDs and Microtubules by TIRFM

TMR-labeled, paclitaxel-stabilized microtubules were polymerized and stabilized as described above (see section Tubulin purification and polymerization). These microtubules were flowed into a slide imaging channel at 0.3 μM tubulin. After allowing the microtubules 10 min to fall to the coverslip surface, the tubulin remaining in solution was washed away using 3 flow channel volumes of MEM30, MEM80$_{6.8}$, or 0.1-1 M Tris (pH 8.0 with HCl), where noted, containing OSS and 10 μM paclitaxel. Then DMAET-QDs were flowed into the imaging channel in MEM30, MEM80$_{6.8}$, or 0.1-1 M Tris (pH 8.0 with HCl), where noted, containing OSS and 10 μM paclitaxel. The DMAET-QDs were titrated to a final concentration of 3 pM-1.67 μM over multiple experiments. The mixtures were visualized by TIRFM.

G5 PAMAM Dendrimers

G5 PAMAM dendrimers were purchased from Dendritech, Inc. (Midland, MI). All modification, purification, and characterization of these dendrimers was done by Ming-Hsin Li, member of James R. Baker's lab, formerly at the University of Michigan. The dendrimers were first purified using a 10 kDa molecular weight cut off (MWCO) dialysis membrane, achieving a relatively monodisperse population (polydispersity index (PDI) = 1.01–1.05, determined by gel permeation chromatogra-

phy (GPC)).[38] The average number of primary amine end groups was determined to be 114 by potentiometric titration after purification by dialysis, membrane filtration, and lyophilization.[39] These dendrimers were then reacted with 5 molar equivalents of Cy5 NHS-ester to achieve an average of 2-3 Cy5 molecules per dendrimer, as determined by ^{1}H NMR and UV-Vis. These particles will be referred to as $(NH_2)_{114}$-G5 throughout the text, according to their surface chemistry and stoichiometry.

Co-localization of $(NH_2)_{114}$-G5 and Microtubules by TIRFM

TMR-labeled, paclitaxel-stabilized microtubules were polymerized and stabilized as described above (see section 'Tubulin Purification and Polymerization'). These microtubules were flowed into a slide imaging channel at 0.3 μM tubulin. After allowing the microtubules 10 min to fall to the coverslip surface, the tubulin remaining in solution was washed away using 3 flow channel volumes of MEM30 containing OSS and 10 μM paclitaxel. Then G5 PAMAM dendrimers were flowed into the imaging channel in MEM30, or $MEM80_{6.8}$ where noted, containing OSS and 10 μM paclitaxel. The dendrimers were titrated to a final concentration of 10pM-100 nM over multiple experiments. The mixtures were visualized by TIRFM.

Alternatively, the microtubules (at 0.3 μM tubulin) and 1.67 μM dendrimers were pre-mixed in $MEM80_{6.8}$ with OSS and 10 μM paclitaxel. This mixture was then flowed into the imaging channel and visualized by TIRFM.

2.3 Results and Discussion

38 and 80 nm Polyacrylamide Particles Do Not Slide Along Microtubules

To probe for co-localization of PAA38 and PAA80 with microtubules, a similar protocol to that reported in the literature[25] was used, except that the coverslips were spin-coated with polystyrene (done by Shi Yu, Ron Larson's lab, Department of

Chemical Engineering, University of Michigan) instead of treating with silane to block particle binding to the surface. Now following the published protocol, microtubules in $MEM80_{6.8}$ were flown into a slide imaging channel, incubated for 10 min to allow the microtubules to fall to the coverslip surface, rinsed away any tubulin in solution with MEM30, and flowed 3 fM of either PAA38 or PAA80 into the imaging channel before visualizing by TIRFM.

Figure 2.1 shows a few particles of either PAA38 (Figure 2.1a) or PAA80 (Figure 2.1b) co-localizing with microtubules. However, many more particles of both PAA38 and PAA80 are bound to the slide surface. Because so many more particles are bound to the slide surface than the microtubules, it cannot be said that there is any significant interaction observed between the polyacrylamide particles and the microtubules. Recall that these particles had surface charge densities of 0.05 (+)/nm^2 or 0.03 (+)/nm^2, respectively. These charge densities may not be sufficient for interaction with microtubules as it has previously been reported in the literature that polyacrylamide particles of similar size cannot significantly interact with microtubules until their surface charge densities reach $\approx$ 3.3 (+)/nm^2.[25] Accordingly, it was next attempted to increase the cationic charge density of the particles using the same amination reaction used in the aforementioned study to increase the surface cationic charge density of polyacrylamide particles.[25]

In order to increase the cationic surface density of their polyacrylamide nanopaticles, Minoura *et al.*[25] reacted the particles with ethylenediamine for 1.3-7 h. Using the same protocol, PAA38 was reacted with ethylenediamine for 4.5 h.[25] After this reaction, zeta potential measurements showed that the particles had aggregated (their diameter increased from 38 $\pm$ 10 nm to 100 $\pm$ 7 nm). This aggregated population gave a zeta potential measurement of -5 $\pm$ 3 mV, likely implying that particles with charge densities both positive and negative are present, resulting in an average charge density close to 0 (neutral). After this, particles of different materials were tested.

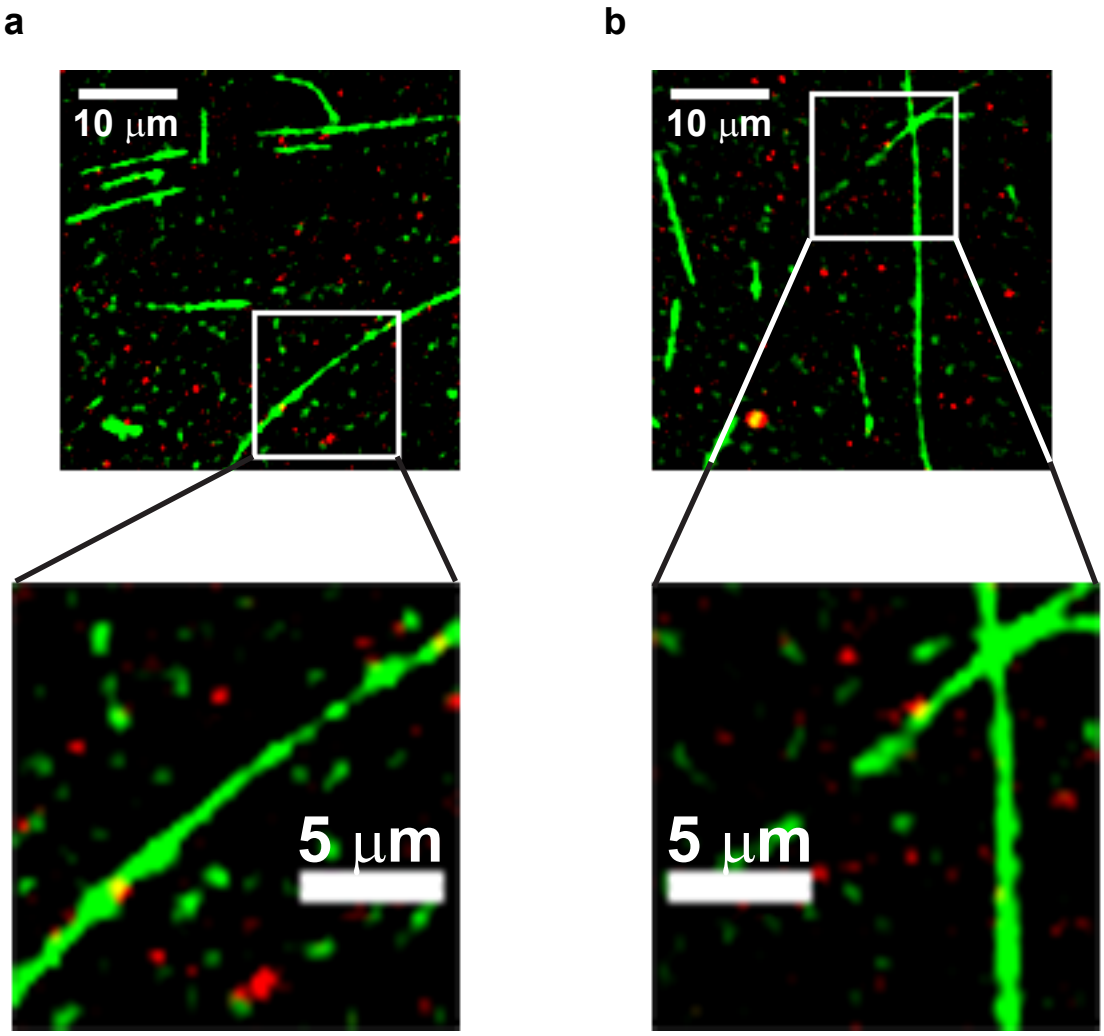

Figure 2.1: 3 fM of (a) PAA38 or (b) PAA80 with microtubules visualized by TIRFM. Images from the TMR channel (green: microtubules) are overlaid onto images from the Cy5 channel (red: polyacrylamide particles). Scale bars shown in top images are 10 μm; those in the bottom zoomed in images are 5 μm. The majority of particles from both populations were primarily observed bound to the coverslip surface.

Polystyrene Nanoparticles Slide Along Microtubules

Next, amine-terminated polystrene nanoparticles were purchased from Sigma-Aldrich. These particles were 50 nm in diameter with a surface charge density of $\sigma = 0.13$ (+)/nm^2, as determined by zeta potential measurement. After purchase, these particles were labeled, on average, with 5-6 Cy5 dyes per particle by Ming-Hsin Li, member of James R. Baker's lab, formerly at the University of Michigan. According to their fluorescent label, these particles will be referred to as Cy-PS throughout the text. These particles do not carry the high charge density previously reported as necessary for interaction between cationic polyacrylamide particles and microtubules,[25] however, polystyrene is more hydrophobic than polyacrylamide (Figure 2.2) and thus will provide additional opportunities for interactions with microtubules.

In order to probe for co-localization between Cy-PS and microtubules, the same protocol was followed as described for the polacrylamide particles above, with the exception that the coverslips were not treated with polystyrene or any other blocking material, and the Cy-PS concentration used was 1 nM. A few Cy-PS particles—$\approx 6\%$ of the population observed—not only co-localized with microtubules, but seemingly slid along them. Figure 2.3 shows one example of an apparently sliding particle. This particle is outlined with a white box in Figure 2.3a. The movement of this particle was tracked using a FIONA (fluorescence imaging with one nanometer accuracy) particle tracking MATLAB routine written by Anthony Manzo.[37] Figure 2.3b shows a plot of the particle's displacement in the y-direction vs. the x-direction relative to the location of the microtubule axis, which was estimated in ImageJ (NIH) by tracing the path of the microtubule with a line segment and recording the angle of the segment with respect to the x-axis. This angle was then used to generate a line equation for plot Figure 2.3b. This plot shows that the particle's overall trajectory closes follows the microtubule axis. Furthermore, while the particle's trajectory is mostly one-dimensional, it is also two-dimensional for some time intervals. Figure 2.3c shows a

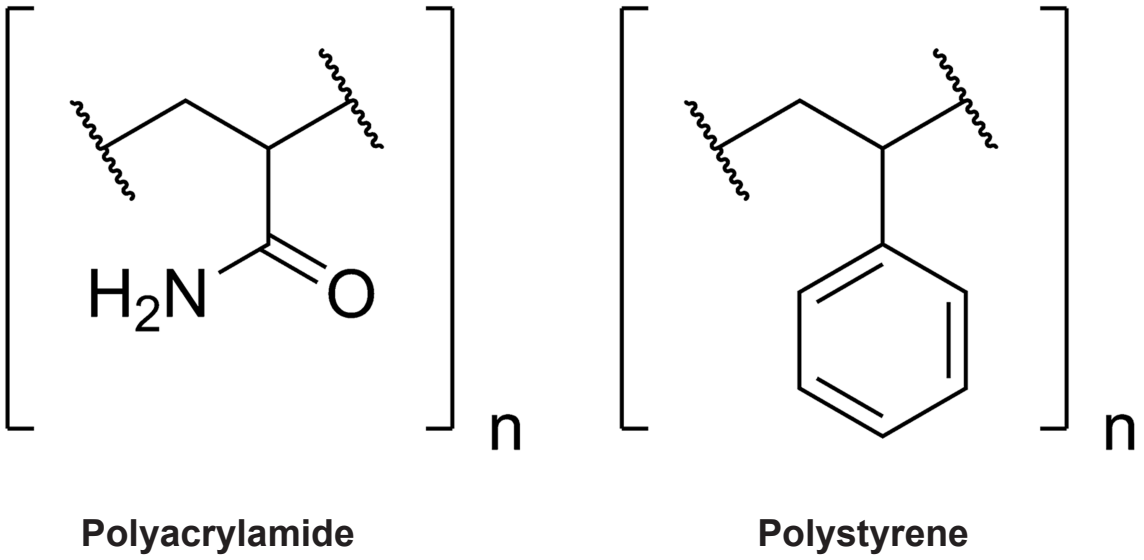

Figure 2.2: Chemical structures of polyacrylamide and polystyrene. The polystyrene nanoparticles used in this study were amine-terminated by Sigma-Aldrich (St. Louis, MO); the final chemical structure is not published by the manufacturer.

histogram of the distances the particle traveled in 100 ms intervals. A Gaussian fit of these data shows that the mean distance traveled by the particle while electrostatically trapped by the microtubule is 0.44 μm/s. Figure 2.3d shows the mean square displacement (MSD) of the particle's trajectory as a function of time. Error bars represent the standard deviation of the MSD, $\sigma = \sqrt{((2Di\Delta t)^2(2i^2+1)/3i(N-i+1))}$.[10] The first 1.5 s of the trajectory were fit with the allometric equation, $MSD = a + (2^n D) * t^c$, where a = offset, D = diffusion coefficient, n = dimensionality of diffusion, t = time lag, and c = coefficient characterizing diffusion. The coefficient of determination for the fit was $R^2 = 0.98$.

From the fit, many parameters can be extracted that will give information about the particle's trajectory. The parameter c is 1.04, indicating the particle underwent Brownian diffusion.[40–42] In addition, the coefficient of determination is equal ($R^2 = 0.98$) whether the parameter n is fixed at 1 (1D diffusion) or 2 (2D diffusion). Considering the plot in Figure 2.3b, and the large diameter of microtubules which would theoretically allow 2D diffusion, it is assumed that the particle underwent 2D diffusion. Under this assumption, a diffusion coefficient of 2.12×10^{-9} cm^2/s is calculated. From this diffusion coefficient, the diameter of the particle is estimated to be 2 μm using the Stokes-Einstein equation $D = \frac{k_B T}{6\pi\eta r}$, where k_B is Boltzmann's constant, T is temperature, η is viscosity, and r is particle radius. If the particle is truly 2 μm in diameter, it is larger than the diffraction limit of light ($\approx$ 266 nm), and its diameter can be measured directly from the fluorescent image. Indeed, a cross-sectional line plot made in ImageJ (NIH) estimates the particle diameter to be $\approx$ 1 μm.

However, these diameter measurements are significantly greater than 50 nm, the particle diameter stated by the manufacturer and confirmed in-house by zeta potential measurement. This discrepancy could be due to either calculation error or particle aggregation. Nevertheless, the measured diffusion coefficients are close to those measured by Minoura *et al.*[25] for polyacrylamide particles of a comparable size

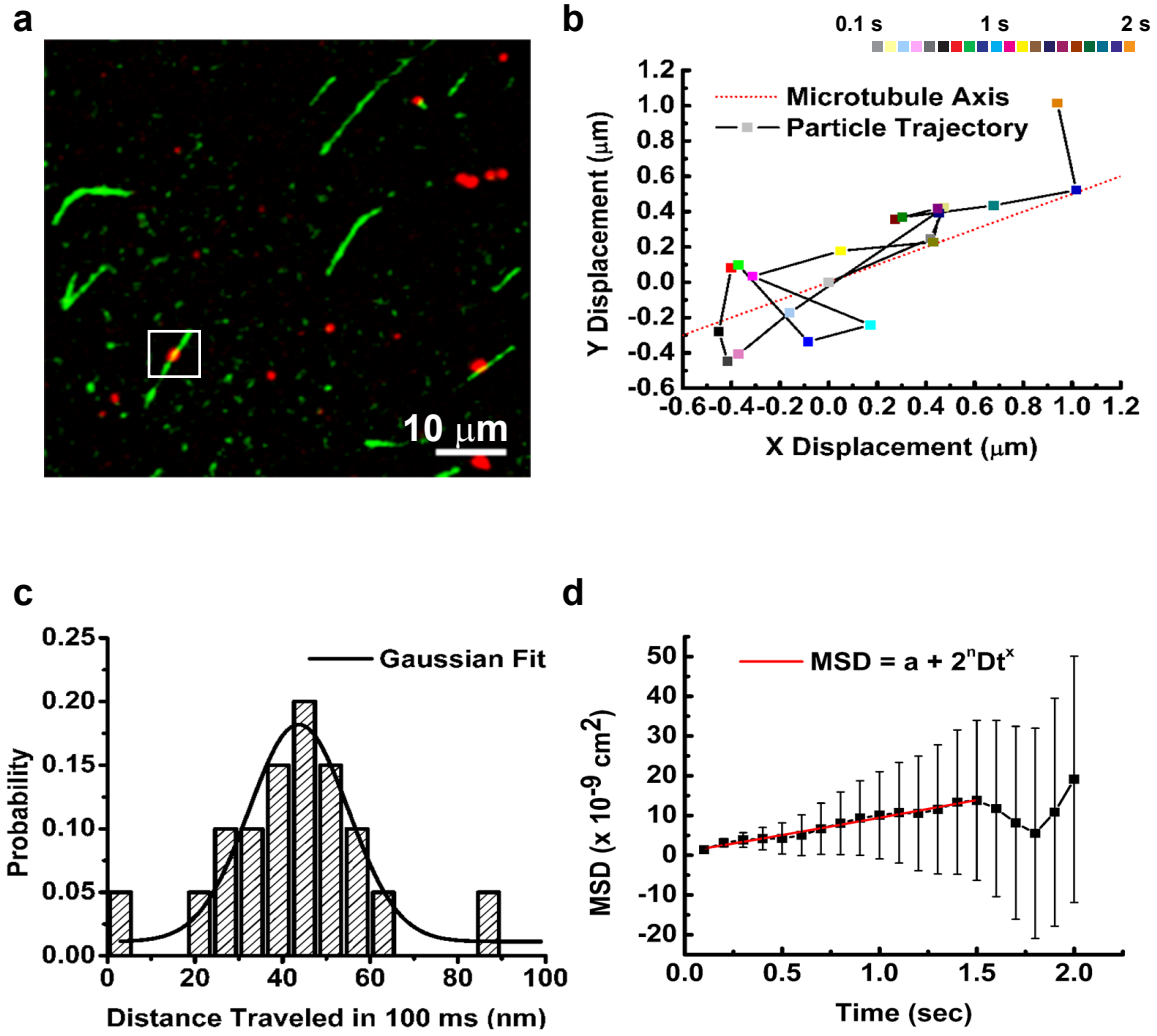

Figure 2.3: (a) 1 nM of Cy-PS with microtubules visualized by TIRFM. Images from the TMR channel (green: microtubules) are overlaid onto images from the Cy5 channel (red: Cy-PS). Scale bar shown is 10 μm. The particle indicated by the white box was analyzed using a FIONA (fluorescence imaging with one nanometer accuracy) particle tracking routine. (b) A plot of the particle's displacement in the y- vs. x-direction relative to the microtubule axis (red dotted line). (c) A histogram of the distances the particle traveled in 100 ms intervals overlaid by a Gaussian fit ($R^2 = 0.89$). The time-color scale is shown above the plot. (d) MSD of the particle's trajectory as a function of time. Error bars represent the standard deviation of the MSD, $\sigma = \sqrt{((2Di\Delta t)^2(2i^2+1)/3i(N-i+1))}$. The first 1.5 s of the trajectory were fit with an allometric equation ($MSD = a + (2^n D) * t^c$) with $R^2 = 0.98$ and parameter $c = 1.04$.

(57 nm): 8.9×10^{-9} cm^2/s. Albeit, these polyacrylamide particles had a much higher charge density than Cy-PS, 3.3 (+)/nm^2 compared to 0.13 (+)/nm^2.

To test if these particles were indeed aggregated, the experiment was repeated except the Cy-PS sample was vigorously vortexed prior to addition to the imaging channel. Figure 2.4 shows that vortexing results in particles that appear much smaller than those observed without vortexing (Figure 2.3). In addition, a higher apparent particle density is observed in Figure 2.4 compared to Figure 2.3 even though the same particle concentration was used for both experiments. This is compelling evidence that the Cy-PS particle observed to slide along microtubules in Figure 2.3 was aggregated. Since there was no obvious sliding observed with the vortexed particles, this implies that the higher number of cationic charges afforded by the aggregates allowed the prolonged microtubule association observed.

Overall, these data suggests that a cationic charge density ≤ 0.13 (+)/nm^2 is not sufficient for prolonged interaction with microtubules. However, when the number of charges available to interact with the microtubule is significantly increased—through particle aggregation, for example—prolonged association is possible. In one instance, the Brownian diffusion of a Cy-PS aggregate was confined (for 2 $\pm$ 0.1 s) to less than three dimensions by a microtubule, likely through electrostatic attraction. The distinction between the observed 2D diffusion of this particle, and the observed 1D diffusion of proteins along DNA,[8–12] can be explained by the larger diameter of microtubules (25 vs. 2 nm), which allows sufficient dimensionality for the particle to undergo 2D diffusion. In order to confirm this observation, additional testing must be done. In addition, the diameter extracted from the 3D diffusion coefficient of these particles in solution should be compared to those determined by confined diffusion along microtubules.

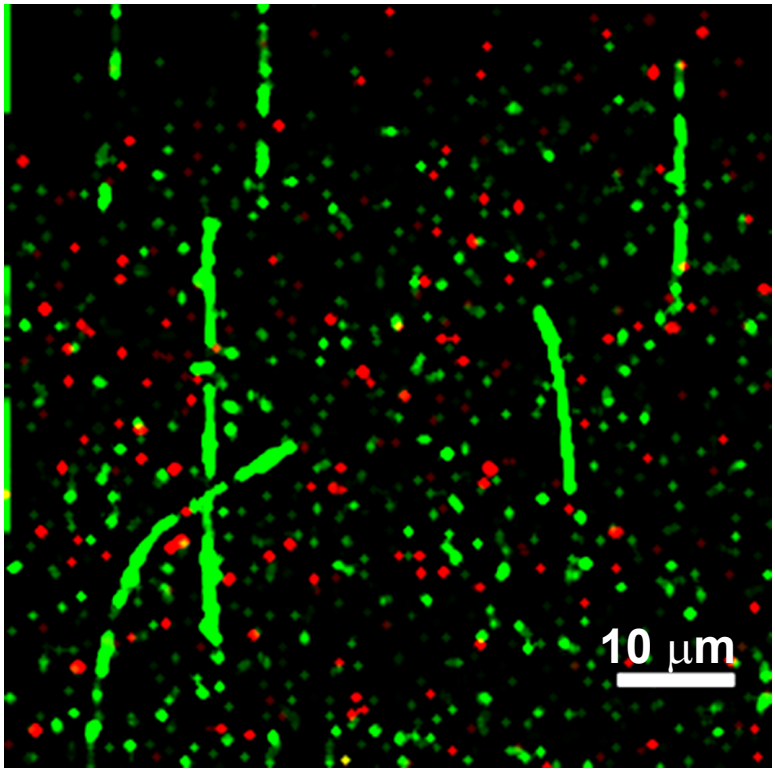

Figure 2.4: 1 nM of Cy-PS were vigorously vortexed before being introduced into an imaging channel already containing microtubules. The resulting mixtures were visualized by TIRFM. Images from the TMR channel (green: microtubules) are overlaid onto images from the Cy5 channel (red: Cy-PS). Scale bar shown is 10 μm.

DMAET-Stabilized Quantum Dots Do Not Significantly Interact with Microtubules

Next, particles with smaller diameters more comparable to those of DNA-binding proteins were texted. Inorganic nanoparticles are theoretically good candidates for protein mimics[23] and, therefore, cationic quantum dots were tested for an ability to slide along microtubules. To this end, 2-dimethylaminoethanethiol (DMAET)-stabilized CdHgTe quantum dots (QDs)—hereafter referred to as DMAET-QDs—were kindly provided by the Kotov lab at the University of Michigan, which were synthesized by Seung-Ho Jung. These particles were determined to be 4.3 nm in diameter with a charge density of 0.3 (+)/nm^2 by zeta potential measurement. This charge density is slightly higher than that of the polyacrylamide (0.04 (+)/nm^2) and polystyrene (0.13 (+)/nm^2) particles tested above. The chemical structure of DMAET is shown in Figure 2.5 for comparison to that of polyacrylamide and polystyrene (Figure 2.2).

TIRFM co-localization experiments were performed exactly as those with the polyacrylamide or polystyrene particles, except that in addition to MEM30, MEM80$_{6.8}$ and 0.1-1 M Tris, were also tested as visualization buffers. DMAET-QDs were imaged in these buffers at a final concentration of 3 pM-1.67 μM, over multiple experiments. Although some co-localization of the particles and the microtubules was observed (Figure 2.6), it did not appear significantly greater than the binding of the particles to the slide surface at any concentration tested.

Considering all particles tested thus far, the only particle that exhibited potential sliding along microtubules was Cy-PS. While all particles tested had relatively low cationic charge densities—ranging from 0.03-0.3 (+)/nm^2—compared to the minimum particle charge density required for significant microtubule association, as determined by Minoura *et al.*,[25] Cy-PS aggregates did exhibit sliding along microtubules. From the diffusion coefficient of this particle, a very large diameter was calculated using the Stokes-Einstein equation, 1-2 μm. This would drastically increase the number

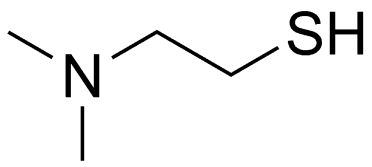

Figure 2.5: Chemical structure of 2-dimethylaminoethanethiol (DMAET), which is used to stabilize the quantum dots (QDs) used in this study.

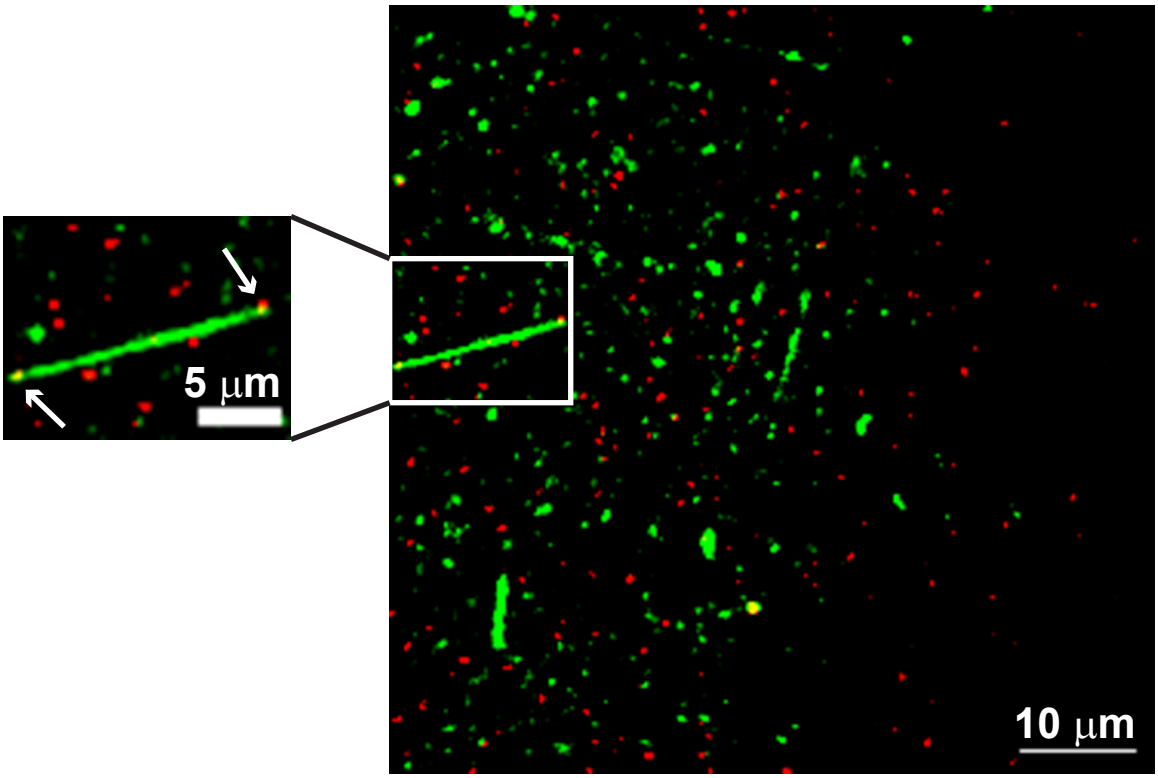

Figure 2.6: 3 pM of DMAET-stabilized CdHgTe QDs with microtubules in 500 mM Tris (pH 8.0) visualized by TIRFM. Images from the TMR channel (green: microtubules) are overlaid onto images from the Cy5 channel (red: QDs). A zoomed in area of interest containing potential sites of co-localization in the image on the right is shown on the left. Sites of co-localization are indicated by white arrows.

of cationic charges available for interaction with the microtubule, although the exact number of cationic charges is not known. Since the particle aggregation was not controlled, even if the charge density of the aggregates was determined from their zeta potential, this would likely result in a wide distribution of particle sizes and charge densities. Therefore, single particles with higher charge densities must be tested for microtubule interaction in order to concisely determine, or confirm,[25] charge density limits for interaction with microtubules.

Highly Cationic G5 PAMAM Dendrimers Interact with Microtubules

The higher charged particles chosen to test were generation 5 (G5) polyamidoamine (PAMAM) dendrimers. Due to the highly branched nature of these organic polymers, the fifth generation particles carry 128 chemically reactive end groups per 5.4 nm particle,[43,44] if formed perfectly. This large number of reaction sites on the surface of the particle makes possible two things important for our purposes: (1) the particle can carry a high cationic surface charge (up to 1.4 (+)/nm^2); and (2) the surface charge on the particles can be very precisely covalently altered, resulting in a wide range of testable charge densities possible for the same particle. Considering that the maximum cationic charge density carried by the G5 PAMAM dendrimer is 1.4 (+)/nm^2, it is a little surprising that Minoura *et al.*[25] were able to achieve 9.4 (+)/nm^2. Nevertheless, it was tested if G5 PAMAM dendrimers carried enough cationic charge to interact, and/or slide along, microtubules.

The batch of G5 PAMAM dendrimers used in this study had 114 terminal [primary] amine groups on average, as determined by potentiometric titration. This results in a cationic charge density of 1.2 (+)/nm^2. According to their chemistry and stoichiometry, these dendrimers will hereafter be referred to as $(NH_2)_{114}$-G5. To test for co-localization between $(NH_2)_{114}$-G5 and microtubules, the same protocol was used as throughout this study, using a final concentration of $(NH_2)_{114}$-G5 of 10

pM-100 nM in MEM30, over multiple experiments.

Similar to all other particles tested (with the exception of the Cy-PS aggregate), there were no significant interactions observed between the dendrimers and the microtubules. However, when the experimental conditions were changed so that the dendrimers were first mixed with the microtubules prior to addition to the imaging chamber, and a much higher dendrimer concentration was used (1.67 μM), significant dendrimer binding to microtubules was observed. Figure 2.7 shows a few examples of dendrimer-bound microtubules. This is in contrast to all other particles tested in that no significant co-localization events were detected whether the particles and microtubules were pre-mixed before introduction into the imaging chamber, or whether the microtubules were first allowed to bind the coverslip surface before the particles were introduced into the imaging chamber. A white box on the leftmost image outlines a dendrimer-bound microtubule. The TMR (tubulin) fluorescence from this microtubule cannot be seen, but this is likely due to fluorescence resonance energy transfer (FRET) between the TMR label on the tubulin and the Cy5 label on the dendrimers. In the rightmost image, some microtubules are observed with a few instances of co-localization with the dendrimers. In the future, G5 PAMAM dendrimers with lower charge densities should be tested for an ability to bind to microtubules, in order to determine a lower charge density limit for microtubule binding.

Conclusions

In conclusion, particles with cationic charge densities of $\leq$ 1.2 (+)/nm^2 do not seem to significantly interact with microtubules, especially at sub-μM particle concentrations. These results are consistent with those of Minoura *et al.*,[25] who found that particles with cationic charge densities less than 3.3 (+)/nm^2 cannot associate with microtubules. However, aggregated polystyrene particles with a single particle charge density of 0.13 (+)/nm^2 were observed to undergo 2D Brownian diffusion

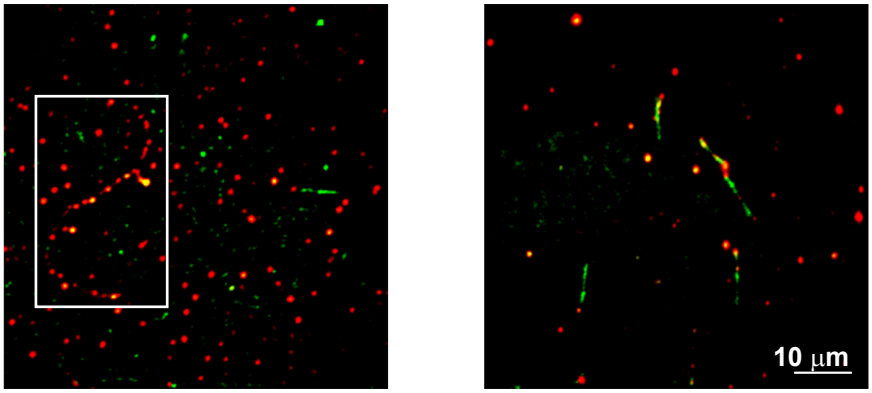

Figure 2.7: 1.67 μM of $(NH_2)_{114}$-G5 with microtubules in $MEM80_{6.8}$, visualized by TIRFM. Images from the TMR channel (green: microtubules) are overlaid onto images from the Cy5 channel (red: dendrimers). Scale bar shown is 10 μm. The two images are taken under the same experimental conditions. The white box on the left image outlines a dendrimer-bound microtubule.

along microtubules (Figure 2.3). When the same particle sample was instead vigorously vortexed prior to mixing with the microtubules, no sliding along, or association with, microtubules was observed. This implies that many more cationic charges must be available for microtubule interaction than those supplied by particles with charge densities of ≤ 1.2 (+)/nm^2.

Considering the implication of these results for the protein-DNA system, DNA-binding (or microtubule-binding) proteins do not have the high charge densities seemingly required by synthetic nanoparticles to interact with, and slide along, microtubules. For example, T7 RNA polymerase has a cationic charge density of 0.057 (+)/nm^2. However, the cationic charges of DNA-binding proteins are primarily concentrated in their DNA-binding domains, which may serve to dramatically increase the local cationic surface charge density of the protein. At this time, there have been no calculations reported in the literature to determine the local surface charge density of DNA-binding proteins, to my knowledge. If the local charge densities of the DNA-binding domains of proteins do not reach those determined to be necessary for synthetic nanoparticles *in vitro*, then this may imply that other interactions in addition to electrostatics are required for non-specific binding to, and sliding of, proteins along DNA. However, the organic nanoparticles tested in this study were actually able to provide some of these alternative interaction opportunities with microtubules other than electrostatic. Therefore, it may be that the shape complementarity of the protein to the DNA, and the charge juxtaposition within the DNA binding pocket of the protein, are very important components of the protein-DNA interactions mediating sliding.[14,45,46] Indeed, it is possible that the reason that some of the polystyrene particle aggregates were able to slide along microtubules when many were not, is that the presumably rough surface of these aggregates may have become, by chance, complementary in shape to the microtubules, as depicted in the model schematic shown in Figure 2.8.

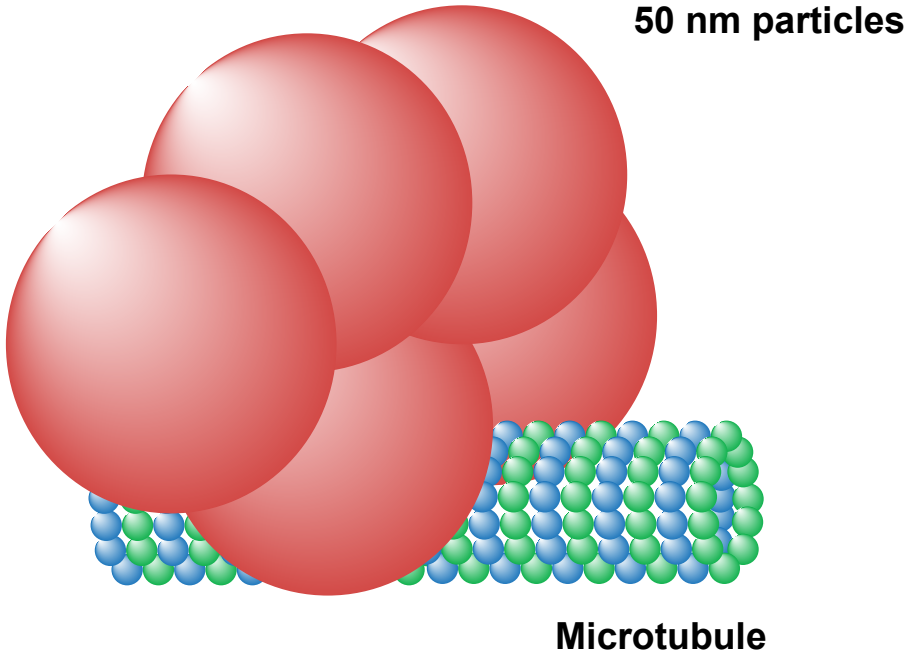

Figure 2.8: Model of particle aggregate shape complementarity with microtubules. 50 nm polystyrene particles, depicted as red spheres, are shown to form an aggregate that has a pocket of the right size to fit around a microtubule, depicted as a cylindrical polymer of blue and green spheres. The shape complementarity of this pocket, randomly formed through particle aggregate, may allow these cationic aggregated particles to slide along microtubules.

CHAPTER III

Paclitaxel-Conjugated PAMAM Dendrimers Adversely Affect Microtubule Structure through Two Independent Modes of Action[1]

3.1 Introduction

Paclitaxel is a small organic molecule that is marketed as an anti-cancer drug (Taxol®, Bristol-Myers Squibb, New York, NY; Figure 3.1) because of its cytotoxic properties that derive from its ability to hyperstabilize microtubules against depolymerization and, consequently, arrest cell division, particularly of rapidly dividing cells.[29] Since paclitaxel is poorly water soluble, it is currently solubilized in a mixture of polyethoxylated castor oil and ethanol prior to injection into the patient.[30] These toxic solubilizing agents, the promiscuous cytotoxicity of paclitaxel, and the fact that paclitaxel has a high binding affinity for plasma proteins, lead to detrimental side effects and decreased drug efficiency.[30] Nevertheless, paclitaxel has proven to be a successful cancer drug,[29] making the design of a targeted delivery strategy using a water-soluble form of paclitaxel very desirable.

Numerous targeted delivery strategies for paclitaxel that aim to overcome its lim-

[1]Adapted with permission from Cline, E.N.; Li, M-H; Choi, S.K.; Herbstman, J.F.; Kaul, N.; Meyhöfer, E.; Skiniotis, G.; Baker, J.R.; Larson, R.G.; Walter, N.G. *Biomacromolecules* **2013**, 14, 654-664.

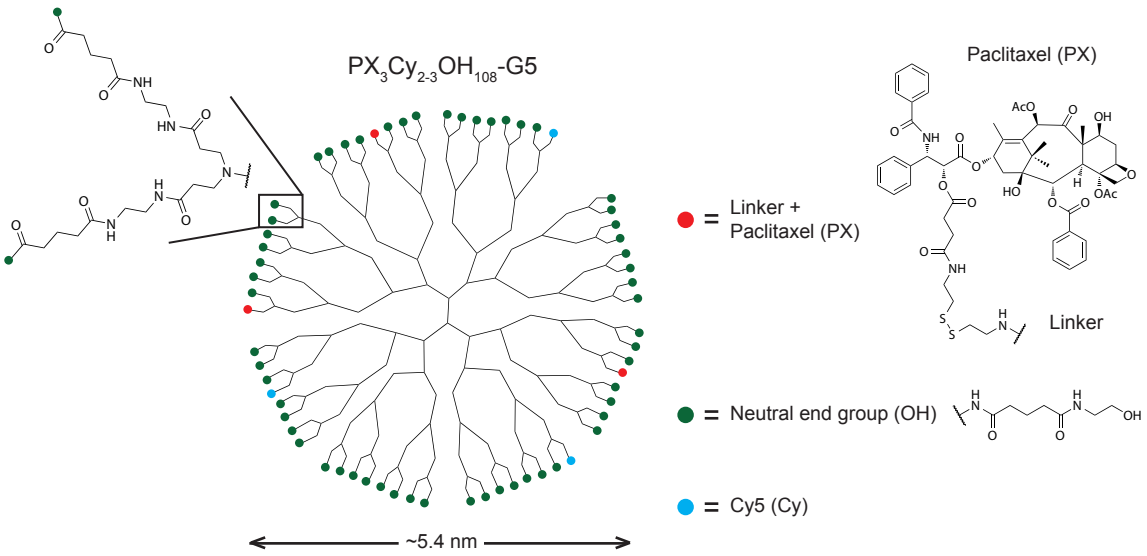

Figure 3.1: Two-dimensional schematic of the fifth generation (G5), paclitaxel (PX)-conjugated PAMAM dendrimer used in this study (systematically termed $PX_3Cy_{2-3}OH_{108}$-G5 by its chemical composition). The theoretical number of terminal branches per G5 dendrimer is 128, but only a fraction of the branches (64) are shown for clarity. The batch used in this study had 114 end groups on average, as determined by potentiometric titration. The modification of all end groups from the original primary amines is depicted by colored circles, showing covalent attachment of 3 paclitaxel molecules (PX: red) and 3 Cy5 molecules (Cy: blue), on average. The remaining surface groups were neutralized by the addition of 108 hydroxyl groups, on average (OH: dark green). The chemical structures of the hydroxyl end groups (OH) and paclitaxel (PX)—covalently linked to the dendrimer at the 2'OH (red) by a linker containing an ester, disulfide bridge, and amide bond—are shown on the right.

itations are currently being explored experimentally and in clinical trials.[30–32] One potential strategy is to use a water-soluble drug carrier such as a PAMAM dendrimer. PAMAM dendrimers are branched, organic nanoparticles that are highly multivalent, allowing for the attachment of many (different) ligands (Figure 3.1).[43,47] PAMAM dendrimers have shown promise as a drug delivery platform in the treatment of many diseases, including cancer.[32,48–51] Notably, paclitaxel-conjugated generation 5 (G5)[52] PAMAM dendrimers have demonstrated cytotoxicity against cancerous cells.[53] The mechanism(s) of cytotoxicity of these paclitaxel-conjugated dendrimers, however, was not investigated. That is, it is not known if the observed cytotoxicity is due to paclitaxel stabilization of microtubules, or to some other mechanism(s). The dendrimers were designed so that the paclitaxel load can be cleaved from the dendrimer carrier inside the cell, *via* the hydrolysis of the ester bond at the C2'-OH of paclitaxel (Figure 3.1), and/or a second ester bond that tethers the drug-linker to the dendrimer carrier. This mechanism has not been experimentally confirmed, although numerous studies suggest that such paclitaxel prodrugs similarly employing a C2'-ester bond have no *in vitro* activity, but gain activity *in vivo*, suggesting that this ester bond may be cleaved intracellularly to release paclitaxel.[54–56] The second ester bond within the linker has now been replaced with a disulfide bridge and amide bond (Figure 3.1)[57,58] to provide better chemical stability of the linker during synthesis. In addition, a disulfide bond may provide a second mechanism for the intracellular release of the paclitaxel load, as it can be cleaved in the reductive environment of endosomes or lysosomes.[57,58] However, the questions remain whether paclitaxel is cleaved from the dendrimer carrier in the cell (and if so, how rapidly), and whether the still paclitaxel-coupled or paclitaxel-free dendrimer may contribute to cytotoxicity by binding to microtubules.

To address the question of whether PAMAM dendrimers, with or without paclitaxel, bind to microtubules, a turbidity assay as well as two single microtubule mi-

croscopy techniques, total internal reflection fluorescence microscopy (TIRFM) and transmission electron microscopy (TEM), are used to investigate the effects of paclitaxel-conjugated or unconjugated dendrimers on purified microtubules *in vitro*. These assays were performed *in vitro* in order to directly observe the effects of the dendrimers on microtubules, while removing the possibility of the conjugates causing cytoxicity through non-microtubule interactions. First, it is found that the paclitaxel-conjugated G5 PAMAM dendrimers stabilize polymerizing microtubules against depolymerization, in a paclitaxel-dependent manner, although much less efficiently than free paclitaxel. Second, and more surprisingly, it is found that G5 PAMAM dendrimers are able to bind and bundle pre-formed microtubules, even after removing both paclitaxel and any surface charges (by addition of hydroxyl groups to the terminal primary amine groups). This paclitaxel-independent mode of action is probably induced, at least in part, by electrostatic interactions, involving protonated tertiary amine functionalities of the interior dendrimer core (Figure 3.1). Both modes of action result in microtubules stabilized against depolymerization, which is expected to impair cellular mitosis. Therefore, at least at the concentrations used in this study, our results call to attention the need to carefully consider potentially harmful molecular interactions mediated even by surface-neutralized drug carriers during the design of novel targeted drug delivery strategies.

3.2 Materials and Methods

Materials

MES, $MgCl_2$, and GTP were all purchased from Fisher Scientific (Waltham, MA). EGTA, paclitaxel, PCA, and PCD from Sigma-Aldrich (St. Louis, MO); Trolox from Acros Organics (Geel, Belgium); GpCpp (GMPCPP) from Jena Biosciences (Jena, Germany); TMR from Molecular Probes (Eugene, OR); and Cy succimidyl ester from

GE Healthcare Life Sciences (Piscataway Township, NJ).

Tubulin purification and polymerization

Tubulin was purified from bovine brain and fluorescently labeled with TMR by Neha Kaul, Jenna Campbell, and Charles Chang Jiang in Edgar Meyhöfer's lab. Briefly, tubulin was purified from bovine brain by two cycles of microtubule polymerization in the presence of a high-molarity PIPES buffer.[34] Tubulin was TMR-labeled by reacting polymerized microtubules with a 20-fold excess of TMR at room temperature for 30 min. Competent, TMR-labeled tubulin was purified from this mixture by repeated depolymerization and polymerization.[35]

For all experiments, microtubules were polymerized by incubating 2 mg/mL (≈ 20 μM) α/β-tubulin dimers (using a mix of TMR-labeled and unlabeled tubulin dimers to achieve a final ratio of 1 TMR dye per 20 dimers, as determined by UV-Vis, where noted) with 4 mM $MgCl_2$ and 1 mM GTP, or GMPCPP where noted, in $MEM80_{6.8}$ buffer (80 mM MES-KOH, pH 6.8, 1 mM EGTA, 2 mM $MgCl_2$) at 37 °C for 30 min. After polymerization, the microtubules were stabilized with 10 μM paclitaxel, unless otherwise noted.

Synthesis and characterization of paclitaxel-conjugated G5 PAMAM dendrimers

G5 PAMAM dendrimers ($(NH_2)_{114}$-G5) were purchased from Dendritech, Inc. (Midland, MI). The dendrimers were first purified using a 10 kDa MWCO dialysis membrane, achieving a relatively monodisperse population (PDI = 1.01–1.05, determined by GPC).[38] The average number of primary amine end groups was determined to be 114 by potentiometric titration after purification by dialysis, membrane filtration, and lyophilization.[39] These dendrimers were first reacted with 5 molar equivalents of Cy5 NHS-ester to achieve an average of 2-3 Cy5 molecules per dendrimer, as

determined by ^{1}H NMR and UV-Vis. The Cy5 labeled PAMAM amine-terminated dendrimer was then fully capped with carboxylic acid groups by reacting glutaric anhydride with the primary amine end groups on the dendrimer. Finally, the Cy5-carboxylated dendrimer was reacted with 10 molar equivalents of paclitaxel, previously conjugated to the ester-disulfide-amide linker (see Supplementary Materials), to achieve an average of 3.2 paclitaxel molecules per dendrimer, as determined by ^{1}H NMR. The residual active groups were neutralized by addition of hydroxyl groups. More details concerning the synthesis, purification, and characterization of the paclitaxel-conjugated G5 dendrimer, as well as of the paclitaxel-conjugated generation 3 (G3) dendrimer and the paclitaxel linkers used for each dendrimer, are available in the Supplementary Materials.

Turbidity Assays

Turbidity assays were conducted as described previously.[59] Briefly, 2.0 mg/mL of unlabeled tubulin ($\approx$ 20 μM) was mixed with 4 mM $MgCl_2$ in $MEM80_{6.8}$ and incubated on ice for 30 min. Meanwhile, the following components were pre-warmed at 37 $^\circ$ in cuvettes: (1) no additional components; (2) 1 mM GTP; (3) 1 mM GTP and 10 μM paclitaxel; (4) 1 mM GTP and 3.33 μM $PX_3Cy_{2-3}OH_{108}$-G5; or (5) 1 mM GTP and 3.33 μM $Cy_{2-3}OH_{111}$-G5. After 30 min, the tubulin mixtures were added to the cuvettes and the readings were begun immediately. The turbidity (polymerization) of the reaction mixtures was monitored at 340 nm once every minute for 30 min at 37 $^\circ$C on a Beckman DU-640 UV-Vis Spectrometer utilizing a High Performance Peltier Temperature Controller (Beckman Coulter, Brea, CA).

TIRFM

Imaging chambers were prepared by affixing a cover glass (No. 1.5, 24x30 mm, VWR, Radnor, PA) to a glass slide (Fischer Scientific, Waltham, MA) with double-

sided sticky tape. After the imaging solution was flown into the chamber, the chamber was sealed with candle wax. Images were taken on an inverted fluorescence microscope (model IX81, Olympus, Center Valley, PA) using a 60x objective lens. Samples were illuminated at either 532 nm (for TMR; type Compass 315M, Coherent Inc., Santa Clara, CA) or 635 nm (for Cy5; type Cube 640-100C, Coherent Inc., Santa Clara, CA) at the critical angle, using a cellˆ TIRF^{TM} Illuminator (Olympus, Center Valley, PA). Fluorescent emissions were split into four separate channels using a QV2 Quad View Imaging System (Photometrics, Tuscon, AZ) and projected onto an EMCCD camera (model Evolve 512, Photometrics, Tuscon, AZ). Fluorescent images were viewed using MetaMorph software (Molecular Devices, Sunnyvale, CA).

TIRFM Polymerization Assays

2.0 mg/mL of a mix of unlabeled and TMR-labeled (see above) tubulin ($\approx$ 20 μM) was mixed with 4 mM $MgCl_2$ and 1 mM GTP in $MEM80_{6.8}$ and either (1) no additional components; (2) 10 μM paclitaxel; (3) 3.33 μM $PX_3Cy_{2-3}OH_{108}$-G5; or (4) 3.33 μM $Cy_{2-3}OH_{111}$-G5 at 37 °C for 30 min. The resulting tubulin mixtures were incubated at room temperature for another 180 min to allow unstable microtubules to depolymerize (it was first determined that no microtubules from sample (1) could be detected by TIRFM after 180 min incubation at room temperature). Prior to visualization by TIRFM, the samples were either diluted to 4 (sample 2) or 15 (samples 1, 3, 4) μM tubulin in $MEM80_{6.8}$, supplemented with an oxygen scavenging system (OSS; 5 mM PCA, 50 nM PCD, 2 mM Trolox).

Co-localization of Dendrimers and Pre-formed Microtubules Observed by TIRFM

TMR-labeled, paclitaxel- or GMPCPP-stabilized microtubules were polymerized and stabilized as described above (see section Tubulin purification and polymeriza-

tion) and incubated with either (1) $PX_3Cy_{2-3}OH_{108}$-G5; or (2) $Cy_{2-3}OH_{111}$-G5 and OSS at a 7:1 ratio of dendrimers:tubulin dimers (2.1:0.29 μM) in $MEM80_{6.8}$ for 30, 105, or 180 min at room temperature prior to visualization by TIRFM. To determine the proportion of microtubules bound by dendrimers for each sample, a coverslip area of 0.5-2 mm^2 was scanned, the bound and unbound microtubules were counted, and the number of microtubules counted were normalized to the total coverslip area scanned. Statistical significance of the difference of the proportion of dendrimer-bound microtubules counted between samples was determined using the Fisher's exact test at significance level $\alpha = 0.05$.

TEM

Carbon-coated copper mesh TEM grids were glow-discharged using a Solarus 950 (Gatan, Inc., Pleasanton, CA). Samples were placed on the carbon-coated side of the grid and negatively stained with a 0.75 % solution of uranyl formate.[60] It was assumed that the acidic pH of the stain would not significantly alter the pH of the sample as the stain would fix the sample in $\leq$ 10 ms.[61] Samples were imaged using a Morgagni 268 transmission electron microscope (FEI, Hillsboro, OR).

Microtubule Bundling Observed by TEM

TMR-labeled microtubules were polymerized as described above (see section Tubulin purification and polymerization) and pelleted from unpolymerized tubulin by centrifugation (Airfuge, rotor A-100, Beckman, Fullerton, CA; 30 s at 30 psi). After centrifugation, microtubules were resuspended in $MEM80_{6.8}$ to an estimated 3.2 μM, based on the microtubule recovery efficiencies determined previously (data not shown). Microtubules (at 0.64 μM tubulin) were then incubated with either (1) 10 μM paclitaxel; (2) 3.33 μM $PX_3Cy_{2-3}OH_{108}$-G5 (which equates to 10 μM of conjugated paclitaxel); or (3) 3.33 μM $Cy_{2-3}OH_{111}$-G5 to achieve a 1:1 ratio of dendrimer:tubulin

dimers in MEM80 at variable pH, adjusted with KOH, for 30 min at room temperature prior to visualization by TEM.

Quantitative Analysis of Microtubule Bundling in TEM Images

The diameter of microtubule (bundles) in TEM images taken at 3,095x magnification was measured at 10 pixel intervals and the corresponding microtubule length was weighted according to the number of bundled microtubules determined to be in that length. The diameter of a single, unbundled microtubule, within two standard deviations from the mean, was assigned to the weight of 1, and this was used as a basis to assign diameter ranges to higher weights for bundled microtubules. The fraction of bundled microtubules in a sample was calculated as the fraction of bundled microtubule length per total measured microtubule length. This analytical process was automated using a MATLAB (MathWorks, Natick, MA) script written in-house.

Statistical Tests for Significance in Bundling

Statistical significance of the difference of mean bundled microtubule length between samples was tested using the Student's t-test, assuming equal variances, at significance level $\alpha = 0.05$. Prior to this test, it was verified that the two samples being compared had equal variances using the F-test at significance level $\alpha = 0.05$. All statistical tests were performed using the Statistics Toolbox in MATLAB (MathWorks, Natick, MA).

3.3 Results and Discussion

Probing the Interactions of Modified PAMAM Dendrimers with Microtubules

The design of the paclitaxel-conjugated, generation 5 (G5) or 3 (G3), PAMAM dendrimers used in this study, hereafter referred to by their stoichiometry as PX_3Cy_{2-3}-OH_{108}-G5 (Figure 3.1) and $PX_3Cy_{2-3}OH_{26}$-G3, respectively, was based on the G5 paclitaxel-conjugate used in our previous cytotoxicity study.[53] As the purpose of the previously designed conjugate was for targeted cancer drug delivery, the conjugate bore the therapeutic drug paclitaxel, the tumor targeting molecule folic acid, and the fluorescent molecule FITC. In the current study, folic acid was not included on the conjugates for simplicity since these the conjugated were not tested on cells, and replaced the fluorophore FITC with Cy5 to achieve the most sensitive detection by objective-type TIRFM.[62]

For increased stability during chemical conjugation, a new paclitaxel-dendrimer linker was developed that contained an ester-disulfide-amide linker instead of the double-ester linker used in the previous study (Figure 3.1).[53] An additional benefit to this change is that the disulfide bond may be cleaved in the reductive environment of the endosome or lysosome, if the conjugate enters the cell *via* receptor-mediated endocytosis. This mechanism has shown promise for the delivery of drug therapeutics linked to carriers with disulfide bonds,[63] including the specific case using paclitaxel,[57,58] although the supporting results are still debated.[64]

Generally, the synthesis, purification, and analysis of the conjugates were performed following standard methods described elsewhere (Materials and Methods and Supplementary Materials).[65] Cy5 was first conjugated to the G5, or G3, dendrimer at a mean stoichiometric ratio of 2-3 fluorophores per dendrimer, as determined by ^{1}H NMR and UV-Vis spectroscopy. Next, the paclitaxel-linker was conjugated to the

G5 and G3 dendrimer core at a mean stoichiometric ratio of 3.2 and 2.8, respectively, drug molecules per dendrimer, as determined by ^{1}H NMR spectroscopy. Prior to conjugation to the dendrimer, the integrity of the paclitaxel-linker was confirmed by high resolution mass spectroscopy and ^{1}H NMR spectroscopy. Finally, the remaining surface groups on the dendrimer, initially primary amines, were neutralized by the addition of hydroxyl groups, as previous studies have found that highly cationic PAMAM dendrimers disrupt cellular membranes.[66,67] UPLC was used to confirm that no detectable level of free paclitaxel was present in the conjugate preparations (see Supplementary Materials) and that the paclitaxel conjugate was stable in water for up to 20 h, which is much greater than the time period of an experiment ($\leq$ 6 h). As negative controls, G5 dendrimers without paclitaxel were synthesized in parallel with $PX_3Cy_{2-3}OH_{108}$-G5, with the exemption of the paclitaxel conjugation steps. Therefore, the only chemical difference between these dendrimers and $PX_3Cy_{2-3}OH_{108}$-G5 is the presence of paclitaxel. Hereafter this dendrimer will be referred to as $Cy_{2-3}OH_{111}$-G5.

Microtubule polymerization and all experiments were carried out in a standard, near-physiological buffer termed "$MEM80_{6.8}$", composed of 80 mM MES-KOH, pH 6.8, 1 mM ethylene glycol tetraacetic acid (EGTA), and 2 mM $MgCl_2$ (Materials and Methods). This buffer will be referred to as only "MEM80" when the pH is varied from 6.8. $MEM80_{6.8}$ is identical in composition to BRB80, a buffer commonly used for polymerizing microtubules *in vitro*,[68] except the buffering agent PIPES is replaced by MES.[25] For observing dendrimer binding by TIRFM co-localization, sparsely 5-(6)-carboxytetramethylrhodamine succimidyl ester (TMR)-labeled tubulin purified from bovine brain, as described before,[10] were used and a dendrimer:tubulin dimer ratio of 7:1. No binding events were observed by TIRFM when the dendrimer concentration was significantly less than a 7-fold excess of the tubulin concentration. Since there are on average three paclitaxel molecules conjugated to each dendrimer, this ratio

would equate to achieving a cellular paclitaxel concentration of 300-400 μM, assuming an average cellular tubulin concentration of 15-20 μM.[69,70] To decrease background signal from unbound dendrimers, TEM assays were performed at a slightly lesser dendrimer:tubulin dimer ratio of 1:1, which corresponds to a cellular paclitaxel concentration of 15-20 μM. Note that although the paclitaxel concentrations used in our experiments seem very high in this context, these concentrations are standard for *in vitro* stabilization of microtubules,[71] which are the focus of this study.

G5 PAMAM Dendrimers Induce Turbidities in Tubulin Solutions Comparable to Paclitaxel

Turbidity assays are standard ensemble microtubule polymerization assays as the turbidity of a tubulin solution is a reliable measure of the mass of microtubules present.[72] To determine the ability of $PX_3Cy_{2-3}OH_{108}$-G5 to induce microtubule polymerization and stabilization compared to paclitaxel, tubulin was mixed together with these components and monitored the turbidity of the mixtures at 37 °C for 30 min, as described in the Materials and Methods section and elsewhere.[59] The following controls were also tested for comparison: (1) tubulin in the absence of GTP, paclitaxel, or dendrimers; and (2) tubulin, GTP, and $Cy_{2-3}OH_{111}$-G5.

The results of these turbidity assays are summarized in Figure 3.2. During the time course of the experiment, the turbidity of all tubulin mixtures increased in an exponential fashion (R^2 = 0.96-0.99), except for the tubulin mixture not containing GTP, paclitaxel, or dendrimers, which increased in a linear fashion (R^2 = 0.9995) (Figure 3.2a). Notably, the turbidity limits reached by the tubulin mixtures in the presence of paclitaxel, $PX_3Cy_{2-3}OH_{108}$-G5, or $Cy_{2-3}OH_{111}$-G5 were not significantly different ($p > 0.05$, Student's t-test), on average (Figure 3.2b). However, the rate of turbidity change was about 3-fold greater in the presence of paclitaxel, compared to that measured in the presence of $PX_3Cy_{2-3}OH_{108}$-G5, or $Cy_{2-3}OH_{111}$-G5 (which were

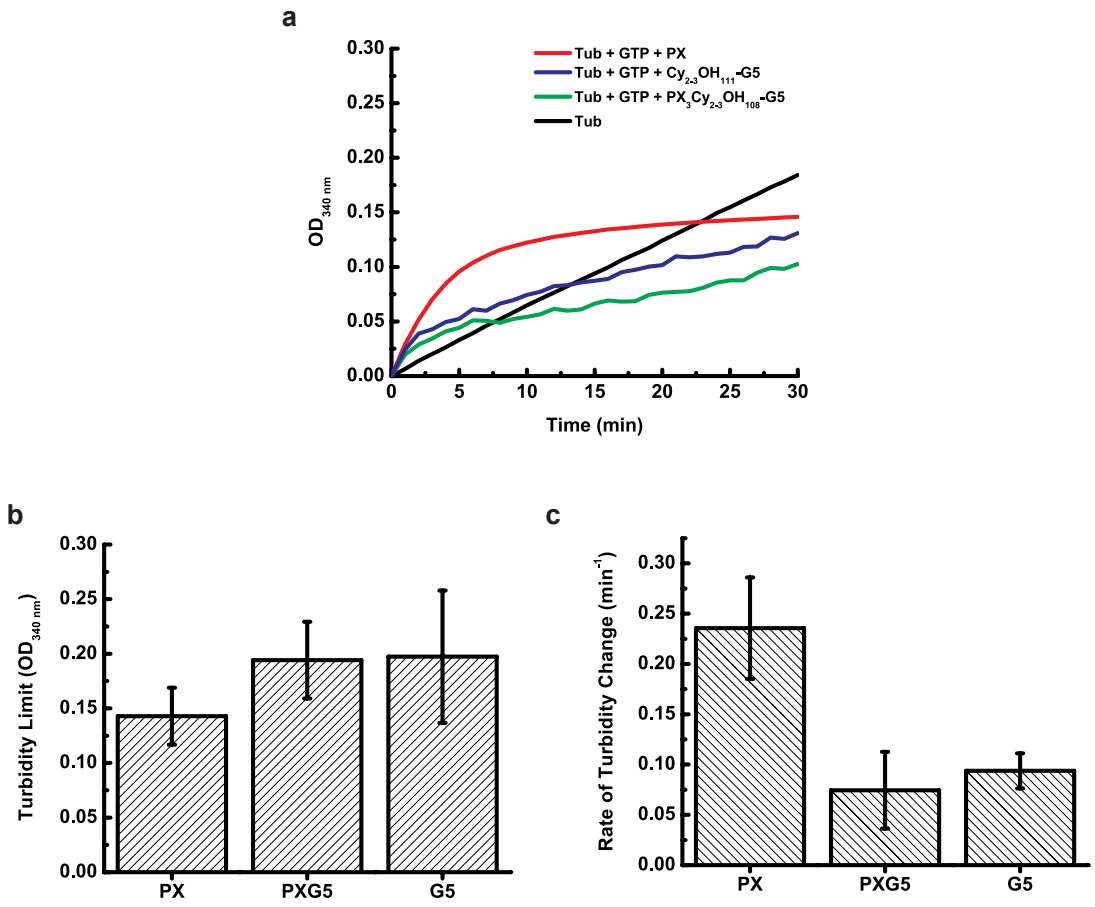

Figure 3.2: Turbidity polymerization assays. (a) The average turbidities of 2 mg/mL tubulin (Tub) solutions in the presence of (1) no extra components (black; n = 2); (2) GTP and paclitaxel (PX) (red; n = 3); (3) GTP and $PX_3Cy_{2-3}OH_{108}$-G5 (green; n = 3); or (4) GTP and $Cy_{2-3}OH_{111}$-G5 (blue; n = 4) was monitored at 340 nm once every minute for 30 min at 37 °C. Error bars are not shown for clarity. All turbidity trends, with the exception of tubulin alone (which was fit with a linear equation), were fit with the exponential growth equation $y = A(1\text{-}e^{-kt})$ at R^2 = 0.96-0.99. (b) The average turbidity limits (parameter A from fit) from the tubulin mixtures in the presence of GTP and (1) paclitaxel (PX); (2) $PX_3Cy_{2-3}OH_{108}$-G5 (PXG5); or (3) $Cy_{2-3}OH_{111}$-G5 (G5). (c) The average rate of turbidity changes (parameter k from fit) from the tubulin mixtures.

not significantly different from each other; $p > 0.05$, Student's t-test) (Figure 3.2c). The exponential increase in turbidity of the tubulin mixtures in the presence of dendrimers while at 37 °C suggests the formation of microtubules or alternatively, non-microtubule tubulin aggregates. To distinguish between these alternatives, TIRFM was used, which allows visualization of single microtubules.

$PX_3Cy_{2-3}OH_{108}$-G5 Stabilize Polymerizing Microtubules

To determine if the dendrimers are able to induce to the formation of microtubule-like structures, the same general procedure was followed as with the turbidity assays, except mixing in a small fraction of TMR-labeled tubulin (5% of all tubulin dimers carry one TMR dye, see Materials and Methods) to allow visualization by TIRFM. To further test the ability of $PX_3Cy_{2-3}OH_{108}$-G5 to not only promote polymerization of microtubules, but to stabilize them, the tubulin mixtures were incubated at room temperature following the 30 min incubation at 37 °C. Prior to the experiment, it was determined determined how long a tubulin mixture in the presence of only GTP has to be incubated at room temperature (180 min) before the concentration of unpolymerized tubulin in solution becomes so great that the fluorescence from this tubulin obscures the fluorescence of any remaining microtubules on the slide surface.

The results of these TIRFM experiments are summarized in Figure 3.3. No microtubules were observed in the absence of paclitaxel after 180 min (Figure 3.3a); but instead a fluorescent haze (not shown) due to the high concentration of unpolymerized tubulin in solution. Contrast adjustment of these images revealed unpolymerized tubulin on the surface (Figure 3.3a). By contrast, typical microtubules, identified as green rods based on their TMR fluorescence, were polymerized and stabilized by free paclitaxel, in the absence of dendrimers (Figure 3.3b). In the presence of $PX_3Cy_{2-3}OH_{108}$-G5, microtubule-like green rods (Figure 3.3c), similar to those observed in Figure 3.3a, were co-localized with $PX_3Cy_{2-3}OH_{108}$-G5, which are

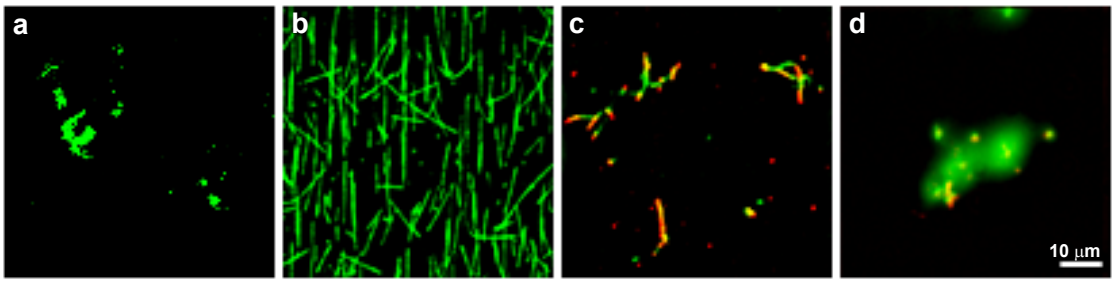

Figure 3.3: Polymerization assays imaged by TIRFM. Images from the TMR channel (green: microtubules) are overlaid onto images from the Cy5 channel (red: dendrimers). Scale bar shown is 10 μm. In these assays, 2 mg/mL α/β-tubulin heterodimers are incubated with either (a) no stabilizers; (b) free paclitaxel; (c) $PX_3Cy_{2-3}OH_{108}$-G5; or (d) $Cy_{2-3}OH_{111}$-G5 in $MEM80_{6.8}$ supplemented with 1 mM GTP at 37 °C for 30 min, then at room temperature for 180 min. To obtain the best image in the presence of a high density of microtubules, the microtubule-paclitaxel sample (b) was diluted 4-fold (as compared to the imaging concentration in the other three samples, which were equal) immediately prior to imaging.

found through their red Cy5 fluorescence. With a few exceptions, $PX_3Cy_{2-3}OH_{108}$-G5 dendrimers were often observed to co-localize at the ends of the microtubule-like rods. The apparent microtubules observed in Figure 3.3c were likely stabilized by $PX_3Cy_{2-3}OH_{108}$-G5, since microtubules polymerized at the tubulin concentrations used in this experiment completely depolymerize after 180 min (the incubation time used in this experiment) in the absence of dendrimers and paclitaxel (Figure 3.3a). However, stabilization by $PX_3Cy_{2-3}OH_{108}$-G5 was very inefficient compared to free paclitaxel, as evidenced by the difference in microtubule density between Figures 3.3b and c, made even greater by the fact that the tubulin imaging concentration in Figure 3.3c was about 4-fold greater than the concentration in Figure 3.3b. This reduction in tubulin imaging concentration for Figure 3.3b was implemented in order to get a clear image, as the microtubules were initially too dense on the slide at the imaging concentration of Figure 3.3a; c-d. In the presence of paclitaxel-unconjugated $Cy_{2-3}OH_{111}$-G5, only non-cylindrical tubulin aggregates were observed, which were seemingly bound by dendrimers, as evidenced by the co-localization of green TMR and red Cy5 fluorescence in some areas (Figure 3.3d).

Together, these results suggest that $PX_3Cy_{2-3}OH_{108}$-G5 is able to bind microtubules specifically through the conjugated drug, resulting in the stabilization of microtubules polymerized in the presence of the paclitaxel-dendrimer conjugate. This stabilization is, however, very inefficient compared to free paclitaxel. This apparent decrease in binding affinity of the dendrimer-conjugated paclitaxel compared to free paclitaxel may result from its conjugation to the dendrimer, as previous studies have shown that paclitaxel prodrugs modified at the same paclitaxel functional group, the 2' OH (see Figure 3.1), have reduced affinity for microtubules.[54–56] Additionally, or alternatively, the size of the dendrimer ($\approx$ 5.4 nm) may hinder the binding of a sufficient number of paclitaxel-conjugated dendrimers to accomplish microtubule stabilization. Notably, while some microtubules were bound along their entire length by

$PX_3Cy_{2-3}OH_{108}$-G5, many were only bound at the ends (Figure 3.3c). It is possible in these cases that tubulin dimers bound by $PX_3Cy_{2-3}OH_{108}$-G5 are added to the (+) end of an existing microtubule, stabilizing the (+) end and slowing depolymerization. It is also important to note that $Cy_{2-3}OH_{111}$-G5—and presumably $PX_3Cy_{2-3}OH_{108}$-G5 as well—binds tubulin through an interaction independent of paclitaxel, and that this interaction does not promote stabilization of microtubules.

Interpreting these results together with the turbidity results (Figure 3.2), PX_3-$Cy_{2-3}OH_{108}$-G5 is able to induce a very low level of polymerization *via* the conjugated paclitaxel. In addition, as the TIRFM image in Figure 3.3d suggests, even in the absence of conjugated paclitaxel, $Cy_{2-3}OH_{111}$-G5 is able to induce tubulin aggregation, which may also lead to an increase in turbidity. Presumably, since $PX_3Cy_{2-3}OH_{108}$-G5 is identical in structure to $Cy_{2-3}OH_{111}$-G5 with the exception of three molecules of paclitaxel, $PX_3Cy_{2-3}OH_{108}$-G5 can also induce tubulin aggregation. These interpretations may explain the observation that the dendrimers increase the turbidity of a tubulin solution to a level comparable with paclitaxel (Figure 3.2).

$PX_3Cy_{2-3}OH_{108}$-G5 Binds Paclitaxel- but Not GMPCPP-stabilized Microtubules

It was next sought to determine if $PX_3Cy_{2-3}OH_{108}$-G5 could bind and stabilize pre-assembled microtubules, which it would also encounter in the cell. To test this idea, co-localization of $PX_3Cy_{2-3}OH_{108}$-G5 with pre-assembled microtubules was probed for by TIRFM. Tubulin dimers were pre-assembled into microtubules and these microtubules were stabilized with an equimolar concentration of free paclitaxel (Materials and Methods), the concentration of which was subsequently reduced by 4-fold dilution upon incubation for 30, 105, or 180 min at room temperature with $PX_3Cy_{2-3}OH_{108}$-G5 or $Cy_{2-3}OH_{111}$-G5 in $MEM80_{6.8}$, which did not contain any additional free paclitaxel, at a 7:1 ratio of dendrimers:tubulin dimers. The number

of microtubules bound or unbound by dendrimers was counted for each sample and normalized by the total coverslip surface area scanned.

When incubated with $PX_3Cy_{2-3}OH_{108}$-G5, two distinct populations of microtubules were observed (Figure 3.4a): (1) those that only fluoresced in the TMR emission channel (green in images, corresponding to tubulin); and (2) those that fluoresced in the Cy5 channel (corresponding to $PX_3Cy_{2-3}OH_{108}$-G5 fluorescence) only (red in images) or in addition to the TMR channel (yellow in images). Population 1 appears entirely free of $PX_3Cy_{2-3}OH_{108}$-G5 whereas population 2 is bound throughout by $PX_3Cy_{2-3}OH_{108}$-G5, sometimes so extensively that the TMR signal is not observed, likely due to fluorescence resonance energy transfer (FRET) from TMR on the tubulin to Cy5 on the dendrimer (top left image in Figure 3.4a). Note that no microtubules that are only bound by dendrimers at the microtubules ends are observed in the present experiment as they were in Figure 3.3c, and that few uniformly bound microtubules are observed in Figure 3.3c compared to the present experiment. This apparent discrepancy may be due to limited sampling.

Different structural populations of $PX_3Cy_{2-3}OH_{108}$-G5-bound microtubules were also observed. Some appeared similar to unbound microtubules (top two images in Figure 3.4a), but some had a distinctly larger diameter (bottom left image in Figure 3.4a) whereas others seemed to be bundled microtubules, as represented by the microtubule(s) in the bottom right image of Figure 3.4a, which appears to have a split tail.

Overall, the fraction of the total microtubule population that was bound by $PX_3Cy_{2-3}OH_{108}$-G5 was initially very small—only 3.4% at the 30 min time point. The bound fraction increased over time, but this partially coincided with a drastic decrease in the total microtubule population (Figure 3.4e). This population decrease was likely due to inadequate stabilization by $PX_3Cy_{2-3}OH_{108}$-G5. The very few microtubules that remained at the end of the experiment were bound, and therefore

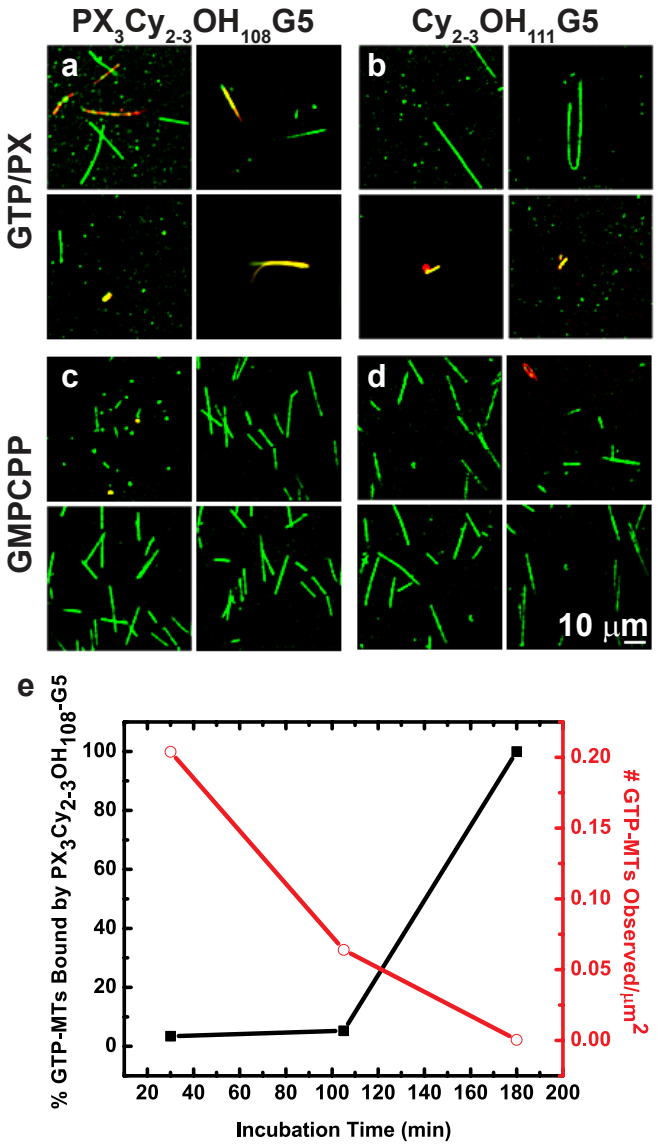

Figure 3.4: Co-localization assays between dendrimers and pre-formed microtubules visualized by TIRFM. Images from the TMR channel (green: microtubules) and Cy5 channel (red: dendrimers) are overlaid. Scale bar shown is 10 μm. Microtubules were polymerized, stabilized with either free paclitaxel (a-b) or GMPCPP (c-d), then incubated with either $PX_3Cy_{2-3}OH_{108}$-G5 (a,c) or $Cy_{2-3}OH_{111}$-G5 (b,d) for 30, 105, or 180 min at room temperature. All images shown are from the 30 min time point, and each 2 x 2 grid of images are from the same sample. The number of microtubules bound or unbound by dendrimers was counted for each sample and normalized by the total coverslip surface area scanned. The plot in (e) shows these normalized data for the GTP-stabilized microtubules and the $PX_3Cy_{2-3}OH_{108}$-G5 samples over time.

presumably stabilized, by $PX_3Cy_{2-3}OH_{108}$-G5. Recall that $PX_3Cy_{2-3}OH_{108}$-G5 was observed to stabilize microtubules in Figure 3.3c, and that this stabilization seemed much less efficient than that induced by free paclitaxel. However, the extent of stabilization in this latter experiment can not be quantitatively compared with the current experiment as the former provided only qualitative observations. The negative control dendrimer, $Cy_{2-3}OH_{111}$-G5, showed an even smaller incidence of binding: only 2.2% of paclitaxel-microtubules after 105 min. No binding was observed at the 30 and 180 min time points. As found with $PX_3Cy_{2-3}OH_{108}$-G5, all bound microtubules observed were bound by $Cy_{2-3}OH_{111}$-G5 along their entire length (Figure 3.4b).

Because so few microtubules bound by $PX_3Cy_{2-3}OH_{108}$-G5 were observed, it was next asked whether $PX_3Cy_{2-3}OH_{108}$-G5 may still be competing for paclitaxel binding sites with the free paclitaxel used to initially stabilize the microtubules immediately after polymerization, even though its concentration was reduced 20-fold by buffer exchange upon incubation with $PX_3Cy_{2-3}OH_{108}$-G5. To this end, stable microtubules were polymerized in the presence of GMPCPP (a slowly hydrolyzable analogue of GTP)[73] instead of GTP and paclitaxel. Hereafter, these populations will be referred to as GMPCPP-microtubules and GTP-microtubules, respectively. The results of this experiment are shown in Figure 3.4c-d. The fraction of $PX_3Cy_{2-3}OH_{108}$-G5-bound GTP-microtubules observed was significantly greater ($p < 0.05$) than $PX_3Cy_{2-3}OH_{108}$-G5-bound GMPCPP-microtubules at all time points. With $Cy_{2-3}OH_{111}$-G5, this difference was significantly greater only at the 105 min time point.

These observations suggest that $PX_3Cy_{2-3}OH_{108}$-G5 can either associate more readily with GTP-microtubules or dissociate more readily from GMPCPP-microtubules, and that this observation is specifically caused by the paclitaxel on the dendrimer. As these observations directly oppose those obtained with free paclitaxel,[74] the paclitaxel-dependent binding mechanism of $PX_3Cy_{2-3}OH_{108}$-G5 does not likely include access an interior paclitaxel binding site through the microtubule walls.[74]

Since the dendrimers often bind the entire microtubule length, and it is not likely that $PX_3Cy_{2-3}OH_{108}$G5 is able to diffuse along the microtubule length while inside the microtubule within the time frame of the experiments,[75] $PX_3Cy_{2-3}OH_{108}$-G5 is also not likely binding an interior paclitaxel binding site by entering through its ends. Therefore, it is possible that $PX_3Cy_{2-3}OH_{108}$-G5 is either: (1) not binding pre-assembled microtubules, but assembling microtubules that have luminal paclitaxel binding sites exposed to solution, and remaining associated with these microtubules as they complete assembly; or (2) binding an exterior paclitaxel binding site.

The first mechanism is supported by the fact that GTP-microtubules depolymerize faster than GMPCPP-microtubules,[73] which is consistent with the observation of more dendrimer bound GTP-microtubules than GMPCPP-microtubules. Furthermore, this may be the binding mechanism utilized by $PX_3Cy_{2-3}OH_{108}$-G5 in the experiments shown in Figure 3.3 since in these experiments, $PX_3Cy_{2-3}OH_{108}$-G5 was included from the start of the polymerization reaction. The second mechanism is supported by published biochemical and computational data that provides evidence for an exterior paclitaxel binding site.[76–78] If the latter mechanism were occurring in our experiments, it would not disprove the idea that an interior paclitaxel binding site exits,[79] but merely support the hypothesis that there is an additional exterior paclitaxel binding site. It is therefore concluded that the low binding incidence of $PX_3Cy_{2-3}OH_{108}$-G5 is unlikely due to competition with the free paclitaxel used to stabilize the microtubules in the previous experiment.

In addition to G5 paclitaxel-conjugated dendrimers, the ability of a G3 paclitaxel-conjugated dendrimer to bind microtubules was also tested. G3 PAMAM dendrimers are smaller than G5 PAMAM dendrimers, $\approx$ 3.6 nm vs. 5.4 nm.[43,44] Our G3 conjugate (see Supplementary Materials for structural details), named $PX_3Cy_{2-3}OH_{26}$-G3 according to its stoichiometry, has the same number of conjugated paclitaxel and Cy5 molecules per dendrimer as our G5 conjugates, and the same neutral hydroxyl

structure on the remaining end groups. When $PX_3Cy_{2-3}OH_{26}$-G3 was incubated with either paclitaxel- or GMPCPP-stabilized microtubules for 30, 105, or 180 min, under the same conditions used for the G5 conjugates (see above), no binding events were observed (data not shown). The fact that our G3 paclitaxel-conjugates cannot bind microtubules, but our G5 paclitaxel-conjugates can, may be due to the lower density of protonatable amines in the G3 vs. G5 dendrimer core (10 vs. 40 at pH 6.8; see results in subsequent sections).[80]

Taking these observations together, it is proposed that $PX_3Cy_{2-3}OH_{108}$-G5 is able to bind microtubules by two mechanisms: (1) binding and stabilizing polymerizing microtubules in a paclitaxel-dependent manner; and (2) binding pre-formed microtubules in a paclitaxel-independent manner, potentially mediating bundling of these microtubules. The first mechanism is supported by the polymerization experiments described above (see Figure 3.3). The second mechanism is supported by the fact that high concentrations of paclitaxel ($\geq$33 nM),[81] and certain microtubule binding proteins,[82] are known to induce bundling of microtubules, as well as by the two lower images of Figure 3.4a.

It is important to note that while the experiments described thus far suggest these two mechanisms, the ability of $PX_3Cy_{2-3}OH_{108}$-G5 to bind and stabilize microtubules appears by TIRFM to be very low and inefficient, as compared to free paclitaxel. This may be due to a decreased ability, compared to free paclitaxel, of the conjugated paclitaxel to access its binding site in the microtubule lumen. It has been proposed that *in vivo* small molecules such as paclitaxel are able to access the microtubule lumen through $\approx$ 1 nm pores in the microtubule wall,[74,83] whereas large molecules, such as the enzyme tubulin acetyltransferase, are able to access the microtubule lumen either through large transient openings in the microtubule wall or by copolymerization.[84,85] The size of $PX_3Cy_{2-3}OH_{108}$-G5 is on the order of tubulin acetyltransferase, and indeed it have been observed that $PX_3Cy_{2-3}OH_{108}$-G5 is able

to bind and stabilize polymerizing microtubules to some degree, however, it is possible that the entry mechanism utilized by large molecules such as tubulin acetyltransferase *in vivo* is not readily available to $PX_3Cy_{2-3}OH_{108}$-G5 *in vitro*. It is also possible that $PX_3Cy_{2-3}OH_{108}$-G5 may be able to access the microtubule lumen *via* the $\approx$ 17 nm diameter openings at the microtubule ends (Figure 3.3c). However, modeling studies have predicted that paclitaxel would take days to reach half equilibrium concentration in the center of a 40 μm microtubule (typical microtubule lengths are 1-100 μm), and an antibody would take years.[75] The paclitaxel-conjugated dendrimer, which has a molecular weight far greater than that of paclitaxel alone, but lower than that of an antibody, would also likely take days to years. Therefore, it is unlikely that $PX_3Cy_{2-3}OH_{108}$-G5 is accessing its luminal binding site *via* this mechanism on the microtubules that are observed to be bound by $PX_3Cy_{2-3}OH_{108}$-G5 along their entire length (Figure 3.4), and may be binding the outside wall of the microtubule in these instances.

Surface Neutralized G5 PAMAM Dendrimers Bundle Microtubules in a Paclitaxel-Independent Manner

The bundling mechanism discussed above is indirectly supported by the observation that some dendrimer-bound microtubules seem to have a greater diameter than unbound microtubules. Figures 3.4a-b (microtubules in the presence of $PX_3Cy_{2-3}OH_{108}$-G5 or $Cy_{2-3}OH_{111}$-G5, respectively) show this qualitatively. In addition, the results of Figure 3.2 in conjunction with those of Figure 3.3 suggest that the dendrimers induce the formation of large tubulin aggregates. In order to directly observe the structure of these $PX_3Cy_{2-3}OH_{108}$-G5-bound microtubules and determine whether they are bundled, an imaging technique with greater spatial resolution than TIRFM, electron microscopy, was used next.

Electron microscopy is routinely used to measure the diameter of microtubules.[76,86–88]

Employing the same reagents that were used for the TIRFM experiments, and the same protocol—with the additional step of separating polymerized microtubules from unpolymerized tubulin *via* centrifugation to decrease tubulin background (Materials and Methods)—it was sought to examine dendrimer-bound microtubules *via* negative-stain TEM. Negative staining enables single microtubules to be observed, which is advantageous since dendrimers may have multiple effects on microtubules. Using TEM, microtubule diameter cannot be precisely measured due to the requirement that the sample be dried, thereby collapsing the microtubules. Nonetheless, bundled microtubules will be easily distinguished from unbundled microtubules.

To determine if $PX_3Cy_{2-3}OH_{108}$-G5 induces microtubule bundling, the same assays were performed as for the TIRFM imaging above (Figure 3.4). That is, pre-assembled microtubules were incubated with either paclitaxel, $PX_3Cy_{2-3}OH_{108}$-G5, or $Cy_{2-3}OH_{111}$-G5 for 30 min at room temperature, and then imaged the samples *via* TEM. To obtain a rough estimate of the degree of bundling in each sample (Figure 3.5g), the diameter of a microtubule (bundle) was measured at 10 pixel intervals and weighted according to the estimated number of bundled microtubules present in that interval, where the mean diameter of a single, unbundled microtubule within two standard deviations was assigned a weight equal to one. This measurement results in a set of bundled or unbundled microtubule lengths, which are then summed and used to calculate the fraction of bundled microtubule lengths for each sample. This analytic method only provides a rough estimate of the degree of bundling, as the thickness of the microtubule bundle cannot be measured in the z-direction from the TEM images. However, using the planar thickness of the bundles to estimate the number of microtubules present should be sufficient to compare the degree of bundling among the samples tested.

Figures 3.5a and 3.5d show the typical structure of paclitaxel-stabilized microtubules in the absence of dendrimers at both low and high magnification. By compar-

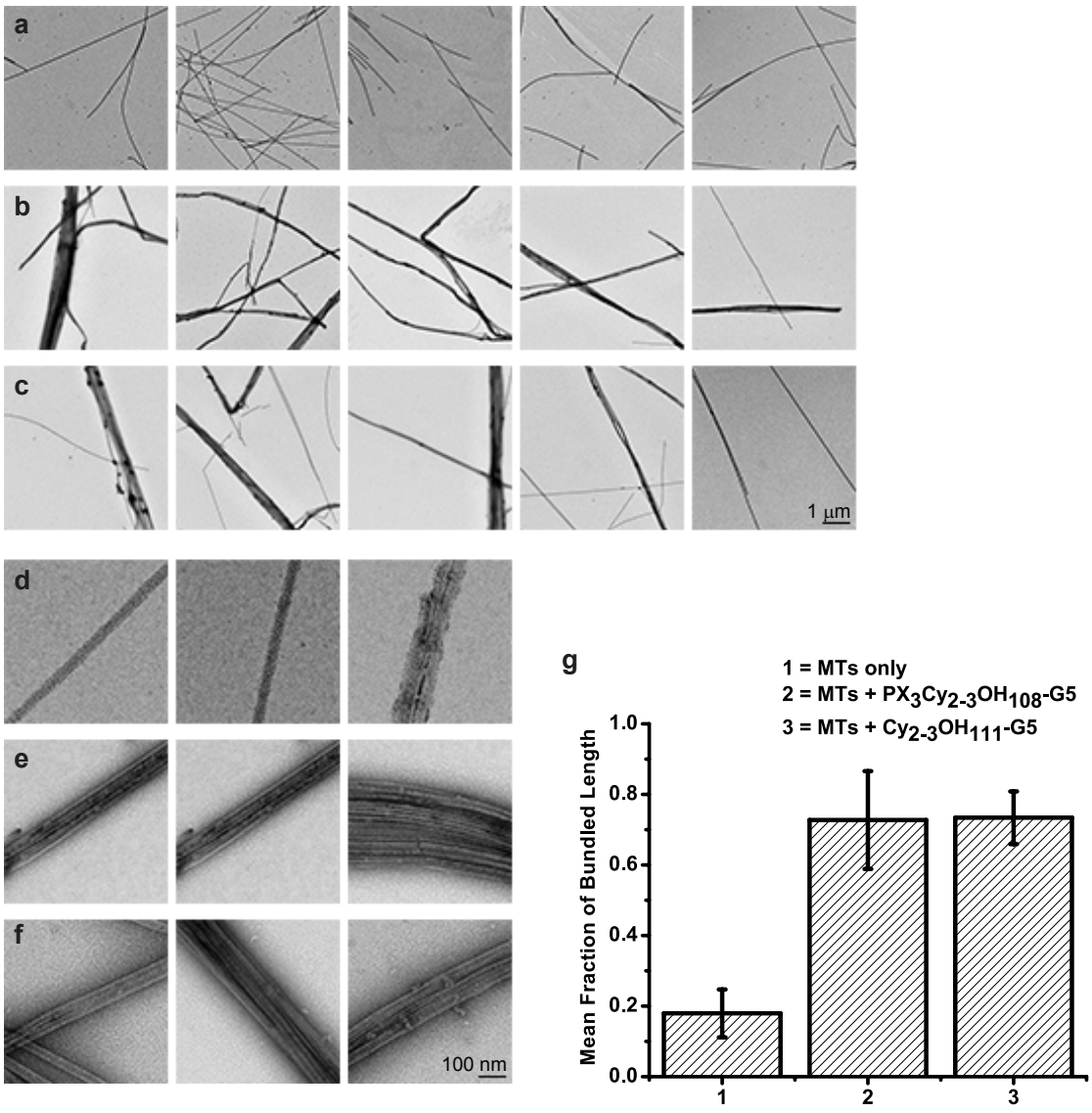

Figure 3.5: Negative-stain TEM images obtained at 3,095x (a-c; scale bar = 1 μm) or 24,628x magnification (d-f; scale bar = 100 nm). Microtubules are incubated in $MEM80_{6.8}$ at room temperature for 30 min with either: paclitaxel (a,d); $PX_3Cy_{2-3}OH_{108}$-G5 (b,e); or $Cy_{2-3}OH_{111}$-G5 (c,f). The amount of bundling in a population is represented as the fraction of bundled microtubule length (g).

ison, Figures 3.5b and 3.5e show microtubules in the presence of $PX_3Cy_{2-3}OH_{108}$-G5, revealing that $PX_3Cy_{2-3}OH_{108}$-G5 induces formation of microtubule bundles of various sizes. The PAMAM dendrimers are not easily resolved in these images due to their small size, low electron mass compared to the carbon imaging grid, and high background from dendrimers and unpolymerized tubulin. Small bundles, containing 2-3 microtubules, were observed in the absence of dendrimers, but the fraction of the total population represented by these bundles was significantly smaller ($p < 0.05$) than the fraction observed in the presence of $PX_3Cy_{2-3}OH_{108}$-G5, as quantified in Figure 3.5g. Intriguingly, a large amount of microtubule bundles was also observed in the presence of $Cy_{2-3}OH_{111}$-G5 (Figure 3.5c,f), and this bundled fraction was not significantly different from the bundling fraction measured in the presence of $PX_3Cy_{2-3}OH_{108}$-G5 ($p > 0.05$) (Figure 3.5g).

Surface Neutralized G5 PAMAM Dendrimers Bundle Microtubules *via* Electrostatic Interactions

It was next sought to identify the properties of $PX_3Cy_{2-3}OH_{108}$-G5 and $Cy_{2-3}OH_{108}$-G5 that induce microtubule bundling. Microtubule bundles have been observed both *in vitro* and *in vivo*, induced by paclitaxel,[81] microtubule-associated proteins (MAPs),[82] or polyamines.[89] The mechanism of action for these microtubule bundling agents has been postulated to be cross-linking and/or charge shielding (*i.e.*, binding the C-terminal tails of the microtubules where the majority of the negative charge is located, thereby reducing electrostatic repulsion between microtubules and allowing them to associate laterally). The fact that there is no significant difference in the amount of bundling induced by $PX_3Cy_{2-3}OH_{108}$-G5 as compared to $Cy_{2-3}OH_{111}$-G5 (see Figure 3.5) precludes the contribution of paclitaxel. The commonalities in the chemical structures of $PX_3Cy_{2-3}OH_{108}$-G5 and $Cy_{2-3}OH_{111}$-G5 (Figure 3.1)—the fluorescent dye Cy5 and the dendrimer core itself—were therefore considered to

determine if either of these components contribute to the observed bundling.

First, considering the dendrimer core structure, it was realized that it contains interior tertiary amines with pKa equal to 6.5 ± 0.2 (derived from potentiometric titration; see Supplementary Materials), and therefore a fraction of these will be positively charged at neutral pH. It is feasible that the interior amines of the dendrimer core could encounter the microtubule surface, as the branched structure of the core is highly flexible and has been predicted by molecular dynamics simulations, and demonstrated by atomic force microscopy, to flatten into a disc-like structure upon encountering a surface.[90] Therefore, it is hypothesized that these protonated tertiary amines contact the microtubule surface and induce microtubule bundling through cross-linking and/or charge shielding. In support of this hypothesis, it is found that unmodified G5 PAMAM dendrimers, hereafter referred to as $(NH_2)_{114}$-G5, carrying 114 protonatable primary amines on the surface, but no paclitaxel or Cy5, are also able to bundle microtubules to a significant degree compared to microtubules alone ($p < 0.05$) (Figure 3.6), although its bundling ability is seemingly lesser than that of $PX_3Cy_{2-3}OH_{108}$-G5 (or by extension, $Cy_{2-3}OH_{111}$-G5). This difference is possibly attributed to the fact that $(NH_2)_{114}$-G5 dendrimers would be highly electrostatically repulsed from each other as they are highly cationic, and therefore fewer $(NH_2)_{114}$-G5 might bind a microtubule than the surface neutralized $PX_3Cy_{2-3}OH_{108}$-G5 or $Cy_{2-3}OH_{111}$-G5. Because the cationic $(NH_2)_{114}$-G5 was able to bundle microtubules, it was therefore sought to test the impact of the positive charges from the interior tertiary amines of $PX_3Cy_{2-3}OH_{108}$-G5 on the ability of these dendrimers to bundle microtubules.

To test the hypothesis that the cationic amines of the dendrimer core interior contribute to the microtubule bundling observed by TIRFM and TEM, the pH of the MEM80 incubation buffer was incrementally increased from 6.5 to 8.3 using KOH, and visualized the resulting dendrimer-microtubule complexes by TEM. As the pH

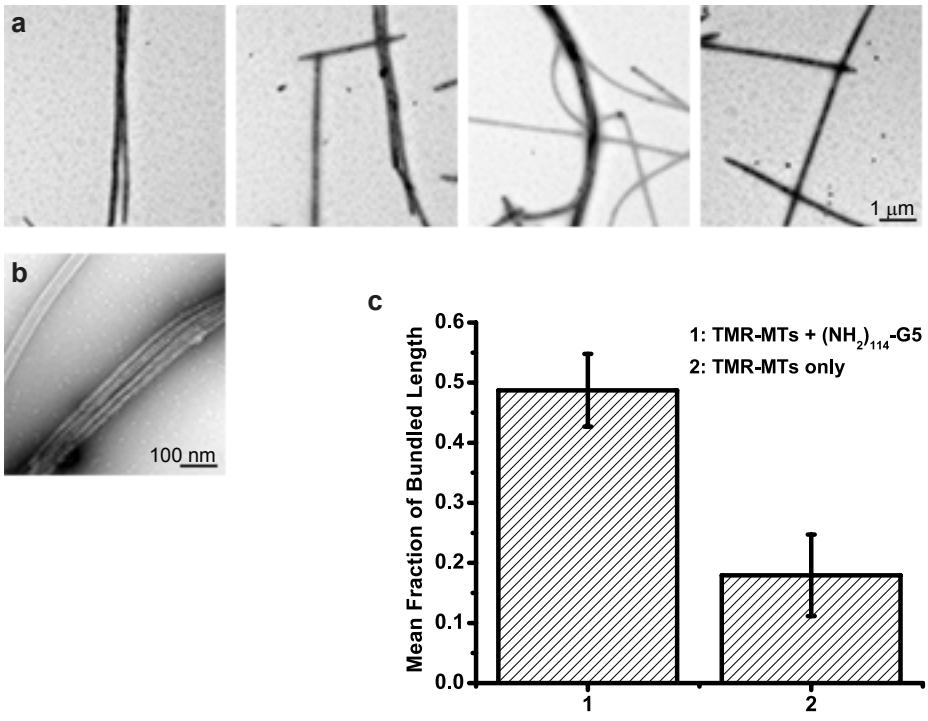

Figure 3.6: Microtubules are incubated with $(NH_2)_{114}$-G5 for 30 min in $MEM80_{6.8}$ and visualized by negative-stain TEM at 3,095x (a; scale bar = 1 μm) or 24,628x (b; scale bar = 100 nm). The amount of bundling in each sample was quantified as before (c), from ten 25.38 μm^2 images from each of three trials. The data from microtubules in the absence of dendrimers (sample 2 in c) was introduced previously (Figure 3.5), but is shown here for reference.

increases, the fraction of tertiary amines in the dendrimer core that are protonated, and therefore positively charged, decreases (Figure 3.7g). If the observed dendrimer-induced bundling is mediated by electrostatics, microtubule bundling will decrease with increasing pH. Only $PX_3Cy_{2-3}OH_{108}$-G5 dendrimers were used for these experiments.

The images of Figure 3.7a-f show qualitatively that the amount of bundling does indeed decrease as the pH increases. The degree of bundling in each sample is roughly estimated as before (Figure 3.7g), and a pH titration curve is fit to the data with an excellent correlation coefficient, $R^2 = 0.94$, suggesting that the observed bundling is indeed pH dependent. From the titration curve, a pKa of bundling equal to 7.6 ± 0.1 is extracted.

The source of the bundling pH dependence could be one or both of the following: (1) electrostatic interactions between the cationic amines in the dendrimer core and the anionic C-terminal tubulin tails on the microtubule surface; or (2) the instability of microtubules at alkaline pH.[91] Considering the first mechanism, the pH increase would cause both a decrease in the number of protonated, cationic amines in the dendrimer core, as well as an increase in the number of deprotonated, anionic C-terminal tubulin tails on the microtubule surface. These changes would decrease any electrostatic attraction between the dendrimers and the microtubules, as well as increase the electrostatic repulsion between microtubules that do not have the negative charges on their C-terminal tubulin tails shielded by bound dendrimers. Considering the second mechanism, it is known that microtubule disassembly increases with increasing pH.[91] Therefore, observing a decrease in microtubule bundling with increasing pH my be observed simply due to increased microtubule disassembly. To distinguish between these two possibilities, additional experiments, such as quantification of microtubule bundling in the presence of PAMAM dendrimers after cleavage of the anionic C-terminal tubulin tails using subtilisin,[92] must be performed.

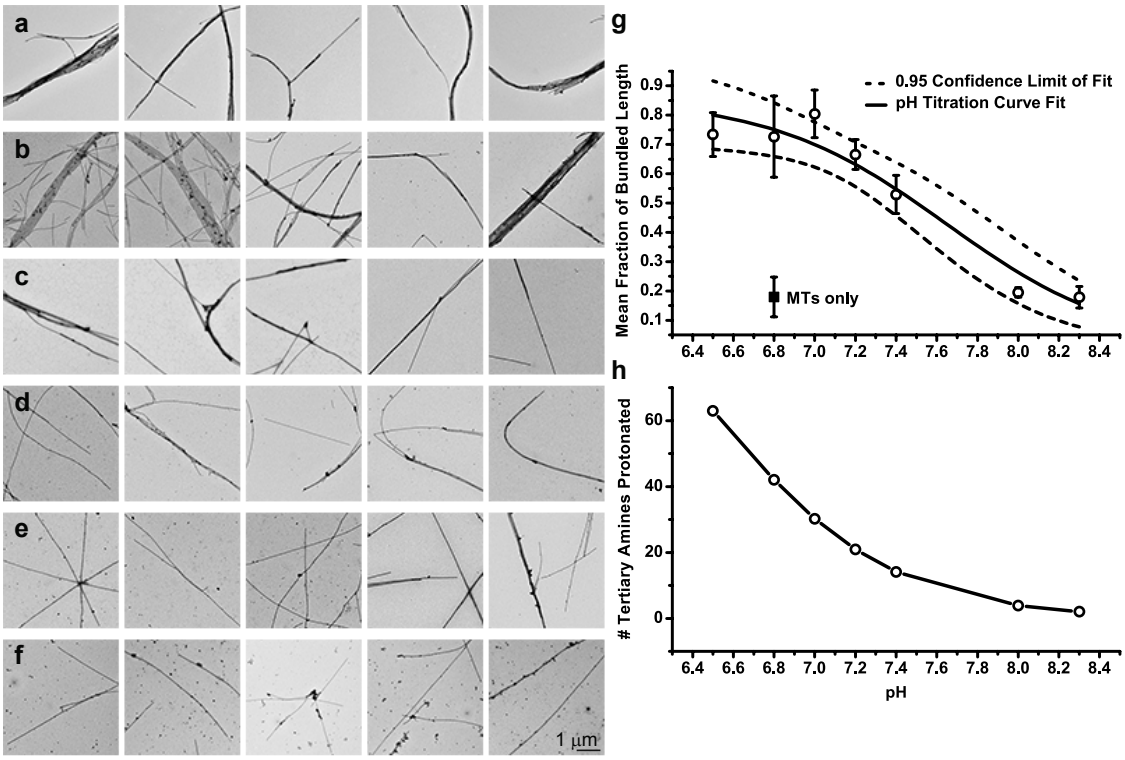

Figure 3.7: Negative stain TEM images obtained at 3,095x magnification (scale bar = 1 μm). Microtubules are incubated at room temperature with $PX_3Cy_{2-3}OH_{108}$-G5 for 30 min in MEM80, in which the pH has been adjusted with KOH to: (a) 6.5; (b) 7.0; (c) 7.2; (d) 7.4; (e) 8.0; or (f) 8.3. Bundling in each sample was estimated as before (g), from ten 25.38 μm^2 images from each of three trials, and a pH titration curve ($y = \frac{y_{max}}{1+10^{pH-pKa}} = \frac{0.86}{1+10^{pH-7.6}}$) was fit to the data ($R^2 = 0.94$). The amount of bundling in the absence of dendrimers is shown for reference (solid square labeled 'MTs only'). The Henderson-Hasselbalch equation ($y = \frac{126}{1+10^{pH-6.5}}$) is used to determine the theoretical number of protonated amines in the dendrimer core at the tested pH values (h).

Implications of Dendrimer-Induced Microtubule Structural Changes for Cancer Treatment

Both dendrimer-induced microtubule structural changes observed in this paper—stabilization of polymerizing microtubules and bundling of pre-formed microtubules—have the potential to stall mitosis in a dividing cell. In this respect, paclitaxel-conjugated dendrimers show promise for use as cancer therapeutics, even without, or upon slow, cleavage of the drug from the carrier. However, one of these structural changes was not specific to the cancer drug paclitaxel, but rather the dendrimer core itself.

Our previous study demonstrated that untargeted, surface neutralized G5 PAMAM dendrimers are not cytotoxic,[53,93] implying that paclitaxel, and less the dendrimer core, induces cytotoxicity. While differences in dendrimer concentration between the current study utilizing purified proteins and the prior study utilizing cultured cells may explain this difference, or the possibility that paclitaxel was cleaved from the dendrimer carrier intracellularly in the prior study, the current study underscores the need for exercising caution when designing dendrimer-conjugates for the treatment of diseases both responsive and non-responsive to paclitaxel, as the dendrimers may have unintended cytotoxic effects not specific to paclitaxel due to their potential direct electrostatic interactions with microtubules. More broadly, the current study highlights the need for careful toxicity studies to be performed and target cell specificity to be achieved to control for and avoid such side effects; not only when using PAMAM dendrimers as a carrier, but any other carrier molecules as well.

Nanoparticle toxicity is a topic that is very important to everyday life, as nanomaterials are being incorporated into a wide array of consumer products in addition to therapeutics.[94–96] Although it is recognized that nanoparticle toxicity stems from the ability of nanoparticles to cross cellular membranes, and that this ability derives from their small size[97] and surface charge,[66,98] it is not completely understood what the

molecular basis of the toxicity is, or what physicochemical properties of nanoparticles contribute to this toxicity.[96–98] The present study further emphasizes the need for additional studies addressing these questions, and advances a mechanism of cytotoxicity for flexible cationic nanoparticles involving interior, cationic tertiary amines.

Conclusions

In the present study, it is found that paclitaxel-conjugated, fifth generation, PAMAM dendrimers are able to affect microtubule structure *via* two mechanisms: (1) by stabilizing polymerizing microtubules; and (2) by bundling pre-formed microtubules. The latter mode of action is not specific to the activity of paclitaxel, as surface neutralized G5 PAMAM dendrimers that are not conjugated with paclitaxel are also able to bundle pre-formed microtubules to the same degree as paclitaxel-conjugated dendrimers. The mechanism for this bundling is at least partially electrostatically driven, mediated by tertiary amines located in the interior of the polyvalent dendrimer core that cannot be neutralized through chemical modifications. The results of this study, therefore, demonstrate both the promise of paclitaxel-conjugated dendrimers in the treatment of cancer and the necessity for further careful toxicity studies of these and other cationic nanoparticles.

CHAPTER IV

The Fluorescent Dyes Cy5 and TMR Induce Microtubule Bundling Through Hydrophobic Interactions[1]

4.1 Introduction

Nanoparticles are being increasingly incorporated into a wide array of consumer products,[94–96] making the study of their toxicity very important. Recently, nanoparticles have been considered for use as targeted drug delivery platforms[32,48,50] as they may allow attachment of many different molecules, including the drug, targeting molecules, and tracking/imaging molecules. In addition, nanoparticle attachment may improve the water solubility, membrane permeability, and release timing of a drug.[31]

Despite the increased utilization of nanoparticle technology, little is understood concerning any associated toxicity. It has been established, however, that the nanometer size of the particles increases toxicity as it: (1) increases their surface area, exposing more reactive sites of the particles; (2) facilitates movement of the particles across cellular and other internal barriers; and (3) enables their interaction with subcellular

[1]All tubulin was obtained from Edgar Meyhöfer. All modification and characterization of dendrimers was done by Ming-Hsin Li. All TEM images were taken using the microcope in the lab of Georgios Skiniotis.

structures, such as DNA and microtubules.[96] Besides their size, it is not completely understood what physicochemical properties of these nanoparticles may contribute to these toxic behaviors,[96–98] and if these properties may be altered or controlled so that their size is no longer a toxicity concern.

In addition to nanosize, nanoparticle charge has been implicated in nanotoxicity.[66,98] Indeed, the results of Chapter III in this dissertation shed light on one potential reason why charge may contribute to nanotoxicity. The results of this earlier chapter show that generation 5 (G5) polyamidoamine (PAMAM) dendrimers carrying no microtubule-targeting molecules are able to bundle microtubules to a very high degree *in vitro*.[99] It was determined that this bundling was electrostatically-driven, mediated by protonable tertiary amines in the dendrimer core that cannot be neutralized.

Formation of microtubule bundles *in vivo* is necessary for proper assembly of the mitotic machinery.[100] These bundles consist of only a few microtubules and are formed through cross-linking by various microtubule-associated proteins (MAPs).[82] Thick microtubule bundles, such as those observed in Chapter III of this dissertation, have also been observed to form *in vivo* when the neuronal microtubule binding protein, tau, is expressed in non-neuronal cells in high concentrations.[101] Tau was found to bundle microtubules by forming cross-bridges between them. Furthermore, this study found that cells with significant microtubule bundling could not proliferate.

One non-protein molecule has been reported to induce micotubule bundling. Spermine, a polyamine naturally present at high concentrations in all eukaryotic cells, was shown to bundle microtubules *in vitro*, but not aggregate or sequester free tubulin.[89] This is in contrast to the observed activity of tau in non-neuronal cells, which has been found to promote participation of free tubulin in the formation of thick microtubule bundles.[101] This phenomenon inhibits the degradation of β-tubulin mRNA, causing tubulin production to increase, which in turn promotes the formation of even

larger bundles.

Clearly, unregulated bundling and free tubulin aggregation—both observed to occur in the presence of G5 PAMAM dendrimers in Chapter III—would have drastic consequences for the cell, as strict regulation of microtubule dynamics is essential for proper chromosome movement during mitosis. Therefore, the results of Chapter III warrant investigation of the following: (1) whether other cationic nanoparticles can induce bundling; (2) what nanoparticle sizes, charge densities, and concentrations are required for the induction of bundling; and (3) whether nanoparticles can induce bundling *in vivo*. In the current study, these questions are addressed using various G5 PAMAM dendrimers. In doing so, convincing evidence is found that the fluorescent dyes, Cy5 and TMR, can enhance microtubule bundling through hydrophobic interactions.

4.2 Materials and Methods

Materials

MES, $MgCl_2$, and GTP were all purchased from Fisher Scientific (Waltham, MA). EGTA, paclitaxel, PCA, and PCD from Sigma-Aldrich (St. Louis, MO); Trolox from Acros Organics (Geel, Belgium); GMPCPP from Jena Biosciences (Jena, Germany); TMR from Molecular Probes (Eugene, OR); Cy succimidyl ester from GE Healthcare Life Sciences (Piscataway Township, NJ) and Cy5 analog (CyA; 2-[(1E,3E)-5-(3,3-Dimethyl-1-propyl-1,3-dihydro-2H-indol-2-ylidene)-1,3-pentadienyl]-3,3-dimethyl-1-propyl-3H-indolium iodide; CAS # 53213-98-2) from H.W. Sand Corp. (Jupiter, FL).

Tubulin Purification and Polymerization

Tubulin was purified from bovine brain and fluorescently labeled with TMR by Neha Kaul, Jenna Campbell, and Charles Chang Jiang in Edgar Meyhöfer's lab.

Briefly, tubulin was purified from bovine brain by two cycles of microtubule polymerization in the presence of a high-molarity PIPES buffer.[34] Tubulin was TMR-labeled by reacting polymerized microtubules with a 20-fold excess of TMR at room temperature for 30 min. Competent, TMR-labeled tubulin was purified from this mixture by repeated depolymerization and polymerization.[35]

For all experiments, microtubules were polymerized by incubating 2 mg/mL ($\approx$ 20 μM) α/β-tubulin dimers (using a mix of TMR-labeled and unlabeled tubulin dimers to achieve a final ratio of 1 TMR dye per 20 dimers, as determined by UV-Vis, where noted) with 4 mM $MgCl_2$ and 1 mM GTP in $MEM80_{6.8}$ buffer (80 mM MES-KOH, pH 6.8, 1 mM EGTA, 2 mM $MgCl_2$) at 37 °C for 30 min. After polymerization, the microtubules were stabilized with 10 μM paclitaxel.

G5 PAMAM Dendrimers

G5 PAMAM dendrimers were purchased from Dendritech, Inc. (Midland, MI). All modification, purification, and characterization of these dendrimers was done by Ming-Hsin Li, member of James R. Baker's lab, formerly at the University of Michigan. The dendrimers were first purified using a 10 kDa MWCO dialysis membrane, achieving a relatively monodisperse population (PDI = 1.01–1.05, determined by GPC).[38] The average number of primary amine end groups was determined to be 114 by potentiometric titration after purification by dialysis, membrane filtration, and lyophilization.[39] These dendrimers were then reacted with 5 molar equivalents of Cy5 NHS-ester to achieve an average of 2-3 Cy5 molecules per dendrimer, as determined by ^{1}H NMR and UV-Vis. The original terminal amine groups of the dendrimers were either neutralized by the addition of acetyl groups, or made negatively charged by the addition of carboxylic acid groups. A non-Cy5 control dendrimer was also identically synthesized, except it was not conjugated with Cy5, and its surface groups were neutralized by the addition of acetyl group. According to their surface chemistry and

stoichiometry, the G5 PAMAM dendrimers in this study will be referred to as: (1) $Cy_{2-3}(COOH)_{111}$-G5 (negative surface charge); (2) $Cy_{2-3}(OH)_{111}$-G5 (neutral surface charge); and (3) $(OH)_{114}$-G5 (neutral surface charge).

TIRFM

Imaging chambers were prepared by affixing a cover glass (No. 1.5, 24x30 mm, VWR, Radnor, PA) to a glass slide (Fischer Scientific, Waltham, MA) with double-sided sticky tape. After the imaging solution was flown into the imaging channel, the channel was sealed with candle wax. Images were taken on an inverted fluorescence microscope (model IX81, Olympus, Center Valley, PA) using a 60x objective lens. Samples were illuminated at either 532 nm (for TMR; type Compass 315M, Coherent Inc., Santa Clara, CA) or 635 nm (for Cy5; type Cube 640-100C, Coherent Inc., Santa Clara, CA) at the critical angle, using a cellˆ TIRF^{TM} Illuminator (Olympus, Center Valley, PA). Fluorescent emissions were split into four separate channels using a QV2 Quad View Imaging System (Photometrics, Tuscon, AZ) and projected onto an EMCCD camera (model Evolve 512, Photometrics, Tuscon, AZ). Fluorescent images were viewed using MetaMorph software (Molecular Devices, Sunnyvale, CA) and further processed using either ImageJ (NIH) and/or MATLAB (The MathWorks, Inc., Natick, MA).

TIRFM Bundling Assays

TMR-labeled, paclitaxel-stabilized microtubules were polymerized and stabilized as described above (see section Tubulin purification and polymerization) and incubated with either: (1) no additional components; (2) $Cy_{2-3}(COOH)_{111}$-G5; (3) PEG 600; (4) T7 RNA polymerase; or (5) Cy-PS at a 1:1 ratio (particle:tubulin dimers; both at ≈ 0.5 μM) in $MEM80_{6.8}$ with oxygen scavenging system (OSS; 5 mM PCA, 50 nM PCD, 2 mM Trolox) and 10μM paclitaxel for 30 min at room temperature

prior to visualization by TIRFM.

Quantifying Microtubule Bundling from TIRFM Images

The fraction of bundled microtubles in a sample was quantified using a custom script written in MATLAB (MathWorks, Natick, MA) (see Appendix D of this dissertation for code). Briefly, this script measures the intensity profile of a microtubule by taking cross-sectional line scans, perpendicular to the microtubule axis, at 5 pixel intervals. A Gaussian distribution is fit to each line scan and integrated to find the area under the curve, which corresponds to the total fluorescence intensity at that cross-section. The fluorescent intensity per unit length of a single, unbundled microtubule was assumed to be within two standard deviations of the mean, as extracted from the Gaussian fit, of the population distribution of microtubules measured in the absence of dendrimers. This intensity range was assigned a weight of 1. Additional weights for bundled microtubules were assigned as multiples of this range (dimers: weight = 2, trimers: weight = 3, *etc.*). Using this weighting system, each measured microtubule length was accordingly weighted and summed to determine the total fraction of bundled microtubules in the sample.

TEM

Carbon-coated copper mesh TEM grids were glow-discharged using a Solarus 950 (Gatan, Inc., Pleasanton, CA). Samples were placed on the carbon-coated side of the grid and negatively stained with a 0.75 % solution of uranyl formate.[60] It was assumed that the acidic pH of the stain would not significantly alter the pH of the sample as the stain would fix the sample in $\leq$ 10 ms.[61] Samples were imaged using a Morgagni 268 transmission electron microscope (FEI, Hillsboro, OR) in the lab of Georgios Skiniotis at the University of Michigan.

TEM Bundling Assays

TMR-labeled—or unlabeled, where indicated—microtubules were polymerized as described above (see section Tubulin purification and polymerization) and pelleted from unpolymerized tubulin by centrifugation (Airfuge, rotor A-100, Beckman, Fullerton, CA; 30 s at 30 psi). After centrifugation, microtubules were resuspended in $MEM80_{6.8}$ to an estimated 3.2 μM, based on the microtubule recovery efficiencies determined previously (data not shown). Microtubules (at 0.64 μM tubulin) were then incubated with either (1) 10 μM paclitaxel; (2) 0.64 μM $Cy_{2-3}(OH)_{111}$-G5; (3) 0.64 μM $(OH)_{114}$-G5; or (4) CyA (unconjugated Cy5 analog) in $MEM80_{6.8}$ for 30 min at room temperature prior to visualization by TEM.

For all salt bundling assays, 0.64 μM of $PX_3Cy_{2-3}OH_{108}$-G5 was used in the same protocol as above. $MgCl_2$ or KCl was added to $MEM80_{6.8}$ to a final concentration of 2-50 mM in excess of the salt already present in the buffer.

Quantifying Microtubule Bundling from TEM Images

The diameter of microtubule (bundles) in TEM images taken at 3,095x magnification was measured at 10 pixel intervals and the corresponding microtubule length was weighted according to the number of bundled microtubules determined to be in that length. The diameter of a single, unbundled microtubule, within two standard deviations from the mean, was assigned to the weight of 1, and this was used as a basis to assign diameter ranges to higher weights for bundled microtubules. The fraction of bundled microtubules in a sample was calculated as the fraction of bundled microtubule length per total measured microtubule length. This analytical process was automated using a MATLAB (MathWorks, Natick, MA) script written in-house.

Statistical Tests for Significance in Bundling

Statistical significance of the difference of mean bundled microtubule length between samples was tested using the Student's t-test, assuming equal variances, at significance level $\alpha = 0.05$. Prior to this test, it was verified that the two samples being compared had equal variances using the F-test at significance level $\alpha = 0.05$. All statistical tests were performed using the Statistics Toolbox in MATLAB (MathWorks, Natick, MA).

4.3 Results and Discussion

Implications of G5 PAMAM Dendrimer Cytotoxicity

From the advent of their design, G5 PAMAM dendrimers have been of interest to the drug development field as potential drug carriers for targeted delivery due to their water solubility and high multi-valency.[44,48] In their native state, PAMAM dendrimers are terminated by primary amines, which are positively charged at a neutral pH. It has been found that the high cationic surface charge of these dendrimers makes them cytotoxic as it allows them to poke holes in cellular membranes.[66,93] These previous studies showed that neutralizing $> 80\%$ of the dendrimer's terminal amine groups eradicates their cytotoxicity. However, the results in Chapter III of this dissertation show that high concentrations of G5 PAMAM dendrimers will induce microtubule bundling *in vitro*, even when 100 % of the terminal amine groups are neutralized. These dendrimers were found to bundle microtubules *via* electrostatic interactions between internal protonable amines in their core—which cannot be neutralized—and the microtubule surface.[99] Therefore, the cytotoxicity of PAMAM dendrimers warrants additional investigation.

Increases in Ionic Strength Correspond to Decreases in Microtubule Bundling

To better understand dendrimer-induced microtubule bundling (Chapter III), the effects of buffer ionic strength were first tested. If dendrimer-induced bundling is mediated by electrostatics, then an increase in buffer ionic strength will correspond with a decrease in bundling. To test this hypothesis, TEM bundling assays were used as before (Chapter III), except that 2-50 mM $MgCl_2$ or KCl were added to $MEM80_{6.8}$ (80 mM MES-KOH, pH 6.8, 1 mM EGTA, 2 mM $MgCl_2$). Note that the condition "2 mM $MgCl_2$" corresponds to $MEM80_{6.8}$ with no additional salt. The paclitaxel-conjugated, Cy5-labeled, surface-neutralized dendrimers, $PX_3Cy_{2-3}OH_{108}$-G5, were used for all experiments (see Chapter III).

Figure 4.1 shows the fraction of unbundled microtubules (represented as unbundled length) measured at each salt concentration. An increase in salt concentration (buffer ionic strength) does indeed correlate with a decrease in bundling. The Hill equation, $(y = y_0 + (1 + \frac{K_A}{[salt]})^{-1})$, was fit to each data set with $R^2 = 0.93$ for $MgCl_2$ and $R^2 = 0.83$ for KCl. From the fits, half-saturation concentrations (K_A) of 3.9 mM $MgCl_2$ and 0.72 mM KCl were extracted. Note that the tubulin and dendrimer concentration used in these experiments was 0.64 μM. This bundling salt-dependence supports our earlier hypothesis that bundling is mediated by electrostatics.

The Fluorescent Dyes TMR and Cy5 Contribute to Microtubule Bundling

To complete our exploration of the mechanisms of dendrimer-induced microtubules bundling, the contribution of the fluorescent labels used in these experiments—Cy5 (dendrimers) and TMR (tubulin) was examined next. Both dyes are hydrophobic with multiple aromatic rings (Figure 4.2), creating the possibility for dye-dye hydrophobic interactions that may mediate microtubule bundling. If these dyes are found to contribute to bundling, it will underscore a need for caution to be used when considering

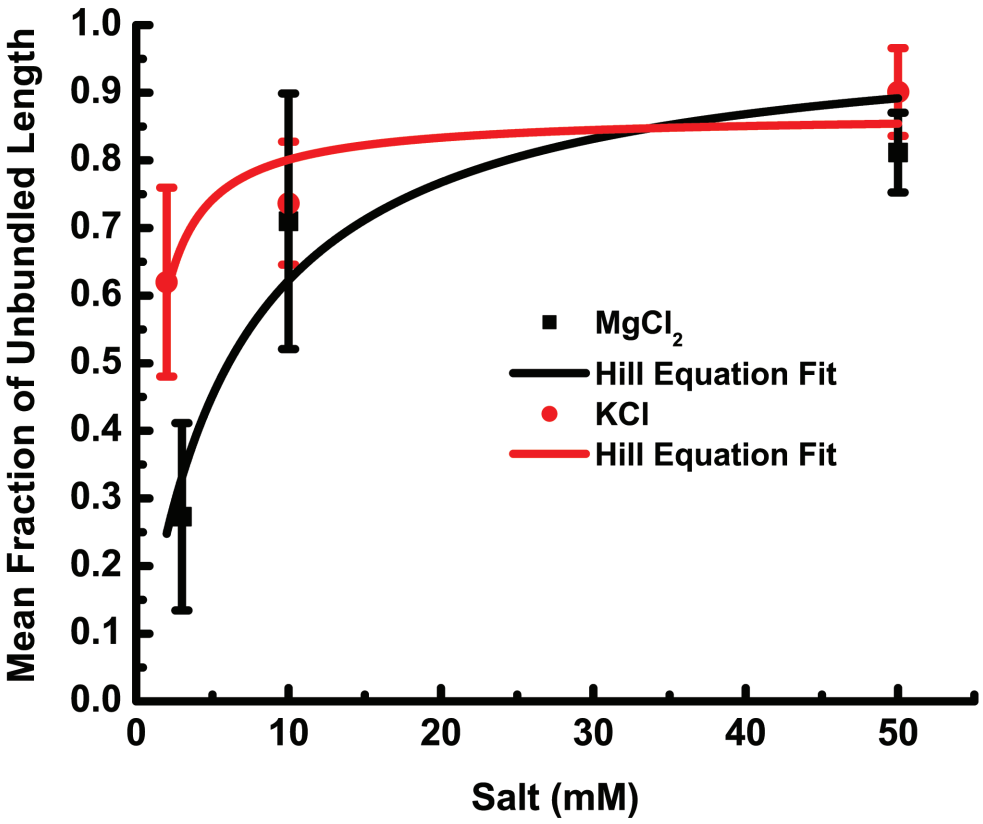

Figure 4.1: Microtubules were incubated with $PX_3Cy_{2-3}OH_{108}$-G5 at a 1:1 ratio of dendrimers:tubulin dimers in $MEM80_{6.8}$ with 2-50 mM $MgCl_2$ or KCl. Note that the condition "2 mM $MgCl_2$" represents $MEM80_{6.8}$ without any additional salt. The mixtures were incubated together for 30 min at room temperature and then visualized by TEM. The Hill equation ($y = y_0 + (1 + \frac{K_A}{[salt]})^{-1}$) was fit to each data set with the following parameters: (1) K_A = 3.9 mM $MgCl_2$, R^2 = 0.93; and (2) K_A = 0.72 mM KCl, $R^2 = 0.83$.

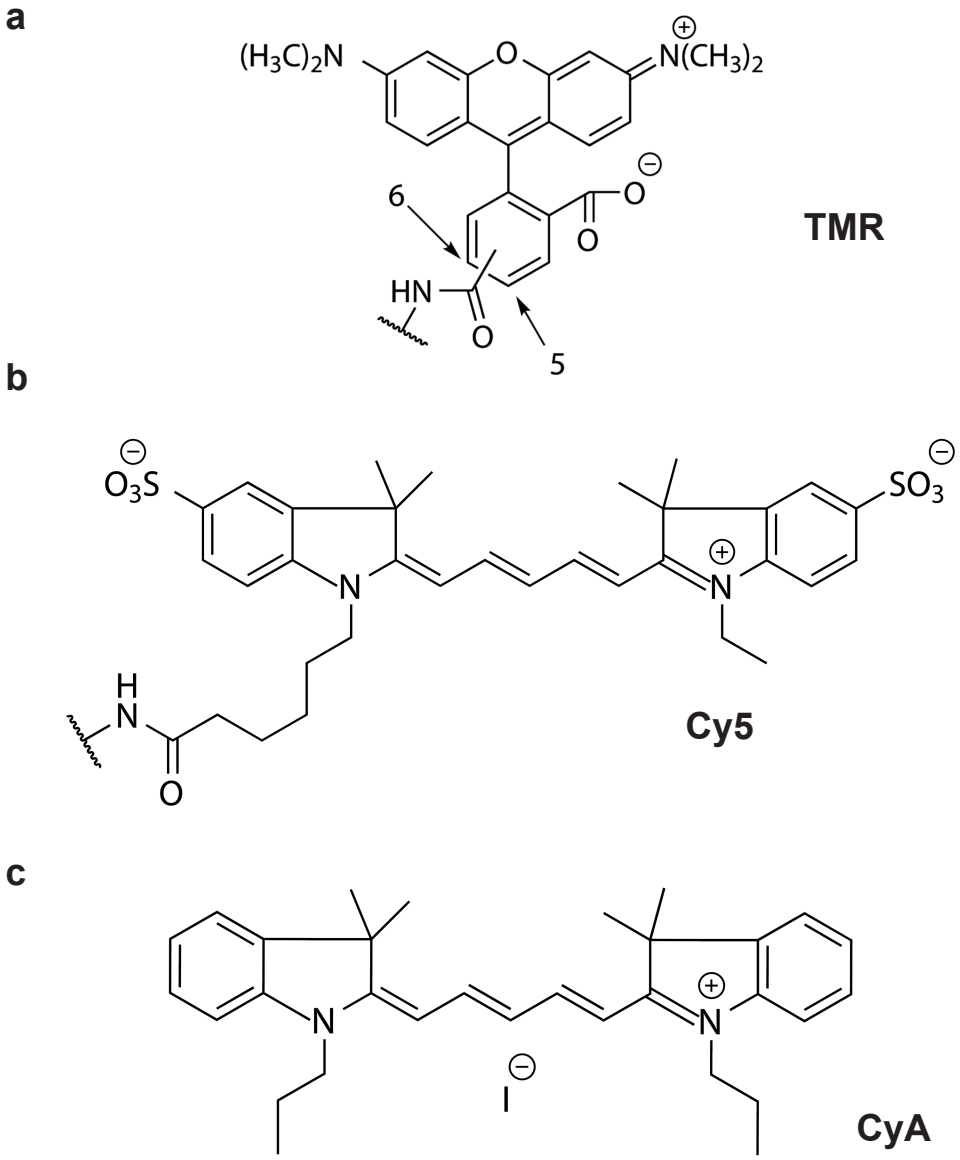

Figure 4.2: Chemical structures of (a) TMR (5-(6)-carboxytetramethylrhodamine succimidyl ester); (b) Cy5; and (c) CyA (unconjugated Cy5 analog) showing dendrimer attachment points.

attachment of aromatic molecules to drug delivery platforms (*e.g.*, dendrimers).

The contribution of Cy5 to dendrimer-induced bundling was tested using TEM bundling assays with either: (1) $(OH)_{114}$-G5 at a 1:1 ratio of dendrimers:tubulin dimers; or (2) CyA at a 3:1 ratio. CyA is a Cy5 analog, chosen for its lack of chemical reactivity and functionality (Figure 4.2c). CyA was tested at a 3:1 ratio with tubulin in order to correspond to the Cy5 concentration contributed by the dendrimers (the dendrimers are labeled with 2-3 Cy5 each). Bundling was quantified as in Chapter III, from 30 x (4.9 μm)^2 TEM images.

For reference, the levels of TMR-labeled microtubule bundling found in the absence or presence of $Cy_{2-3}(OH)_{111}$-G5 in Chapter III are shown in columns 1 and 2, respectively, of Figure 4.3. To determine the contribution of the conjugated Cy5 to the high levels of observed bundling in the presence of $Cy_{2-3}(OH)_{111}$-G5, $(OH)_{114}$-G5 were next tested. This dendrimer is chemically identical to $Cy_{2-3}(OH)_{111}$-G5, except that it does not have Cy5 conjugated to its surface. As seen in Figure 4.3, removing Cy5 from the dendrimer eradicates its ability to bundle microtubules. Furthermore, when CyA, a Cy5 analog (Figure 4.2c), was incubated with microtubules, the level of microtubule bundling again increased (Figure 4.3). This level of bundling was significantly greater than that measured in the presence of $(OH)_{114}$-G5 ($p < 0.05$), but not significantly different from that measured in the presence of $Cy_{2-3}(OH)_{111}$-G5. This suggests that Cy5, conjugated to dendrimers or not (as CyA), induces high levels of microtubule bundling.

Cy5 Induces Microtubule Bundling Even When Conjugated to Highly Anionic Dendrimers

To further test this observation that Cy5 makes a large contribution to dendrimer-induced bundling, $Cy_{2-3}(COOH)_{111}$-G5 were tested for an ability to bundle microtubules. These dendrimers are labeled with Cy5 and carry a high anionic surface

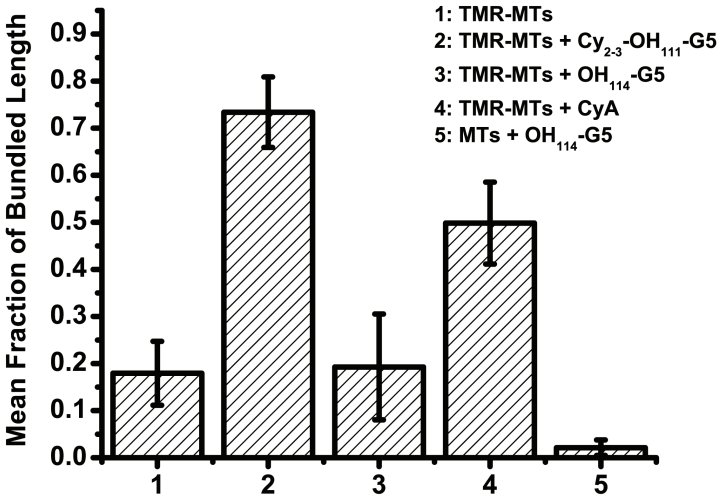

Figure 4.3: Quantification of TMR-labeled (TMR-MTs), or unlabeled (MTs), microtubule bundling from TEM images in the presence of various dendrimers or CyA (unconjugated Cy5 analog).

charge (1.4 (-)/nm^2) from carboxylate groups. The high anionic surface charge density of these dendrimers should cause them to be electrostatically repelled from the anionic microtubule surface. This experiment was visualized by TIRFM instead of TEM, but all experimental conditions were the same (with the exception of the addition of OSS).

The method used for quantifying bundling from TIRFM images (see Appendix E) is very similar to that used previously for TEM images (see Appendix D). Briefly, the fluorescence intensity profile is measured at cross-sections of the microtubules at 5 px intervals. Each profile is fit with a Gaussian distribution, and the area under the curve (corresponding to the total fluorescence intensity at that cross-section) is determined. The fluorescent intensity per unit length of a single, unbundled microtubule is assumed to be within two standard deviations of the mean of the population distribution of microtubules measured in the absence of dendrimers. This intensity range is assigned a "weight" of 1. Additional weights for bundled microtubules are assigned as multiples of this range (*i.e.* dimers: weight = 2, trimers: weight = 3, *etc.*). Using this weighting system, each measured microtubule length is weighted accordingly, and summed to determine the total fraction of bundled microtubules in the sample.

Figure 4.4a shows microtubules in the absence of dendrimers, identified as "green rods." When microtubules are incubated with $Cy_{2-3}(COOH)_{111}$-G5 (Figure 4.4b), some green rods—one example in this image is indicated by an arrow—appear to have a greater width, as if they might be bundles of microtubules. The other microtubules may be either unbundled, or smaller bundles that are not thick enough to distinguish from unbundled microtubules by eye, due to the resolution of light microscopy. Indeed, upon quantification of bundling (Figure 4.4c) it is found that $Cy_{2-3}(COOH)_{111}$-G5 bundles microtubules to a significant degree ($p < 0.05$). Furthermore, this level of bundling is not significantly different than that measured in the presence of $PX_3Cy_{2-3}OH_{108}$-G5 or $Cy_{2-3}OH_{111}$-G5 from TEM images in Chapter III

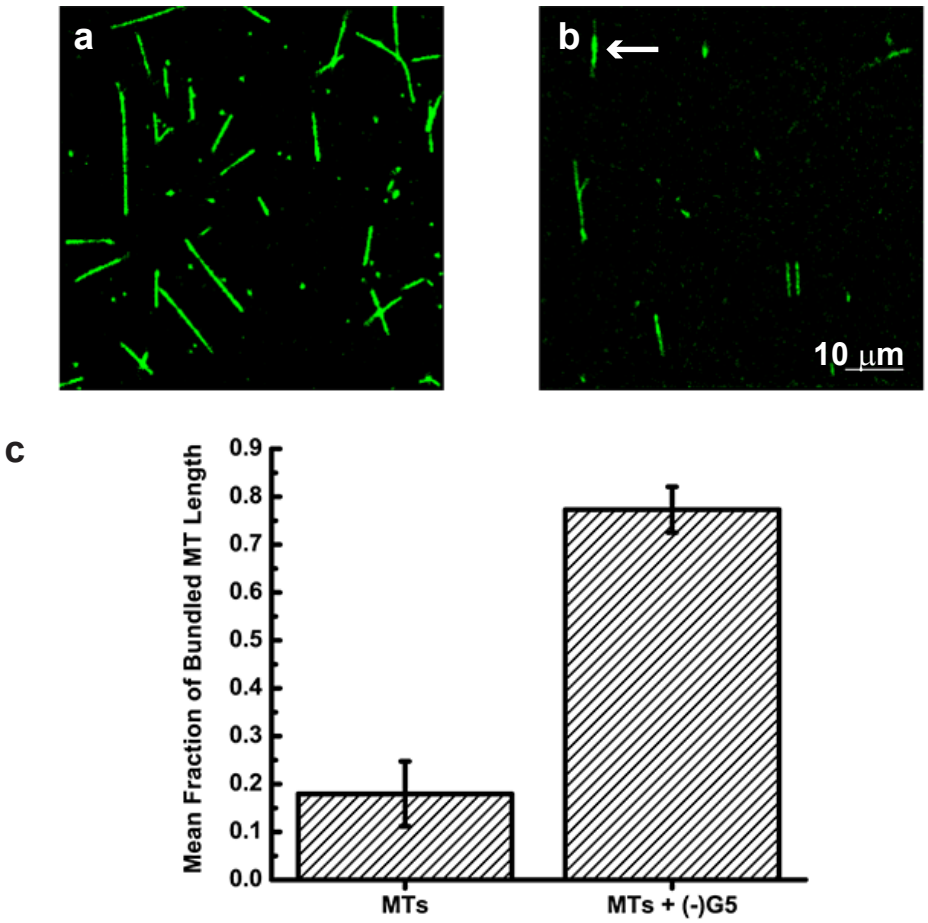

Figure 4.4: Microtubules were incubated with either (a) no additional components or (b) $Cy_{2-3}(COOH)_{111}$-G5 at a 1:1 ratio of dendrimers:tubulin dimers in $MEM80_{6.8}$ for 30 min at room temperature prior to visualization by TIRFM. The white arrow indicates a potential [large] bundle of microtubules. The other microtubules may be either unbundled, or smaller bundles that are not thick enough to distinguish from unbundled microtubules by eye, due to the resolution of light microscopy. Only the image from the TMR channel (green: microtubules) is shown. Scale bar represents 10 μm. (c) The amount of bundling in each sample was measured from the quantity of microtubules observed on ≥ 14 m^2 of coverslip surface, and represented as the fraction of total microtubule length bundled.

($p > 0.05$).

Together these observations imply that Cy5 significantly contributes to the dendrimer-induced bundling. This raises the question of whether there is free dye present in the dendrimer preparation. However, this is not likely as following the Cy5 conjugation reaction, the dendrimers were purified by MWCO 10 kD ultrafiltration and six runs of 10 kD dialysis (see Appendix A). Therefore, any elevated bundling observed in the presence of Cy5-conjugated dendrimers is likely due to the conjugated Cy5 and not contaminating free Cy5.

Next, to determine the contribution of the TMR label on the tubulin to dendrimer-induced bundling, TEM bundling assays were performed with $(OH)_{114}$-G5 exactly as before except without the TMR label on the tubulin. As can be seen in column 5 of Figure 4.3, in the absence of Cy5 and TMR, only 2 % of the total population is bundled. This amount of bundling is significantly different from that measured with TMR-labeled microtubules, both in the presence or absence of $(OH)_{114}$-G5 ($p < 0.05$). Therefore, it can be concluded from all of the above data that Cy5 (whether free or coupled to dendrimers) and TMR (while coupled to tubulin) are able to induce bundling of microtubules, likely through hydrophobic interactions with each other.

Conclusions

G5 PAMAM dendrimer-induced microtubule bundling is likely induced by a combination of: (1) electrostatic interactions involving protonatable tertiary amines in the dendrimer core (Figure 3.1); and (2) hydrophobic interactions involving aromatic dyes conjugated to the dendrimer (Cy5) and tubulin (TMR). The hydrophobic dye interactions appear to have an overall greater contribution to bundling than electrostatic interactions (Figure 4.3). This suggests that the pH-dependence of bundling (Figure 3.7) may also be due to microtubule instability at alkaline pH,[91] in addition to electrostatic interactions.

The large contribution of dendrimer-coupled Cy5 to microtubule bundling is likely a function of its concentration in these experiments. It is possible that lower Cy5 concentrations may reduce bundling. Indeed, this study found that TMR coupled to microtubules, which was present in the experiments in concentrations 40-60 fold less than Cy5, induced a lower level of bundling than Cy5. Therefore, the concentration limit of bundling induced by Cy5, or any other aromatic, hydrophobic compound such as a drug, must first be precisely determined before such molecules are considered for use in imaging and therapeutic nanomedicines.

Overall, the conclusions of this chapter suggest that the bundling observed in Chapter III may not be clinically relevant as it is dependent on dendrimer and dye concentrations that may be too high to be clinically relevant. Nevertheless, the paclitaxel-conjugated G5 PAMAM dendrimers studied were still able promote microtubule polymerization and stabilization in a paclitaxel-dependent manner, although not as efficiently as free paclitaxel. These data motivate further development of paclitaxel-nanoparticle conjugates that can polymerize and stabilize (and possibly bundle) microtubules as effectively as free paclitaxel, and/or effectively release their paclitaxel cargo in the cell. Finally, these nanoparticle carriers, and any conjugated imaging molecules, must be carefully tested for cytotoxic effects in the absence of any paclitaxel.

CHAPTER V

Paclitaxel-Conjugated Gold Nanoparticles Show Promise as a Targeted Cancer Drug Delivery Strategy[1]

5.1 Introduction

Paclitaxel is a small organic molecule originally isolated from the Pacific yew tree in 1962. Its cytotoxicity was demonstrated subsequently in several experimental systems, thereby initiating interest in its potential as an anti-cancer therapeutic.[102,103] In 1979, Schiff *et al.*[104] discovered the mechanism of paclitaxel cytotoxicity: promotion of microtubule polymerization and stabilization of microtubules against depolymerization. Soon after, Bristol-Myers Squibb (New York, NY) began clinical trials on paclitaxel, and now markets the molecule as the anti-cancer drug Taxol®, indicated for various types of cancer, including ovarian, breast, lung and AIDS-related Kaposi's sarcoma.

Even though paclitaxel is a very effective anti-tumor agent,[29] like many chemotherapeutic agents, its use is accompanied by detrimental side effects primarily arising from its poor water solubility and promiscuous cytotoxicity.[30] For example, in order

[1]TMR-tubulin was obtained from Edgar Meyhöfer. All AuNPs were synthesized by Seok Ki Choi. All TEM images were taken using the microcope in the lab of Georgios Skiniotis.

to compensate for its poor water solubility, Taxol® is currently solubilized in a very toxic mixture of polyethoxylated castor oil and ethanol prior to injection into the patient.[30] Given the detrimental side effects associated with this preparation, it is very desirable to develop a water-soluble, targeted delivery strategy for paclitaxel.

Nanoparticles have been of great interest to the targeted drug delivery field in recent decades due to their inherent properties such as their capacity for multivalent attachments, ability to cross cellular membranes, and imaging capabilities.[105] Accordingly, at least two examples of paclitaxel-conjugated nanoparticles are currently on the market, attempting to increase the efficacy, and decrease the side effects, of paclitaxel for treatment. Abraxane™, marketed in the US by Celgene (Summit, NJ), utilizes albumin as a nanoparticle delivery vehicle for paclitaxel. Nanoxel™, marketed in India by Dabur Pharma (India), utilizes another type of polymeric nanoparticle delivery vehicle (a co-polymer of N-isopropyl acrylamide and vinyl pyrrolidone).[106] Although both treatments are an improvement upon Taxol® because they are more water soluble and increase the amount of paclitaxel delivery to the tumor sites, they nevertheless still cause harmful side effects in patients,[107] potentially due, at least in part, to the fact that neither formulation contains any molecules to specifically target delivery of paclitaxel to cancerous cells. Therefore, further improvement upon paclitaxel delivery methods is warranted.

Gold nanoparticles (AuNPs) have a unique set of physical, chemical, and photonic properties among nanoparticles that makes them attractive for use in targeted drug delivery applications.[108,109] For example, AuNPs provide good radiation therapy contrast, photo-imaging contrast, and spectrochemical diagnostic contrast.[110] Already, there have been a few reported examples of paclitaxel-conjugated AuNPs synthesized.[106] One of these conjugates has severn increased cytotoxcity compared to paclitaxel *in vitro*, however further testing of these conjugates is necessary.

AuNPs provide multiple options for carrying and releasing drugs to the target

site. For example, one method takes advantage of the strong Au-S bond to conjugate thiolated drugs to the AuNP surface. Once the conjugated AuNPs are internalized into a cell, the reductive peptide glutathione (GSH), present in high concentrations inside the cell, exchanges with the drug, freeing the drug for therapeutic action. The intracellular concentrations of GSH are much higher than extracellular concentrations, promoting the selective release of the drug inside the cell, rather than outside.[111]

In the current study, AuNPs of multiple diameters are tested, to which paclitaxel has been conjugated *via* thiol bonds (Figure 5.1), for their microtubule stabilizing capabilities *in vitro* using total internal reflection fluorescence microscopy (TIRFM) and transmission electron microscopy (TEM). Preliminary evidence is presented that these AuNPs are capable of: (1) promoting microtubule polymerization; (2) stabilizing microtubules; and (3) bundling microtubules. Therefore, further testing of these paclitaxel-conjugated AuNPs as drug delivery vehicles with the attachment of tumor-targeting ligands is warranted.

5.2 Materials and Methods

Materials

MES, $MgCl_2$, and GTP were all purchased from Fisher Scientific (Waltham, MA). EGTA, paclitaxel, PCA, and PCD from Sigma-Aldrich (St. Louis, MO); Trolox from Acros Organics (Geel, Belgium); TMR from Molecular Probes (Eugene, OR); and HiLyte488 and unlabeled tubulin from porcine brain from Cytoskeleton, Inc. (Denver, CO).

Tubulin Purification and Polymerization

Tubulin was purified from bovine brain and fluorescently labeled with TMR by Neha Kaul, Jenna Campbell, and Charles Chang Jiang in Edgar Meyhöfer's lab.

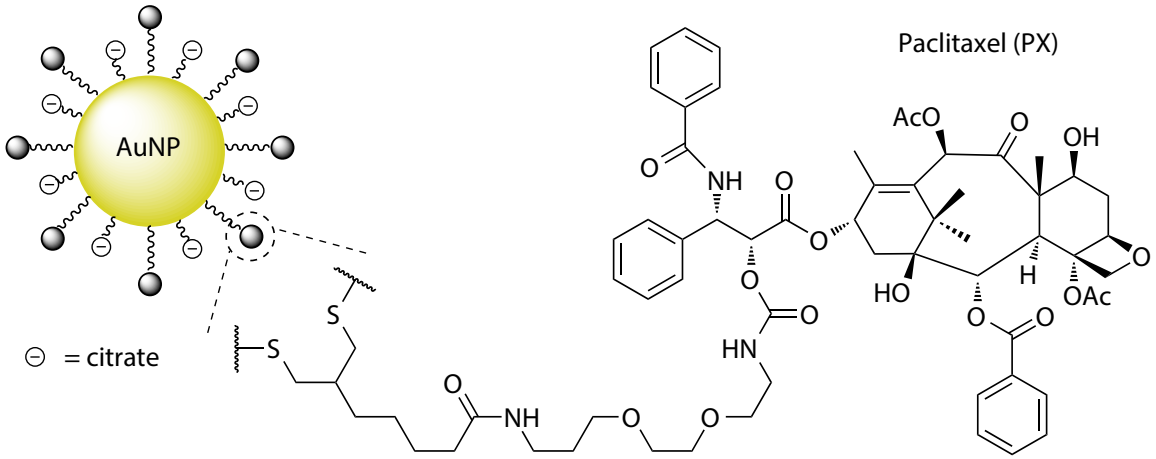

Figure 5.1: General two-dimensional schematic of the paclitaxel-conjugated gold nanoparticles (AuNPs) used in this study, showing citrate stabilization and paclitaxel conjugation *via* Au-S bonds.

Briefly, tubulin was purified from bovine brain by two cycles of microtubule polymerization in the presence of a high-molarity PIPES buffer.[34] Tubulin was TMR-labeled by reacting polymerized microtubules with a 20-fold excess of TMR at room temperature for 30 min. Competent, TMR-labeled tubulin was purified from this mixture by repeated depolymerization and polymerization.[35]

For all experiments, microtubules were polymerized by incubating 2 mg/mL ($\approx$ 20 μM) α/β-tubulin dimers (using a mix of TMR-labeled and unlabeled tubulin dimers to achieve a final ratio of 1 TMR dye per 20 dimers, as determined by UV-Vis, where noted) with 4 mM $MgCl_2$ and 1 mM GTP in $MEM80_{6.8}$ buffer (80 mM MES-KOH, pH 6.8, 1 mM EGTA, 2 mM $MgCl_2$) at 37 °C for 30 min. After polymerization, the microtubules were stabilized with 10 μM paclitaxel.

Paclitaxel-Conjugated Gold Nanoparticles

Paclitaxel-conjugated gold nanoparticles were synthesized by Seok Ki Choi, member of James R. Baker's lab, formerly of the University of Michigan. The particles were citrate-stabilized and conjugated to the fullest extent possible with paclitaxel *via* thiol bonds. The number of paclitaxel molecules per particle has not yet been characterized. Four different samples of paclitaxel-conjugated particles were prepared, of the following sizes: 48 nm, 20 nm, and two different samples with sizes distributed between 10-20 nm. These particles will referred to throughout the manuscript as PX-cit-Au48, PX-cit-Au20, PX-cit-Au10a, and PX-cit-Au10b, according to their diameters. As a negative control, 48 nm citrate-stabilized gold nanoparticles were synthesized in parallel with PX-cit-Au48, except that paclitaxel was not attached. This particle will be referred to as cit-Au48 throughout the manuscript. At this time, no non-paclitaxel negative controls have been synthesized for PX-cit-Au20, PX-cit-Au10a, or PX-cit-Au10b.

TIRFM

Imaging chambers were prepared by affixing a cover glass (No. 1.5, 24x30 mm, VWR, Radnor, PA) to a glass slide (Fischer Scientific, Waltham, MA) with double-sided sticky tape. After the imaging solution was flown into the chamber, the chamber was sealed with candle wax. Images were taken on an inverted fluorescence microscope (model IX81, Olympus, Center Valley, PA) using a 60x objective lens. Samples were illuminated at either 532 nm (for TMR; type Compass 315M, Coherent Inc., Santa Clara, CA) or 635 nm (for Cy5; type Cube 640-100C, Coherent Inc., Santa Clara, CA) at the critical angle, using a cellˆ TIRF^{TM} Illuminator (Olympus, Center Valley, PA). Fluorescent emissions were split into four separate channels using a QV2 Quad View Imaging System (Photometrics, Tuscon, AZ) and projected onto an EMCCD camera (model Evolve 512, Photometrics, Tuscon, AZ). Fluorescent images were viewed using MetaMorph software (Molecular Devices, Sunnyvale, CA).

TIRFM Bundling Assays

HiLyte488-labeled, paclitaxel-stabilized microtubules were polymerized and stabilized as described above (see section Tubulin purification and polymerization) and incubated with either: (1) no additional components; (2) PX-cit-Au10a; (3) PX-cit-Au10b; (4) PX-cit-Au20; (5) PX-cit-Au48; or (6) cit-Au48 at a 1:1 ratio (particle:tubulin dimers; both at $\approx$ 60 nM) in MEM80$_{6.8}$ with oxygen scavenging system (OSS; 5 mM PCA, 50 nM PCD, 2 mM Trolox) and 10μM paclitaxel for 30 min at room temperature prior to visualization by TIRFM.

Quantifying Microtubule Bundling from TIRFM Images

The fraction of bundled microtubles in a sample was quantified using a custom script written in MATLAB (MathWorks, Natick, MA) (see Appendix D of this dissertation for code). Briefly, this script measures the intensity profile of a microtubule

by taking cross-sectional line scans, perpendicular to the microtubule axis, at 5 pixel intervals. A Gaussian distribution is fit to each line scan and integrated to find the area under the curve, which corresponds to the total fluorescence intensity at that cross-section. The fluorescent intensity per unit length of a single, unbundled microtubule was assumed to be within two standard deviations of the mean, as extracted from the Gaussian fit, of the population distribution of microtubules measured in the absence of dendrimers. This intensity range was assigned a weight of 1. Additional weights for bundled microtubules were assigned as multiples of this range (dimers: weight = 2, trimers: weight = 3, *etc.*). Using this weighting system, each measured microtubule length was accordingly weighted and summed to determine the total fraction of bundled microtubules in the sample.

TEM

Carbon-coated copper mesh TEM grids were glow-discharged using a Solarus 950 (Gatan, Inc., Pleasanton, CA). Samples were placed on the carbon-coated side of the grid and negatively stained with a 0.75 % solution of uranyl formate.[60] It was assumed that the acidic pH of the stain would not significantly alter the pH of the sample as the stain would fix the sample in $\leq$ 10 ms.[61] Samples were imaged using a Morgagni 268 transmission electron microscope (FEI, Hillsboro, OR).

TEM Polymerization Assays

2.0 mg/mL of a mix of unlabeled and TMR-labeled (see Tubulin Purification and Polymerization above) tubulin ($\approx$ 20 μM) was mixed with 4 mM $MgCl_2$ and either (1) no additional components; (2) 20 μM paclitaxel; (3) 10 nM PX-cit-Au20; (4) 10 nM PX-cit-Au48; or (5) 10 nM cit-Au48 in $MEM80_{6.8}$ at 37 °C for 20 min, then room temperature for 90 min. The resulting mixtures were then imaged by TEM.

Quantitative Analysis of Microtubule Bundling in TEM Images

The diameter of microtubule (bundles) in TEM images taken at 3,095x magnification was measured at 10 pixel intervals and the corresponding microtubule length was weighted according to the number of bundled microtubules determined to be in that length. The diameter of a single, unbundled microtubule, within two standard deviations from the mean, was assigned to the weight of 1, and this was used as a basis to assign diameter ranges to higher weights for bundled microtubules. The fraction of bundled microtubules in a sample was calculated as the fraction of bundled microtubule length per total measured microtubule length. This analytical process was automated using a MATLAB (MathWorks, Natick, MA) script written in-house.

Statistical Tests for Significance in Bundling

Statistical significance of the difference of mean bundled microtubule length between samples was tested using the Student's t-test, assuming equal variances, at significance level $\alpha = 0.05$. Prior to this test, it was verified that the two samples being compared had equal variances using the F-test at significance level $\alpha = 0.05$. All statistical tests were performed using the Statistics Toolbox in MATLAB (MathWorks, Natick, MA).

5.3 Results and Discussion

Paclitaxel-Conjugated Nanoparticles May Promote Microtubule Polymerization in the Absence of GTP

One of the cytotoxic properties of paclitaxel is its ability to promote microtubule polymerization in the absence of GTP or microtubule-associated proteins (MAPs).[104] In the cell, abnormal microtubule polymerization would disrupt the normal cellular functions, as strict regulation of microtubule dynamics is essential for proper chro-

mosome movement during mitosis. Therefore, it was first tested if conjugation to the gold nanoparticle (AuNP) disrupts the ability of paclitaxel to promote microtubule polymerization *in vitro*. To test the ability of the paclitaxel-conjugated AuNPs to promote microtubule polymerization, 2 mg/mL tubulin was incubated with 4 mM $MgCl_2$ and either (1) no additional components; (2) 20 μM paclitaxel; (3) 10 nM PX-cit-Au20; (4) 10 nM PX-cit-Au48; or (5) 10 nM cit-Au48 in $MEM80_{6.8}$ at 37 °C for 20 min to encourage polymerization, then room temperature for 90 min to test stability of any polymerized microtubules.

Figure 5.2 shows the results of these experiments. Figure 5.2a shows microtubules formed in the presence of free paclitaxel, in a 1:1 ratio of paclitaxel:tubulin dimers. If no paclitaxel is present, only tubulin aggregates are observed. Some of these tubulin aggregates appeared to be roughly the same shape as microtubules (Figure 5.2b). However, visualization at high magnification (24,628x; bottom row of Figure 5.2b) shows that these stalk-like aggregates do not show the characteristic tubulin patterns of a well-formed microtubules. Only a few of these stalk-like aggregates were observed over more than $(5\ \mu m)^2$ of grid area searched. In the presence of PX-cit-Au20, in a 1:2,000 ratio of AuNPs:tubulin dimers, well-formed microtubules were observed (Figure 5.2c). In the presence of PX-cit-Au48, in a 1:2,000 ratio of AuNPs:tubulin dimers, microtubules were observed with normal tubulin patterning, but apparently more protofilaments than usual (Figure 5.2d). In contrast, in the presence of cit-Au48, in a 1:2,000 ratio of AuNPs:tubulin dimers, only tubulin aggregates were observed (Figure 5.2e), although none of the stalk-like aggregates were observed as in Figure 5.2b.

As expected, no well-formed microtubules are formed in the absence of paclitaxel (Figure 5.2b). Therefore, if any microtubules are observed in the presence of PX-cit-Au20 or PX-cit-Au48, this would suggest that the conjugated paclitaxel retains its ability to promote polymerization and stabilization of microtubules. Indeed, mi-

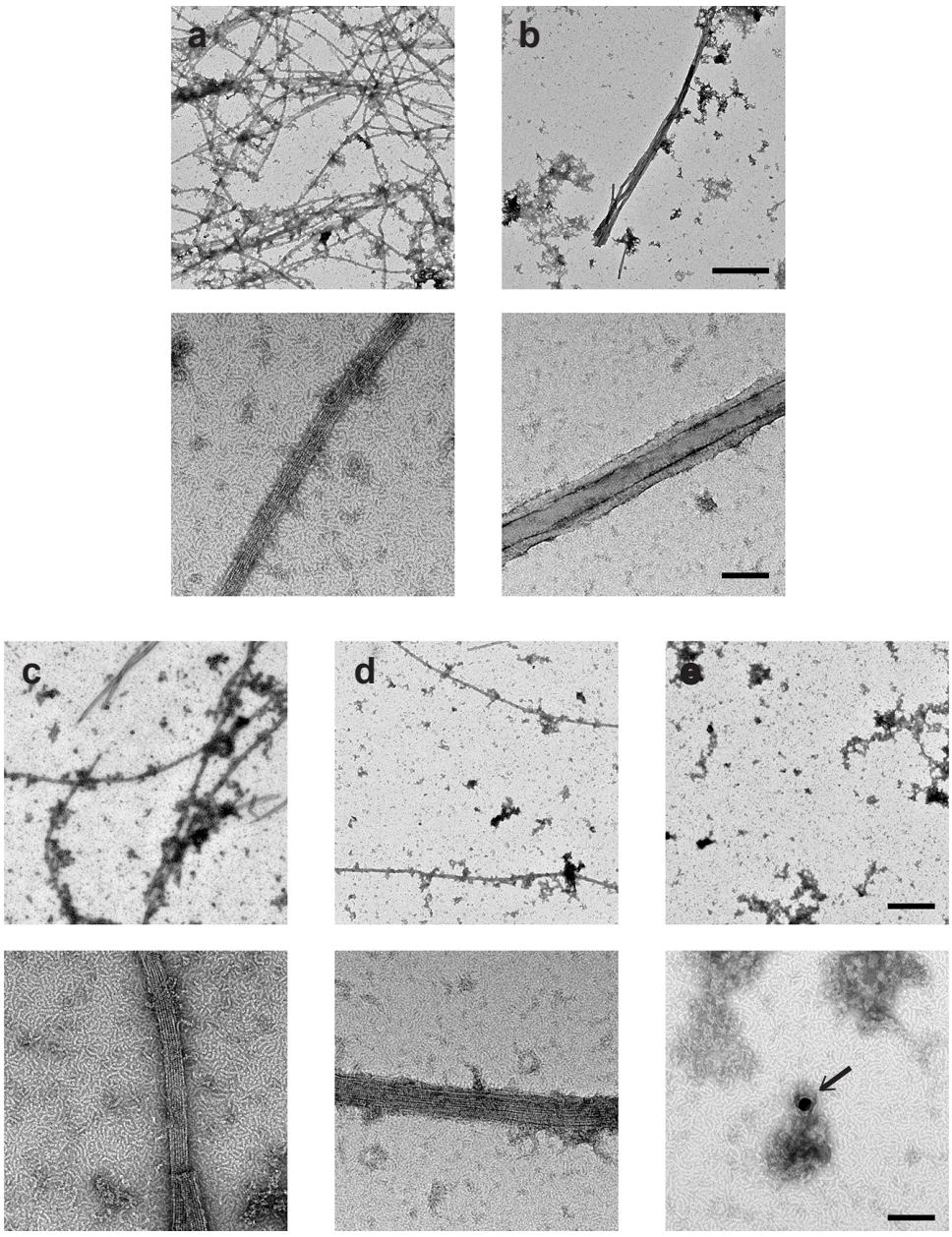

Figure 5.2: Negative-stain TEM images obtained at 3,095x (top row; scale bar = 1 μm) or 24,628x magnification (bottom row; scale bar = 100 nm). 2 mg/mL tubulin was incubated with 4 mM $MgCl_2$ and either (a) no additional components; (b) 20 μM paclitaxel; (c) 10 nM PX-cit-Au20; (d) 10 nM PX-cit-Au48; or (e) 10 nM cit-Au48 in $MEM80_{6.8}$ at 37 °C for 20 min, then room temperature for 90 min. The black arrow in (e) indicates a AuNP.

crotubules are observed in the presence of both of these AuNPs (Figures 5.2c-d). Strikingly, the microtubules observed in the presence of PX-cit-Au48 appeared to have more protofilaments than normally observed under the conditions used *in vitro*. This may be explained by the larger diameter of PX-cit-Au48. At least one location of the paclitaxel binding site is thought to be in the microtubule lumen,[78,79] and therefore if PX-cit-Au48 were bound to the lumen of the microtubule during polymerization, it is conceivable that more protofilaments would have to assemble in order to form a closed cylindrical structure as the normal inner diameter of a microtubule is $\approx$ 17 nm (Figure 1.4). The fact that no microtubules were observed in the presence of cit-Au48 (Figure 5.2e) suggests that the formation of microtubules in the presence of PX-cit-Au48 (Figure 5.2d) is due to the presence of paclitaxel.

However, even though microtubules were observed in the presence of PX-cit-Au20 and PX-cit-Au48, no AuNPs were observed bound to these microtubules. Due to the much greater electron density of Au compared to the other atoms present in the sample (C, N, O, H), the AuNPs should show up as very dark spheres, as indicated in Figure 5.2e by a black arrow. Therefore, this suggests that either the paclitaxel has become detached from the AuNPs, or the PX-cit-AuNPs were displaced from the microtubules during the negative staining protocol performed prior to TEM imaging. Therefore, further testing must be done to better understand the mechanism of microtubule formation in the presence these nanoparticle samples.

PX-cit-Au48 May Bundle Microtubules

Another known cytotoxic effect of paclitaxel is its ability to promote the abnormal formation of microtubule bundles.[81,112] Accordingly, it was next tested if these paclitaxel-conjugated AuNPs induced the formation of microtubule bundles *in vitro*. To test this, HiLyte488-labeled microtubules were pre-polymerized and stabilized them with free paclitaxel. Then they were incubated with either (1) no additional

components; (2) PX-cit-Au10a; (3) PX-cit-Au10b; (4) PX-cit-Au20; (5) PX-cit-Au48; or (6) cit-Au48 at a 1:1 ratio in $MEM80_{6.8}$ with 10μM paclitaxel for 30 min at room temperature prior to visualization by TIRFM.

Figure 5.3 shows the results of experiments: microtubules in the presence of (a) no additional components; (b) PX-cit-Au10a; (c) PX-cit-Au10b; (d) PX-cit-Au20; (e) PX-cit-Au48; or (f) cit-Au48. No obvious bundling or differences between samples are observable by eye. The amount of bundling in each sample was quantified using a custom MALTLAB script by first measuring the fluorescence intensity profile at cross-sections of the microtubule at 5 px intervals. Each profile was fit with a Gaussian distribution and the area under the curve, corresponding to the total fluorescence intensity at that cross-section, was calculated. The fluorescent intensity per unit length of a single, unbundled microtubule was assumed to be within two standard deviations of the mean, as extracted from the Gaussian fit, of the population distribution of microtubules measured in the absence of dendrimers. This intensity range was assigned a weight of 1. Additional weights for bundled microtubules were assigned as multiples of this range (dimers: weight = 2, trimers: weight = 3, *etc.*). Using this weighting system, each measured microtubule length was accordingly weighted and summed to determine the total fraction of bundled microtubules in the sample (Figure 5.3g).

The plot in Figure 5.3g shows the fraction of total microtubule length bundled in each sample. The amount of microtubule bundling in the absence of nanoparticles seems high compared to previous bundling levels measured by TEM (see Chapter III). However, this is the first experiment performed with HiLyte488-tubulin, as opposed to all other experiments in this dissertation which were performed with TMR-labeled tubulin, therefore these elevated bundling levels may be due to an increased ability of HiLyte488 to induce bundling compared to TMR (see conclusions in Chapter IV). Since the chemical structure of HiLyte488 is proprietary, a structural comparison cannot be made with TMR.

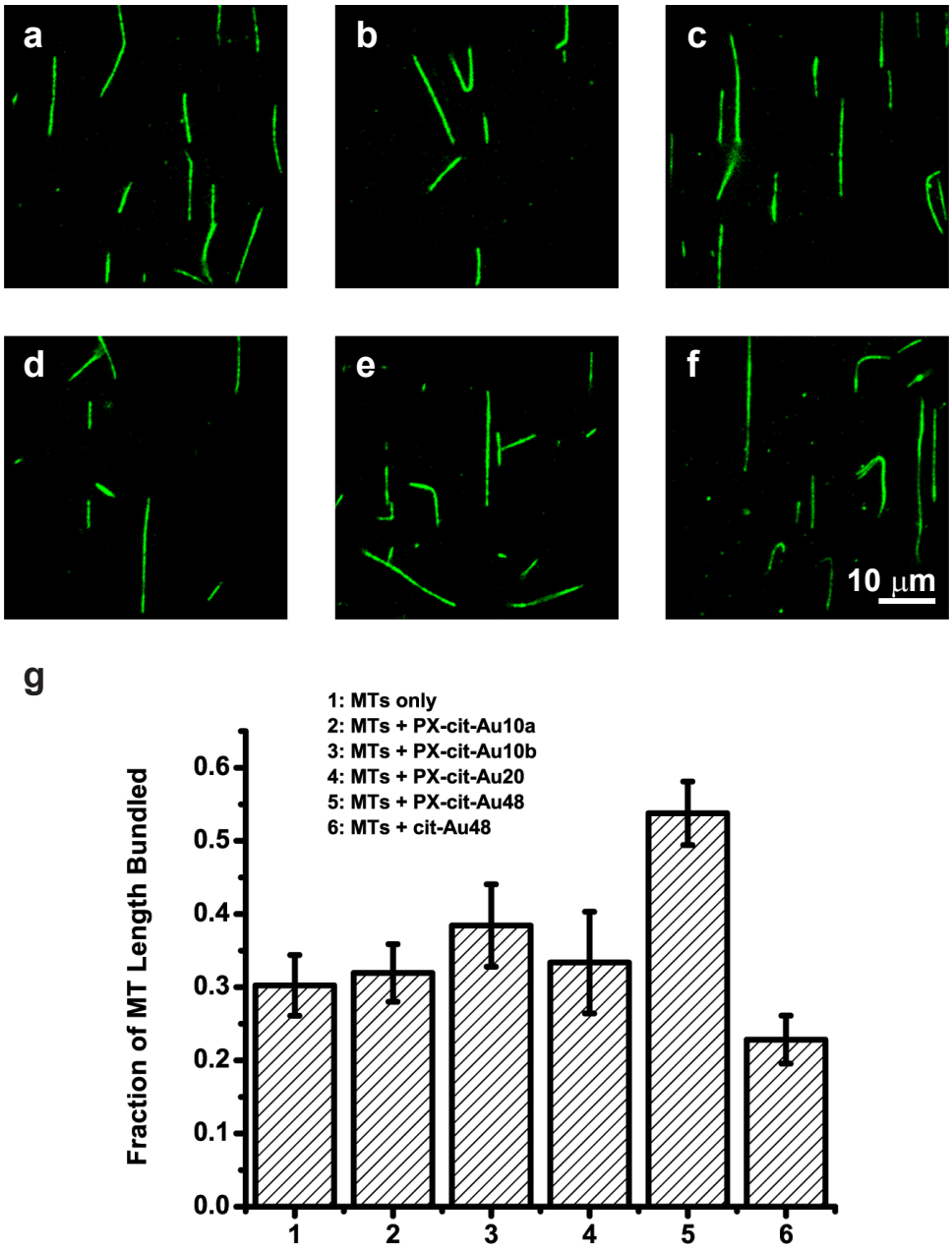

Figure 5.3: Microtubules (MTs) were incubated with either (a) no additional components; (b) PX-cit-Au10a; (c) PX-cit-Au10b; (d) PX-cit-Au20; (e) PX-cit-Au48; or (f) cit-Au48 at a 1:1 ratio in $MEM80_{6.8}$ with 10μM paclitaxel for 30 min at room temperature prior to visualization by TIRFM. Only the image from the TMR channel (green: microtubules) is shown. No obvious bundling can be seen by eye. (g) The amount of bundling in each sample was estimated from the cross-sectional fluorescent intensity profile of microtubules observed on $\geq$ (2 m)^2 of coverslip surface area, using a custom MATLAB script, and represented as the fraction of total microtubule length bundled.

Statistical significance between samples was tested using the Student's t-test with significance level $\alpha = 0.05$. This statistical test showed that there was no significant difference in bundling levels between any of the AuNPs compared to the free paclitaxel control, with two exceptions. PX-cit-Au48 was found to bundle microtubules significantly more than free paclitaxel, while cit-Au48 was found to bundle microtubules signficantly less than free paclitaxel ($p < 0.05$). The fact that the smaller AuNP conjugates do not seem capable of bundling microtubules implies that only PX-cit-Au48 supplies enough paclitaxel molecules per particle due to its large size to induce bundling. The decreased bundling levels measured in the presence of cit-Au48 are likely a result of the high anionic surface charge of the citrate, which is not shielded by conjugated paclitaxel on these nanoparticles. This high anionic surface charge would create electrostatic repulsion between particles, and possibly between the particles and the microtubule surface, blocking most, or all, cit-Au48 from binding microtubules.

Conclusions

In this study, preliminary evidence was presented showing that 20 nm and 48 nm paclitaxel-conjugated AuNPs were able to promote polymerization of microtubules *in vitro*, in the absence of GTP or MAPs. In addition, the 48 nm paclitaxel-conjugated AuNPs were found to promote abnormal microtubule bundling *in vitro*, but not any AuNP sample with a smaller diameter. This difference is likely explained by the ability of the 48 nm particles to carry higher numbers of paclitaxel particles compared to the smaller particles. Both of these cytotoxic activities could be attributed to the presence of paclitaxel, showing that the AuNP core is not cytotoxic with respect to alterations of microtubule dynamics or structure. However, AuNPs could not be seen by TEM bound to microtubules polymerized in the presence of paclitaxel-conjugate AuNPs, so it is not yet clear whether the paclitaxel bound the microtubules

while conjugated to the AuNPs or not. It should be noted that the ability of the conjugated paclitaxel to affect microtubule dynamics or structure is not absolutely required for these AuNPs to be effective drug delivery platforms, as they may release their paclitaxel load intracellulary. Therefore, *in vitro* testing with cultured cells is necessary to confirm the promise of these conjugates as drug delivery platforms.

CHAPTER VI

Summary and Future Directions

6.1 Summary

DNA-protein interactions are at the heart of many cellular functions in all organisms. A more in-depth understanding of these interactions would not only increase our understanding of these basic biological interactions, but better inform therapeutic design, and enable engineering applications such as the design of nanomotors capable of delivering cargo to a specific location in our genome.

In order to find a specific DNA-binding (target) site on the DNA, DNA-binding proteins employ a combination of: intradomain association and dissociation (3D diffusion or "hopping"), intersegment transfer (hopping between close DNA segments), sliding (1D diffusion), and site-specific recognition (Figure 1.1).[4,5] The question of how proteins slide along DNA is one that inspired this dissertation. It is thought that during sliding, proteins are "loosely" associated with DNA through electrostatic interactions.[14,15] This hypothesis is tested by creating a reductionist model in which the protein is modeled by a cationic particle and the DNA with an anionic "line". The model employed in this dissertation was a nanoparticle-microtubule system. The development and study of this model system led us to not only modify our hypothesis concerning protein sliding, but to characterize cytotoxic properties of nanoparticles, which are being increasingly incorporated into nanomedicines and other nanomateri-

als.[94–96]

Electrostatic Interactions are Not Sufficient for Protein Sliding

In Chapter II, nanoparticles of various materials and charge densities are tested for their interactions with microtubules using total internal reflection fluorescence microscopy (TIRFM) and single particle tracking methods. A previous observation in the literature that cationic polyacrylamide particles are able to slide along microtubules[25] inspired our choice to use microtubules as electrostatic DNA analogs. Like DNA, microtubules are "linear" biopolymers with an overall negative surface charge. In addition to electrosatic interactions, microtubules would provide opportunities for van der Waals interactions with the nanoparticles, but no specific DNA sequence information.

Neither the polyacrylamide particles (d = 38 or 80 nm; σ = 0.03 or 0.05 (+)/nm^2; Figure 2.1), nor the 2-dimethylaminoethanethiol (DMAET)-stabilized quantum dots (d = 4.3 nm; σ = 0.3 (+)/nm^2; Figure 2.6), that were tested showed any significant interactions with microtubules. These results are consistent with the findings of Minoura *et al.*[25] that the minimum charge density for polyacrylamide particles to significantly interact with microtubules is 3.3 (+)/nm^2. When generation 5 (G5) polyamidoamine (PAMAM) dendrimers carrying a surface charge density of 1.4 (+)/nm^2 were tested, it was found that these particles were able to bind microtubules, but not slide along them (Figure 2.7). The apparent discrepancy between this observation, and the observation of Minoura *et al.*[25] that particles with charge densities less than 3.3 (+)/nm^2 do not significantly interact with microtubules, is likely resolved through concentration differences (1.67 μM for dendrimers vs. pM range for polyacrylamide particles).

The only particles that were observed to slide along microtubules were aggregated polystyrene particles (Figure 2.3), which actually diffused along the microtubule in

two-dimensions rather than one. That is, the particles seemed to move laterally across the microtubule surface, rather than just longitudinally. In contrast, individual polystyrene particles, which were 53 nm in diameter with a surface charge density of 0.13 (+)/nm^2, were not observed to slide along microtubules. The diameter of one sliding aggregate was estimated by measurement from the image, and the Stokes-Einstein equation (using its measured diffusion coefficient), to be 1 μm. No estimate of the surface charge density of these aggregates could be obtained due to the probable high distribution of aggregate sizes present in the sample.

These results suggest that in order for spherical nanoparticles to slide along microtubules, and presumably by extension, DNA, they must have very high cationic charge densities, perhaps greater than 3.3 (+)/nm^2. There is an apparent discrepancy between these *in vitro* observations and the biological protein-DNA system: DNA-binding proteins do not have surface charge densities this high. For example, T7 RNA polymerase has a cationic charge density of 0.057 (+)/nm^2. However, the cationic charges of DNA-binding proteins are primarily concentrated in their DNA-binding domains, likely resulting in higher local cationic charge densities. Therefore, it may be that the shape complementarity of the protein to the DNA, and the charge juxtaposition within the protein's DNA binding pocket, are crucial for protein sliding,[14,45,46] and that electrostatic interactions alone are not sufficient. Indeed, it is possible that the reason that some of the polystyrene particle aggregates were able to slide along microtubules when most other aggregates and all individual nanoparticles were not, is that the presumably rough surface of these aggregates may have become, by chance, complementary in shape to the microtubules.

Paclitaxel-Conjugated PAMAM Dendrimers Adversely Affect Microtubule Structure through Two Independent Modes of Action

In addition to observing non-specific, electrostatically-driven diffusion along microtubules by nanoparticles, a target site analog was incorporated into our model system. For this purpose, paclitaxel was chosen to target the nanoparticles to microtubules. Paclitaxel is known to bind microtubules and stabilize them against depolymerization, an action that is cytotoxic *in vivo*. Naturally, due to this known cytotoxic behavior of paclitaxel, it is of interest to test the cytotoxicity of our paclitaxel-conjugated nanoparticles, which is the subject of Chapter III of this dissertation.

In Chapter III, the interactions between paclitaxel-conjugated G5 PAMAM dendrimers (Figure 3.1) and microtubules are investigated *in vitro*, primarily using two single microtubule imaging techniques: TIRFM and transmission electron microscopy (TEM). As paclitaxel is known to promote microtubule polymerization, stabilize microtubules,[104] and bundle microtubules,[81,112] the paclitaxel-conjugated dendrimers were tested for the retention of each of these cytotoxic properties. First, we find that paclitaxel-conjugated dendrimers are able to promote microtubule polymerization, although not as efficiently as unconjugated paclitaxel (Figures 3.2 and 3.3), implying that conjugation of paclitaxel to the dendrimer partially hinders its interaction with microtubules. Next, it is found that the conjugates are able to stabilize microtubules, although once again, not as efficiently as unconjugated paclitaxel (Figures 3.3 and 3.4). Finally, it is found that the conjugates are able to bundle microtubules (Figure 3.5), although this bundling is not due to the presence of paclitaxel on the conjugates. This dendrimer-induced bundling was instead dependent on pH (Figure 3.7). This pH dependence is interpreted to mean that the large number of protonatable tertiary amines in the dendrimer core (Figure 3.1) were mediating the observed bundling through electrostatic interactions with the microtubules surface.

The implications of these results are two-fold. First, paclitaxel-conjugated nanopar-

ticles may be suitable as drug delivery platforms. Even if the paclitaxel-nanoparticle linker is not cleaved on all particles (assuming they make it into the cell), these particles will still be able to act upon microtubules and induce cell death. Development of a water-soluble, targeted delivery strategy for paclitaxel is very desirable due to the detrimental side effects caused by this hydrophobic untargeted drug, which is an otherwise successful anti-tumor agent.[30] Second, the cytotoxicity of G5 PAMAM dendrimers warrants further investigation, especially since these nanoparticle have been of great interest to the field of targeted drug delivery.[32,48–51] Chapters IV and V follow up on these results, investigating the utility of paclitaxel-conjugated gold nanoparticles for targeted drug delivery, and the cytotoxicity of G5 PAMAM dendrimers, respectively.

The Fluorescent Dyes Cy5 and TMR Aid Microtubule Bundling Through Hydrophobic Interactions

In Chapter IV, the cytotoxicity of G5 PAMAM dendrimers is investigated in order to more precisely determine the cause of the dendrimer-induced microtubule bundling observed in Chapter III. In doing so, it was determined that in addition to electrostatic interactions, the observed dendrimer-induced microtubule bundling was also enhanced by hydrophobic interactions between the fluorescent dyes on the dendrimers (Cy5) and tubulin (TMR) used for TIRFM imaging (Figures 4.3 and 4.4 and 4.1). These results demonstrate that caution should be used when considering these, and other hydrophobic compounds, for imaging or therapeutic nanomedicines. However, it is possible that these dyes may still be safe for use in nanomedical applications in lower concentrations.

Paclitaxel-Conjugated Gold Nanoparticles Show Promise as a Targeted Cancer Drug Delivery Strategy

Gold nanoparticles (AuNPs) have a unique set of physical, chemical, and photonic properties among nanoparticles that makes them attractive for use in targeted drug delivery applications.[108,109] In addition, they provide multiple options for carrying and releasing drugs at the target site. For example, thiolated drugs can be conjugated to the AuNP surface *via* Au-S bonds. Upon cellular internalization, the reductive peptide GSH, which is present in high concentrations inside the cell, exchanges with the drug, thereby freeing the drug for therapeutic action. Since the intracellular concentrations of GSH are much higher than the extracellular, the selective release of the drug inside the cell rather than outside is promoted.[111]

It is this conjugation and delivery strategy that was employed for paclitaxel-conjugated AuNPs (Figure 5.1). By the same logic used when testing the paclitaxel-conjugated G5 PAMAM dendrimers, it was decided to test the ability of our paclitaxel-conjugated AuNPs to promote microtubule polymerization, stabilize microtubules, and bundle microtubules. Again, TIRFM and TEM were used for these experiments. First, it is found that microtubules are able to polymerize in the absence of GTP when they are incubated with 20 or 48 nm paclitaxel-conjugated AuNPs (Figure 5.2). However, no AuNPs could be seen bound to these microtubules, so it is unknown if the conjugated paclitaxel became separated from the AuNPs, or if the paclitaxel-conjugated AuNPs were replaced during staining prior to TEM imaging. Next, it is found that 48 nm paclitaxel-conjugated AuNPs were able to bundle microtubules, while three other distinct paclitaxel-conjugated AuNP samples with diameters $\leq$ 20 nm were not. In contrast to the dendrimer-mediated bundling observed in Chapter III, this bundling was dependent on the presence of paclitaxel. Together the results of this section demonstrate the promise of paclitaxel-conjugated AuNPs as targeted cancer drug delivery strategies.

6.2 Future Directions

The nanoparticle-microtubule model system developed in Chapter II is only a small step toward the overall goal of understanding the mechanisms of protein sliding along DNA. The results of this chapter suggest that electrostatic interactions alone are not sufficient to allow proteins to slide along DNA. Considering these results, it is proposed that specific protein conformational complementarity and a suitable arrangement of cationic charges in the protein's DNA binding pocket allow proteins to slide along DNA. Accordingly, future attempts to model protein sliding using cationic nanoparticles should utilize concave nanoparticles with cationic charges concentrated in their concavities in order to more closely mimic the conformation and charge arrangements of DNA-binding proteins. For example, Zhao *et al.*[113] and Berkovitch *et al.*[114] have already synthesized two different types of concave inorganic nanoparticles. However, synthesizing concave nanoparticles on the size scale of DNA-binding proteins, and preferentially placing cationic charges in the concavity, is still a technological challenge.

The results of Chapters III and V concerning paclitaxel-conjugated nanoparticles warrant further investigation into the suitability of these and similar particles as drug delivery platforms. The experiments presented in this dissertation were all performed *in vitro* with purified tubulin. In order to determine the utility of the particles, they must also be conjugated with some tumor targeting molecule (see Majoros *et al.*,[53] for example), and tested *in vivo* with cultured cell lines for cytotoxicity and intracellular release of their paclitaxel load.

Finally, the results of Chapter IV warrant further investigation into the concentration dependence of microtubule bundling induced by the hydrophobic fluorescent dyes Cy5 and TMR, on the dendrimer and microtubules, respectively. If these dyes are found to not induce microtubule bundling at dye:tubulin ratios that could be expected to be utilized nanomedical imaging applications, then these dyes—and by

extension, aromatic drug molecules—may still be safe for use in these applications □

APPENDICES

APPENDIX A

Synthesis and Characterization of Paclitaxel-Conjugated PAMAM Dendrimers

Synthesis and Characterization of the Paclitaxel Linker

The synthetic scheme of the paclitaxel linker is shown in Figure A.1.

Step 1. To a solution of cystamine dihydrochloride (**1**; 5.00 g, 22.2 mmol) in water (15 mL) was added NaOH (2.66 g, 66.6 mmol). The solution was diluted in MeOH (50 mL) and succinic anhydride was added (2.22 g, 22.2 mmol). The reaction was stirred at 0 °C for 1 h, then room temperature for 7 h. Boc anhydride ($(Boc)_2O$; 7.30 g, 33.3 mmol) was added to the mixture and the resulting mixture was stirred at room temperature for 12 h. The mixture was concentrated *in vacuo*, and the aqueous residue was diluted with water (50 mL), basified with $NaHCO_3$ (5 %) to pH $\approx$ 9, extracted with ethyl acetate (150 mL), acidified with 1 M H_3PO_4 to pH $\approx$ 5, and extracted again with ethyl acetate (300 mL). The organic layer was concentrated *in vacuo* and purified by flash silica column chromatography (15:85 MeOH:CH_2Cl_2) to yield the N-Boc protected cystamine-succinic acid (**2**) as a white solid (1.64 g, 21 %).

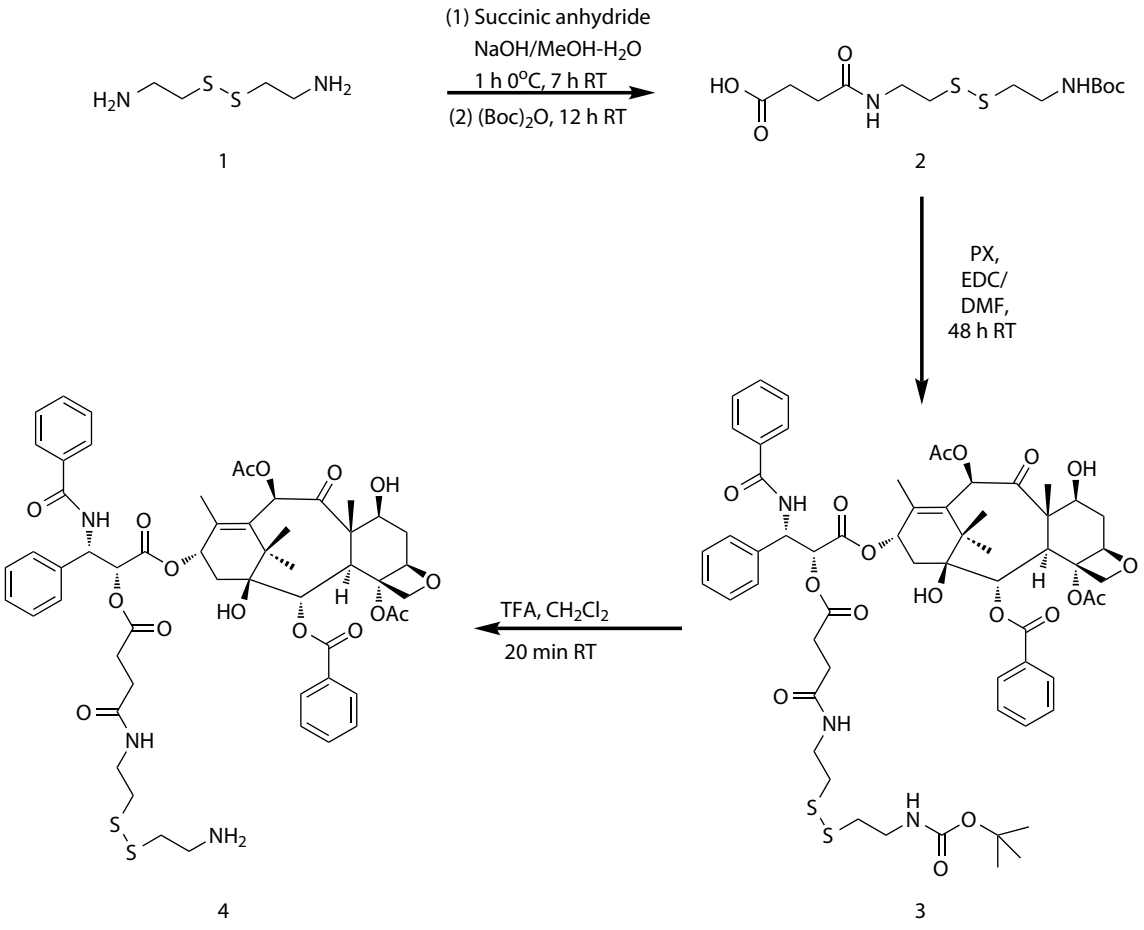

Figure A.1: Synthesis of the paclitaxel linker

R_f (5 % MeOH:CH_2Cl_2) = 0.29. ^{1}H NMR (400 MHz, $CDCl_3$): δ 3.46-3.44 (t, 2H), 3.33-3.3 (br m, 2H), 2.75-2.74 (t, 2H), 2.72 (t, 2H), 2.69 (t, 2H), 2.43 (br t, 2H), 1.36 (s, 9H) ppm.

Step 2. To a solution of paclitaxel (200 mg, 0.234 mmol) and the N-Boc protected cystamine-succinic acid (**2**; 87 mg, 0.246 mmol) in dimethylformamide (DMF; 10 mL) were added 4-dimethylaminopyridine (DMAP; 31 mg, 0.236 mmol) and 1-ethyl-3-(3-dimethylaminopropyl) carbodiimide hydrochloride (EDC; 31 mg, 0.254 mmol). The mixture was stirred at room temperature for 48 h. The mixture was concentrated *in vacuo* and then purified by flash silica column chromatography by eluting with 5-10 % MeOH/CH_2Cl_2 to yield the N-Boc protected paclitaxel linker derivative (**3**) as a pale yellow foam (209 mg, 75 %). R_f (5 % MeOH:CH_2Cl_2) = 0.46. ^{1}H NMR (400 MHz, CD_3OD): δ 8.08-8.05 (m), 7.93 (s), 7.82-7.76 (m), 7.66-7.61 (m), 7.58-7.48 (m), 7.44-7.35 (m), 7.26-7.20 (m), 6.8 (d), 6.41 (s), 6.11 (br t), 6.03 (m), 5.79-5.75 (m), 5.60 (m), 5.42-5.40 (t), 4.97 (d), 4.70 (d), 4.55 (br s), 4.36-4.22 (m), 4.14 (s), 3.79-3.71 (m), 3.41-3.38 (m), 3.31-3.26 (m), 3.12 (br m), 2.99-2.83 (m), 2.80 (s), 2.77-2.51 (m), 2.45-2.41 (m), 2.36-2.32 (m), 2.19-2.10 (m), 1.88 (d), 1.80-1.70 (m), 1.61 (s), 1.4 (br s), 1.10 (m) ppm. MS (ESI, positive ion mode): m/z (relative intensity, %) = 1210.4 (100) $[M+Na]^+$. HRMS (ESI) calculated for $C_{60}H_{73}N_3O_{18}S_2Na$ 1210.4228, found 1210.4271.

Step 3. To the N-Boc protected paclitaxel derivative (**3**; 50 mg, 0.042 mmol) was added a mixture of trifluoroacetic acid and CH_2Cl_2 (2 mL; 1:1). The mixture was stirred at room temperature for 20 min and then evaporated to dryness to yield the paclitaxel linker (**4**) as pale yellow oil. The ^{1}H NMR analysis indicated the complete deprotection of the N-Boc protecting group, and the product was used without further treatment in the next step. R_f (0.5 % Et_3N/5 % MeOH:CH_2Cl_2) = 0.56. ^{1}H NMR (400 MHz, CD_3OD): δ 8.08-8.05 (m), 7.98-7.93 (m), 7.82-7.76 (m), 7.66-7.61 (m),

7.58-7.48 (m), 7.44-7.35 (m), 7.26-7.20 (m), 6.8 (d), 6.52 (d), 6.41 (s), 6.21 (br d) 6.11 (br t), 6.03 (m), 5.79-5.75 (m), 5.73-5.60 (m), 5.47-5.45 (m), 5.42-5.40(t), 5.29-5.24 (m), 4.97 (d), 4.70 (d), 4.6 (br s), 4.36-4.22 (m), 4.14 (s), 4.10-4.03 (m), 3.79-3.71 (m), 3.59-3.51 (m), 3.41-3.38 (m), 3.31-3.23(m), 3.12 (br m), 2.99-2.83 (m), 2.80 (s), 2.77-2.51 (m), 2.45-2.41 (m), 2.36-2.32 (m), 2.19-2.10 (m), 1.98 (d), 1.92-1.87 (m), 1.80-1.70 (m), 1.61 (s), 1.59-1.53 (m), 1.33 (br s), 1.10 (m), 1.01-0.94 (m), 0.89-0.83 (m) ppm. MS (ESI, positive ion mode): *m/z* (relative intensity, %) = 1088.4 (100) $[M+H]^+$. HRMS (ESI) calculated for $C_{55}H_{66}N_3O_6S_2$ 1088.3885, found 1088.3912.

Synthesis and Characterization of $PX_3Cy_{2-3}OH_{108}$-G5

The synthetic scheme of the $PX_3Cy_{2-3}OH_{108}$-G5 synthesis is shown in Figure A.2.

To a solution of G5 PAMAM dendrimers ($(NH_2)_{114}$-G5; **5**; 100 mg; 3.7 μmol) in MeOH (10 mL) was added Cy5-NHS ester (14.2 mg; 18 μmol) and the mixture was stirred at room temperature for 16 h. To the resulting conjugate, $Cy_{2-3}(NH_2)_{108}$-G5 (**6**), was added glutaric anhydride (74 mg; 740 μmol) and the mixture was stirred at room temperature for 24 h. The mixture was then purified by MWCO 10 kD ultrafiltration to yield the carboxylated conjugate $Cy_{2-3}(COOH)_{108}$-G5 (**7**) as a sticky blue solid (83 mg; 47 %). To the carboxylated conjugate (**7**; 50 mg; 1.22 μmol) were added 1-ethyl-3-(3-dimethylaminopropyl) carbodiimide hydrochloride (EDC; 954 mg; 183 μmol) and NHS (23 mg; 200 μmol) in DMF (20 mL) and the mixture was stirred at room temperature for 8 h. To the resulting conjugate (**8**) was added the paclitaxel linker (**4**; 13.3 mg; 12.2 μmol) in triethylamine (TEA; 5 μL) and the mixture was stirred at room temperature for 12 h. To this mixture was added ethanolamine (ETA; 5 μL) and the mixture was stirred at room temperature for 16 h in order to quench the active NHS ester and neutralize the dendrimer surface. The resulting mixture was first purified by 10 kD dialysis against PBS and DI water for 3 runs each and then lyophilized

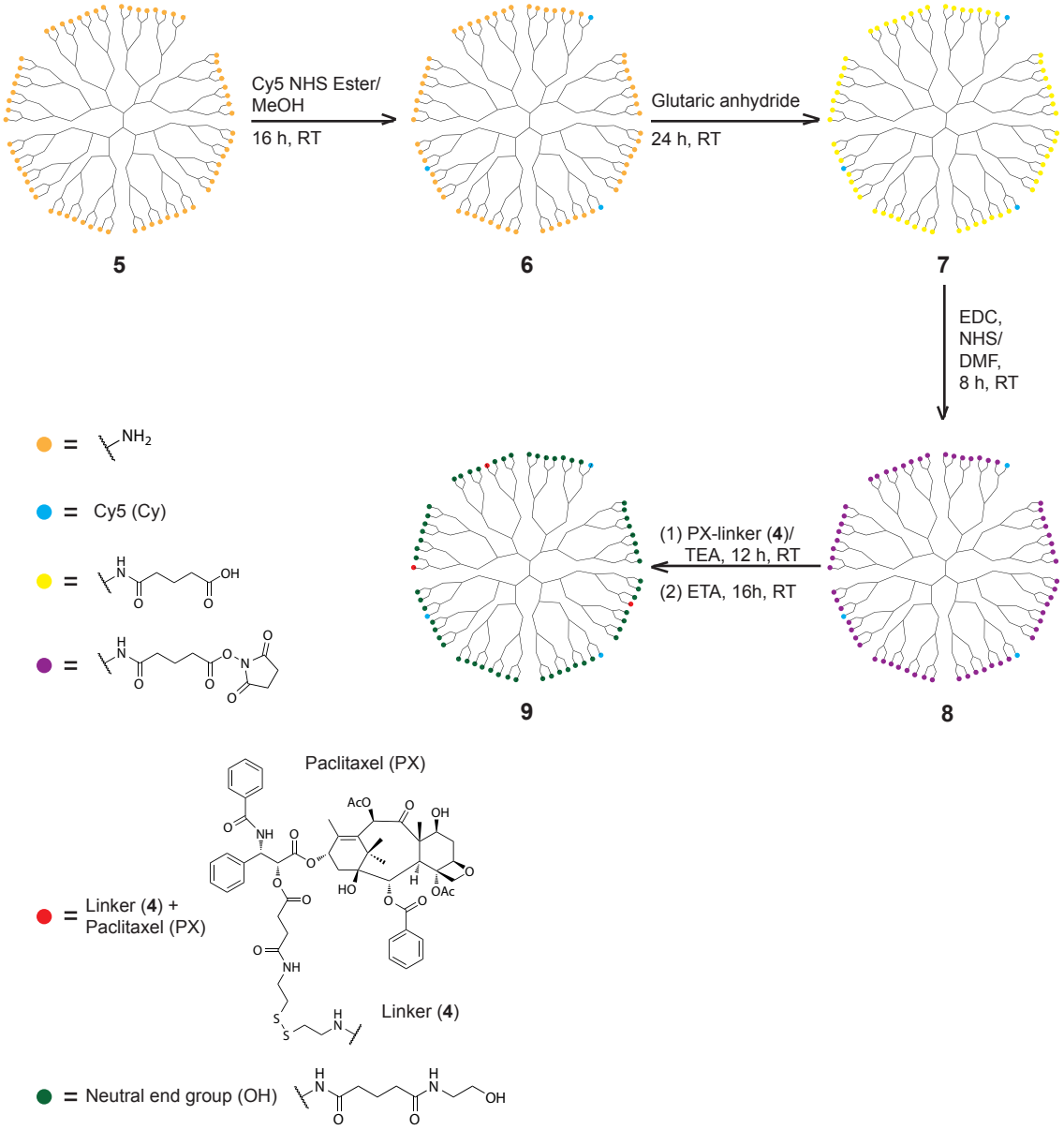

Figure A.2: Synthesis of $PX_3Cy_{2-3}OH_{108}$-G5

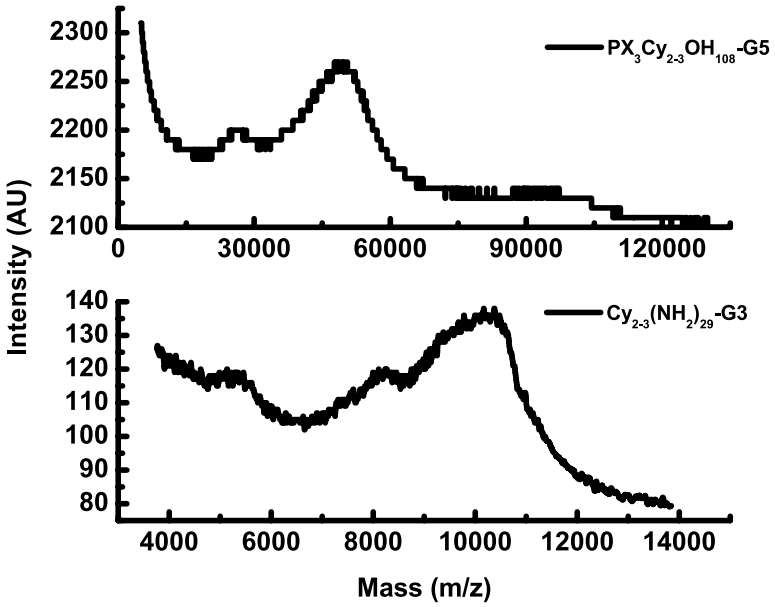

Figure A.3: MALDI-TOF mass spectra of $PX_3Cy_{2-3}OH_{108}$-G5 (top panel) and $PX_3Cy_{2-3}OH_{26}$-G3 (bottom panel).

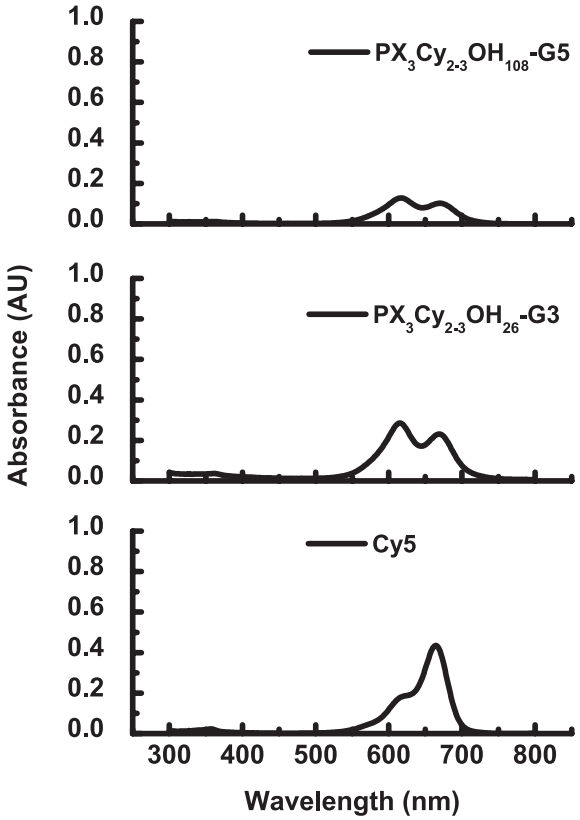

Figure A.4: Ultraviolet-visible spectra of $PX_3Cy_{2-3}OH_{108}$-G5 (top panel), $PX_3Cy_{2-3}OH_{26}$-G3 (middle panel), and Cy5 (bottom panel).

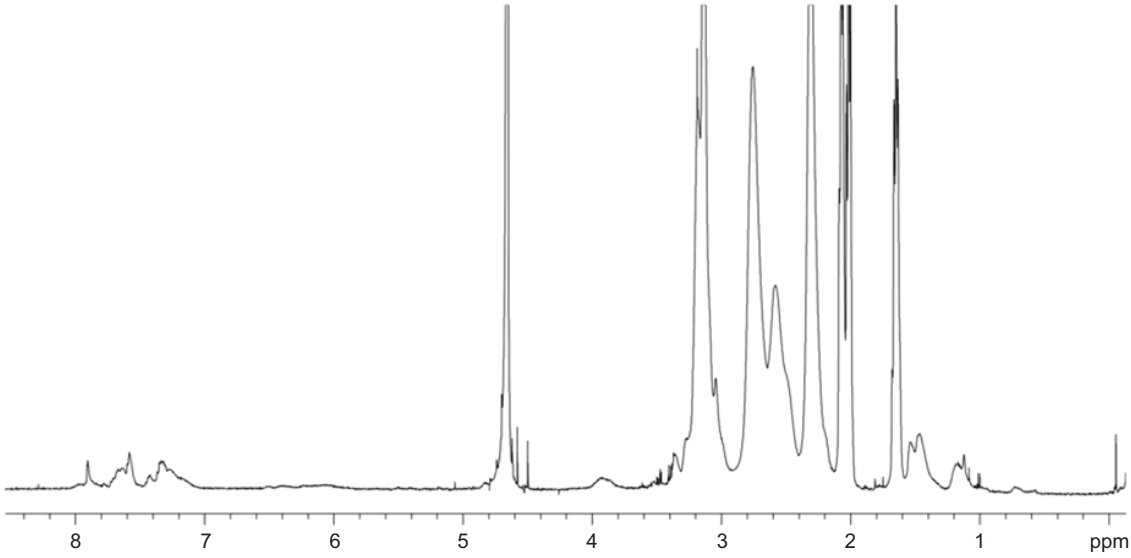

Figure A.5: ^{1}H NMR spectrum of $PX_3Cy_{2-3}OH_{108}$-G5

to yield $PX_3Cy_{2-3}OH_{108}$-G5 (**9**) as a blue solid (48 mg; 82.0 %). MALDI-TOF-MASS analysis indicated that the $PX_3Cy_{2-3}OH_{108}$-G5 was the expected molecular weight, 48 kDa (Figure A.3). The number of conjugated Cy5 dyes per dendrimer was determined to be 2.3, on average, using ultraviolet-visible spectroscopy (Figure A.4), calibrated to free Cy5. The number of conjugated paclitaxel molecules per dendrimer was determined to be 3.2 using ^{1}H NMR spectroscopy (Figure A.5). This was determined as follows. The peaks at δ (ppm) $\approx$ 7-8 belong to the combination of three phenyl groups (15 H's) of paclitaxel and the aromatic groups (8 H's) of Cy5. The integration value for these combined signals was corrected to represent only paclitaxel by subtracting out the integration value calculated for the contribution of Cy5 molecule. For this correction, other signals at δ (ppm) $\approx$ 6–6.6, belonging to the protons in the triene conjugation system of Cy5 (3 H's), were used as a reference, and it was assumed that the mean number of Cy5 molecules per dendrimer is 2.3, as determined earlier by ultraviolet-visible spectroscopy (Figure A.4).

Testing the Stability of Paclitaxel Conjugation to PX_3Cy_{2-3}-OH_{108}-G5

$PX_3Cy_{2-3}OH_{108}$-G5 was tested for stability in water to confirm that the paclitaxel would not be spontaneously hydrolyzed from the dendrimer carrier at room temperature in the aqueous buffers used in this study over the maximum experimental time frame, $\leq$ 6 h. In order to test this, $PX_3Cy_{2-3}OH_{108}$-G5 was dissolved in DI water to a final concentration of 1 mg/mL. A 200 μL aliquot of this aqueous solution was tested for the presence of free paclitaxel after 0.17, 1, 2, 3, 6, and 20 h at room temperature. First, the dendrimers were removed from each aliquot by MWCO 10 kD ultrafiltration. Then the filtrate, containing any free paclitaxel that may have separated from the dendrimer during the incubation in water, was collected and the concentration of

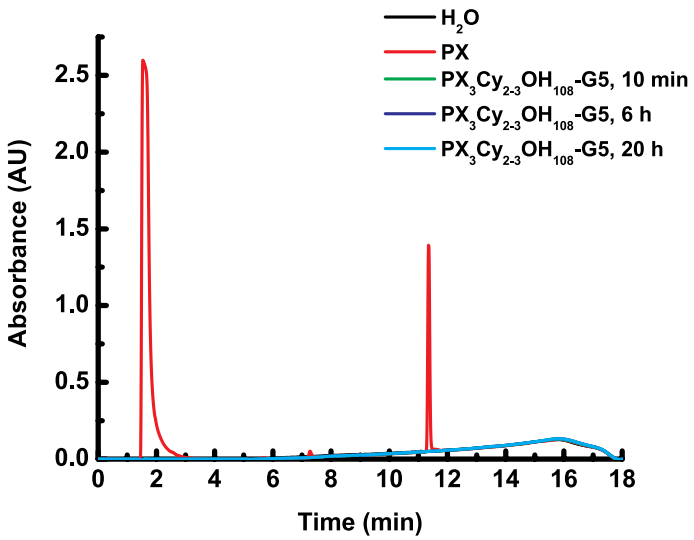

Figure A.6: UPLC spectra of DI H_2O (black); (b) paclitaxel (PX) in DI water (red); or MWCO 10 kD filtrates from $PX_3Cy_{2-3}OH_{108}$-G5 incubated in DI water at room temperature for 10 min (green); 6 h (dark blue); or 20 h (light blue). Note that the first elution peak of the "PX" sample represents the solvent front while the second peak represents PX. All signals from the $PX_3Cy_{2-3}OH_{108}$-G5 filtrates are identical to that of water, and show no significant elution peaks at the time points that free PX elutes, indicating that the PX linker of $PX_3Cy_{2-3}OH_{108}$-G5 is stable in water at room temperature for up to 20 h.

free paclitaxel was measured by ultra performance liquid chromatography (UPLC), using an Acquity Peptide Mapping System (Waters Corporation; Milford, MA) controlled by Empower 2 software and equipped with an Acquity BEH C4 column and a photodiode array detector. A gradient elution was used, using a mobile phase ranging from 99:1 - 20:80 (v/v) water:acetonitrile, containing 0.14 % trifluoroacetic acid. The UPLC spectra show that the paclitaxel linker of $PX_3Cy_{2-3}OH_{108}$-G5 is stable in water at room temperature for up to 20 h (Figure A.6).

Measuring the pKa of Tertiary Amines in the G5 PAMAM Dendrimer Core

For this measurement, a G5 PAMAM dendrimer with the same neutralizing surface modification as $PX_3Cy_{2-3}OH_{108}$-G5 (*i.e.* its terminal groups are hydroxyl groups), but with no conjugated Cy5 or paclitaxel, was used. This dendrimer, termed OH_{114}-G5, according to its surface modifications and stoichiometry, only contains titratable protons sites in the tertiary amines in the dendrimer core (compare with the structure of $PX_3Cy_{2-3}OH_{108}$-G5 shown in Figure 1). Potentiometric titration of OH_{114}-G5 was compared with that of $(NH_2)_{114}$-G5 (Figure A.7). Prior to titration, 10 mg of dendrimer was dissolved in 1 mL of 0.1 N NaCl and the pH of the resulting solution was adjusted to 2.5. Potentiometric titration was conducted manually with a MP230 pH meter equipped with an InLab®Micro pH electrode (Mettler-Toledo; Columbus, OH). Assuming that both dendrimers have an equivalent titration start point, the pKa of the tertiary amines in OH_{114}-G5 was calculated as follows: pKa = 0.5 (Endpoint + Startpoint) = 0.5 (9.484 + 3.455) = 6.5 $\pm$ 0.2, where the error was determined from the raw data.

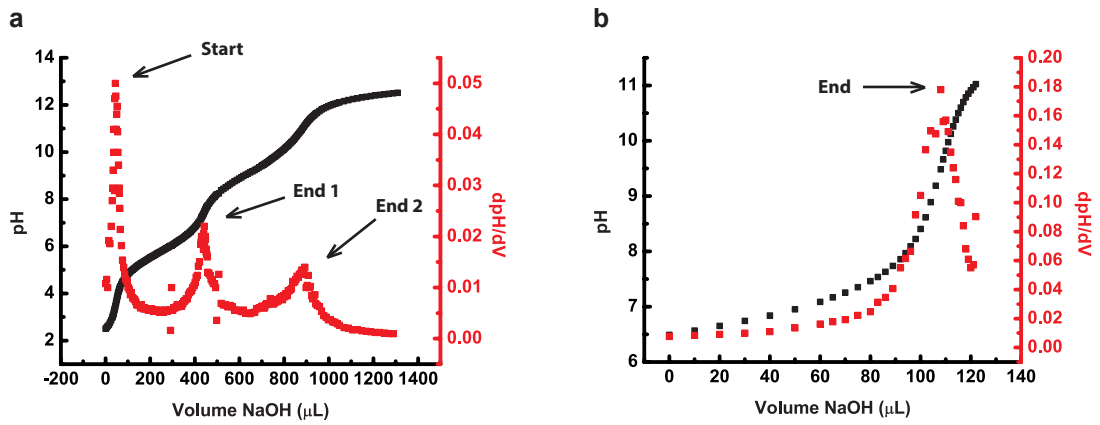

Figure A.7: Potentiometric titration curves of (a) $(NH_2)_{114}$-G5, showing the start point of titration (start), endpoint of the tertiary amine titration (end 1) and endpoint of the primary amine titration (end 2); and (b) OH_{114}-G5, showing the endpoint of the tertiary amine titration (end).

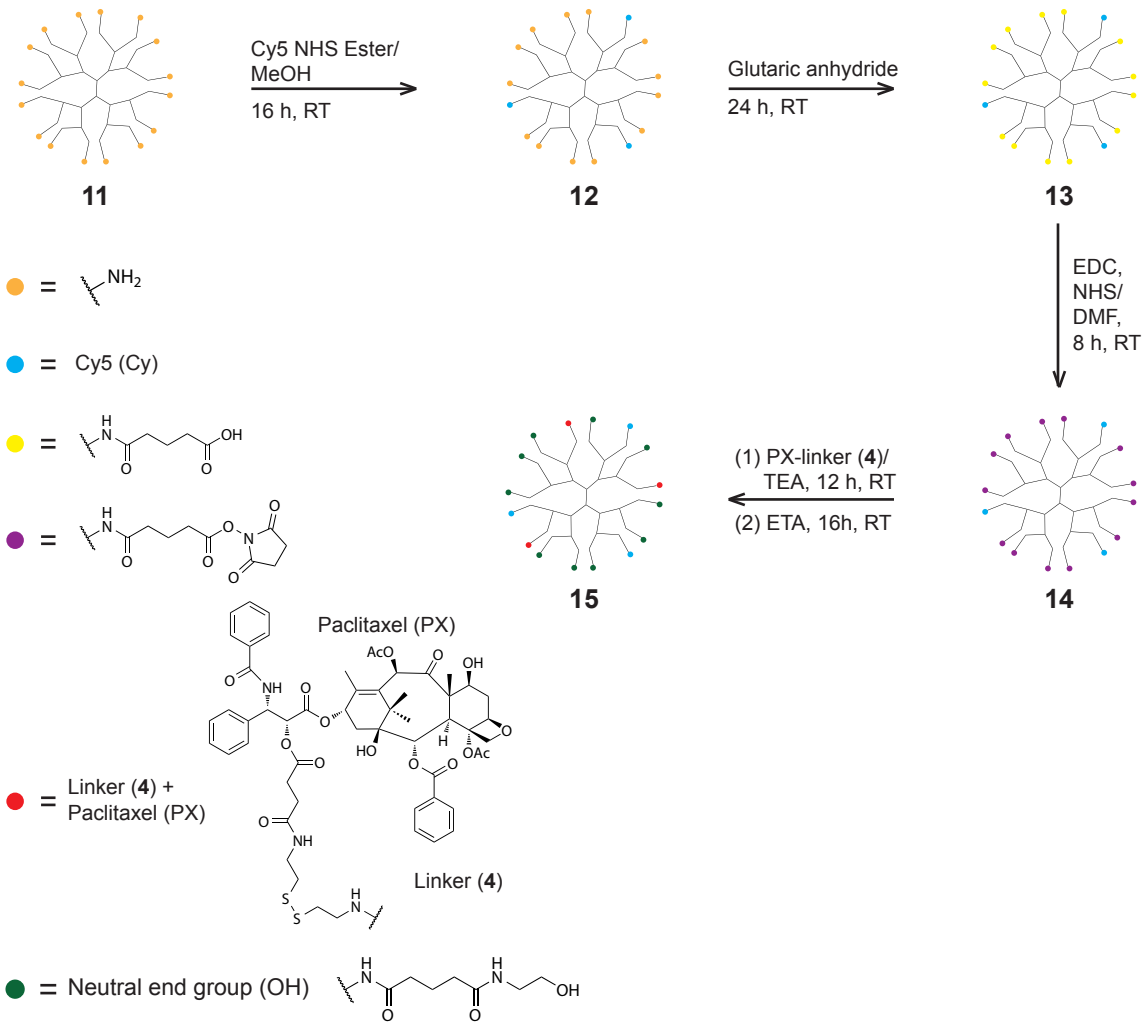

Figure A.8: Synthesis of $PX_3Cy_{2-3}OH_{26}$-G3

Synthesis and Characterization of $PX_3Cy_{2-3}OH_{26}$-G3

The synthetic scheme of $PX_3Cy_{2-3}OH_{26}$-G3 is shown in Figure A.8.

G3 PAMAM dendrimers were first purified using a 1 kDa MWCO dialysis membrane, achieving a relatively monodisperse population (polydispersity index (PDI) = 1.01–1.05, determined by gel permeation chromatography (GPC)).

To a solution of G3 PAMAM dendrimers ($(NH_2)_{32}$-G3; **11**; 20 mg; 2.87 μmol) in MeOH (5 mL) was added Cy5-NHS ester (11.3 mg; 14.2 μmol) and the mixture was stirred at room temperature for 16 h. To the resulting conjugate, $Cy_{2-3}(NH_2)_{29}$-G3 (**12**), was added gluataric anhydride (14.35 mg; 143.5 μmol) and the mixture was stirred at room temperature for 24 h. The mixture was then purified by MWCO 3 kD ultrafiltration to yield the carboxylated conjugate $Cy_{2-3}(COOH)_{29}$-G3 (**13**) as a sticky blue solid (16.3 mg; 54.7 %). To the carboxylated conjugate (**13**; 12.4 mg; 1.2 μmol) were added EDC and NHS (6.9 mg; 60 μmol) in DMF (5 mL) and the mixture was stirred at room temperature for 8 h. To the resulting conjugate (**14**) was added the paclitaxel linker (**4**; 10.9 mg; 10 μmol) in TEA (3 μL) and the mixture was stirred at room temperature for 12 h. To this mixture was added ETA (5 μL) and the mixture was stirred at room temperature for 16 h in order to quench the active NHS ester and neutralize the dendrimer surface. The resulting mixture was first purified by MWCO 3 kD dialysis against PBS and DI water for 3 runs each and then lyophilized to yield $PX_3Cy_{2-3}OH_{26}$-G3 (**15**) as a blue solid (12.3 mg 42 %). MALDI-TOF-MASS analysis indicated that the $Cy_{2-3}(NH_2)_{29}$-G3 was the expected molecular weight, 10.4 kDa (Figure A.3). The number of conjugated Cy5 dyes per $PX_3Cy_{2-3}OH_{26}$-G3 was determined to be 2-3, on average, using ultraviolet-visible spectroscopy (Figure A.4), calibrated to free Cy5. The number of conjugated paclitaxel molecules per $PX_3Cy_{2-3}OH_{26}$-G3 was determined to be 3.2 using ^{1}H NMR spectroscopy (Figure A.9); by integrating the aromatic peaks located at δ 7-8 and

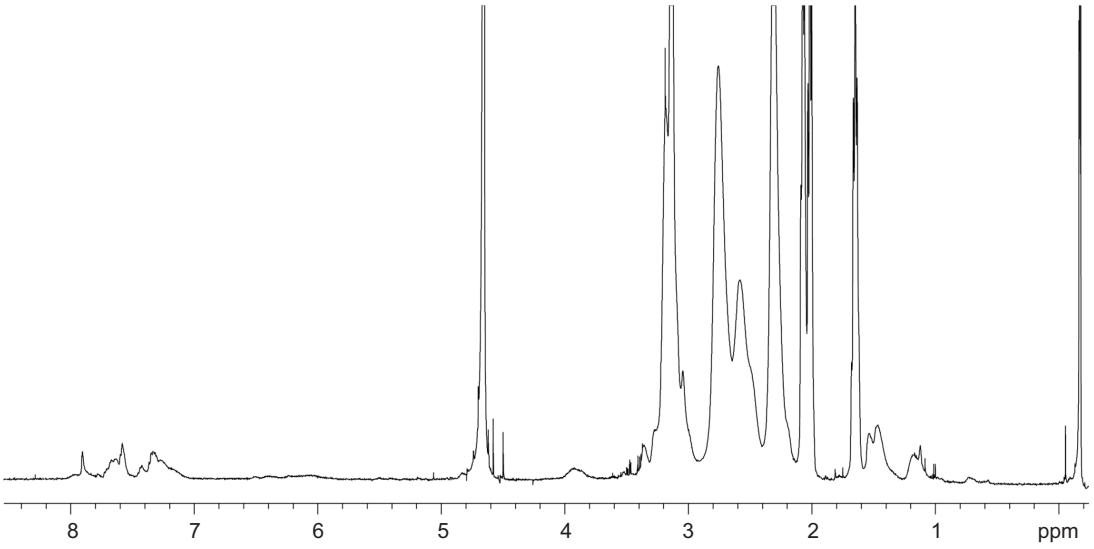

Figure A.9: ^{1}H NMR spectrum of $PX_3Cy_{2-3}OH_{26}$-G3

subtracting out the aromatic protons due to the number of conjugated Cy5 molecules per dendrimer determined by ultraviolet-visible spectroscopy.

APPENDIX B

Using DNA Curtains to Study DNA-Protein Interactions

Introduction[1]

In order to visualize single proteins—or nanoparticles—sliding along DNA in order to gain information about their dimensionality and speed of movement along DNA—among other information—single molecule microscopy techniques must be used. As shown in Chapter II of this dissertation, total internal reflection fluorescence microscopy (TIRFM) is one technique well suited for this application. In addition to imaging nanoparticles sliding along DNA as done in this dissertation, TIRFM has also been used to image proteins sliding along DNA.[8,10,12] Previously, in order to achieve these observations, DNA was randomly adhered to the slide (or coverslip) surface and stretched and aligned either by flow[8,12] or molecular combing.[10] While nonetheless effective, these DNA adherence techniques have a few drawbacks. First,

[1]Training in DNA curtain technology kindly provided by Eric Greene's laboratory, primarily by Feng Wang and Jayil Lee. λ DNA containing a T7 RNA polymerase promoter and biotinylated T7 RNA polymerase constructs were prepared by Feng Wang. All nanofabrication for this project was performed by Ashwin Panday. This project was conducted in collaboration with Soma Dhakal.

because the DNA is anchored directly to the surface, either at the end(s) or at interior points, the normal helical movement of DNA-binding proteins around DNA[26–28] is hindered. Second, the placement and orientation of the DNA strands cannot be precisely controlled.

Recently, a technique has been developed by Eric Greene (Columbia University) for adhering DNA to surfaces for single molecule observations by TIRFM that addresses these drawbacks. This technique, termed DNA curtains, involves stringing DNA molecules across nanofabricated barriers resulting in hundreds of parallel DNA molecules oriented in the same direction can be viewed in a single field of view (Figure B.1).[115] This allows for hundreds of DNA-protein interactions to be observed in a single experiment. DNA curtains have been used by Eric Greene and colleagues to investigate interactions between DNA and multiple DNA-binding proteins.[7,116–118]

Generally, DNA curtains are formed by creating a fluid lipid bilayer on a slide surface containing nanofabricated barriers that are raised 25 nm from the surface, 20 nm above the $\approx$ 5 nm lipid bilayer. λ DNA molecules, labeled on one end with biotin and on the other end with digoxygenin (DIG), are tethered to the lipid bilayer through biotin-streptavidin-biotin linkages. Buffer flow pushes the tethered DNA to the corners of zig-zag nanofabricated barriers and stretches the DNA, allowing it to anchor to an opposite pentagonal barrier through DIG-anti-DIG linkages (Figure B.1). Suspending the DNA 20 nm above the lipid bilayer *via* nanofabricated barriers allows proteins to access 360 $^\circ$ of the DNA structure, allowing them to move in a helical path along the DNA. Furthermore, by differentially end-labeling the DNA, each DNA molecule is oriented in the same direction, allowing for directional observations if specific DNA sequences are engineered into the λ DNA template.

The motivation for using DNA curtains to address the main goal of this dissertation was to visualize nanoparticle-DNA or protein-DNA interactions during target site searching, whether natural or mimicked (in the case of nanoparticles). This technique

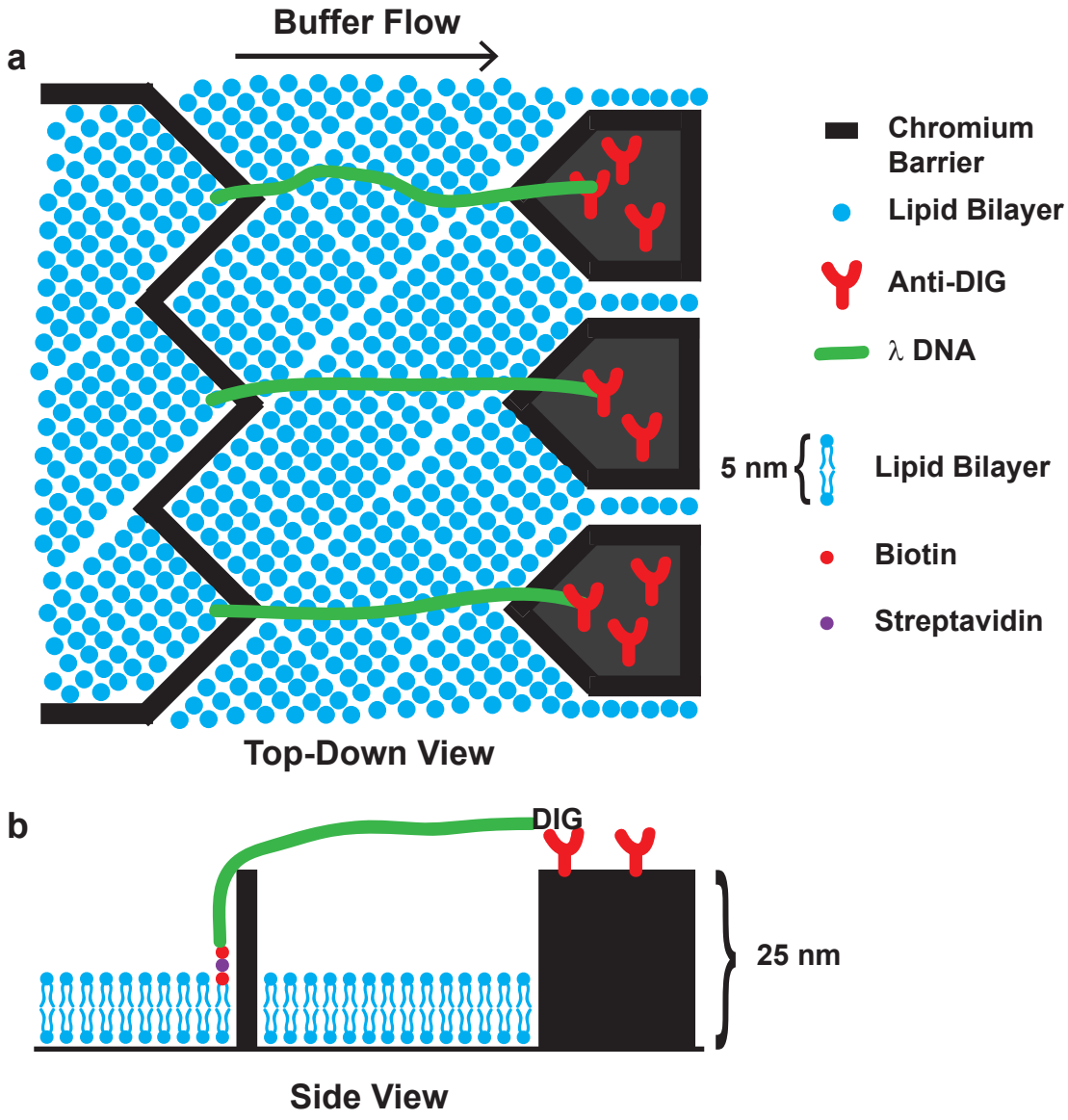

Figure B.1: (a) Top-down and (b) side views of double-tethered DNA curtain schematic. A fluid lipid bilayer is created on a slide surface containing nanofabricated barriers raised 25 nm from the surface, 20 nm above the $\approx$ 5 nm lipid bilayer. λ DNA molecules, labeled on one end with biotin and on the other end with digoxygenin (DIG), are tethered to the lipid bilayer through biotin-streptavidin-biotin linkages. Buffer flow pushes the tethered DNA to the corners of the zig-zag barriers and stretches it, allowing it to anchor to the opposite pentagonal barrier through DIG-anti-DIG linkages. Many copies of these patterns can be fabricated on a single slide allowing hundreds of observations per experiment.

should be very advantageous for studying both types of interactions. For example, my collaborator Shi Yu in Ron Larson's lab (University of Michigan) has found that cationic nanoparticles can significantly interact with DNA in solution, but not when the DNA is attached to the surface *via* molecular combing, presumably because the affinity of the nanoparticles for the DNA is not significantly greater than the affinity to the surface (data not published). DNA curtain technology significantly raises the DNA above the surface and employs a lipid bilayer to block protein—and presumably nanoparticle—binding to the surface.

The first aspect of target site searching that was of interest to characterize using DNA curtains was the ability of bacteriophage T7 RNA polymerase to locate and recognize promoters (target sites) with varying degrees of sequence mutation. DNA-binding proteins recognize the unique chemical signature and/or three-dimensional structure of their DNA target sites. Both of these properties are very sensitive to the exact sequence of the DNA target site and mutation of even one base can disrupt the ability of the protein to recognize its target.[18] To our knowledge, a characterization of the effect of promoter mutations on the kinetics of T7 RNA polymerase recognition using single molecule, real-time observations has never been reported.

The second aspect of target site searching that was of interest to characterize was the effect of varying DNA roughness landscapes on the sliding kinetics of T7 RNA polymerase. DNA is thought to have different "roughness" landscapes based on specific sequences. Theory predicts that RNA polymerase will speed up or slow down upon encountering sequences of different roughness.[3] Different degrees of roughness can be programmed into a DNA strand by changing its sequence using DNA cloning techniques. Using a model developed by my collaborator Shi Yu (Ron Larson's lab, University of Michigan), the diffusion coefficient of RNA polymerase along these different sequences can be predicted, the diffusion of RNA polymerase in real time along these sequences can be tracked, the experimental observations to the theoretical

predictions can be compared. To our knowledge, such a characterization has never been reported.

Materials and Methods

All protocols were modified from the Eric Greene's protocols.[115]

End-labeling Lambda DNA

4 nM of λ DNA (Invitrogen; Grand Island, NY), warmed to 65 °C for 10 min before pipetting with wide bore pipet tips (Mettler-Toledo; Chicago, IL), was incubated with a 3' biotinylated oligonucleotide complementary to the single stranded overhangs on λ DNA and a 5' DIG-labeled complementary oligonucleotide (both from Exiqon; Vedbæk, Denmark) in 1x T4 DNA ligase reaction buffer (New England Biolabs; Ipswich, MA) at 65 °C for 10 min. After the mixture was cooled to room temperature, 4 U/μL of T4 DNA ligase (New England Biolabs; Ipswich, MA) was added and the resulting mixture was incubated overnight at 42 °C. The next day, the ligase was heat inactivated at 65 °C for 10 min.

Next, the ligase was removed from the mixture by phenol-chloroform extraction. The sample was mixed with one half volume of buffer saturated phenol (MP Biochemicals; Santa Ana, CA) and one half volume chloroform (Sigma-Aldrich; St-Louis, MO) by upturning the sample vial several times. The mixture was then incubated at room temperature for 1 min prior to centrifugation for 1 min at top speed on a table-top Eppendorf (Hamburg, Germany) centrifuge. The aqueous (top) layer was transferred to a new tube and mixed with one volume chloroform by upturning the tube several times. The mixture was then incubated at room temperature for 1 min prior to centrifugation for 1 min at top speed on a table-top centrifuge. The aqueous (top) layer was again removed to a separate tube, and chloroform extraction was repeated twice more. The sample (final aqueous layer) was then concentrated in an Eppendorf

Vacufuge for 30 min. Finally, the labeled DNA was desalted and separated from any unbound oligonucleotides using illustra MicroSpin S-200 HR columns (GE Healthcare Life Sciences; Piscataway Township, NJ), according to the manufacturer's protocol. The concentration of the resulting end-labeled λ DNA was measured using a NanoDrop2000 spectrometer (Thermo Scientific; Hanover Park, IL), and the integrity of the DNA (proper length) was confirmed using agarose gel electrophoresis, comparing to unmodified (λ) DNA.

Preparing Mixed Lipid Stocks

An unused glass test tube was first rinsed with ethanol (Fisher Scientific; Waltham, MA) and dried in an oven at 120 °C for 20 min. Then, using Hamilton (Hamilton Company; Reno, NV) syringes cleaned with chloroform, 1 mL of 20 mg/mL DOPC (18:1 (9-Cis) PC (DOPC) 1,2-dioleoyl-sn-glycero-3-phosphocholine; Avanti Polar Lipids; Alabaster, AL), 0.160 mL of 10 mg/mL DOPE-mPEG (18:1 PEG550 PE 1,2-dioleoyl-sn-glycero-3-phosphoethanolamine-N-[methoxy(polyethylene glycol)-550]; Avanti Polar Lipids; Alabaster, AL), and 0.010 mL of 10 mg/mL DOPE-biotin (16:0 Biotinyl Cap PE 1,2-dipalmitoyl-sn-glycero-3-phosphoethanolamine-N-(cap biotinyl); Avanti Polar Lipids; Alabaster, AL) lipid stocks were added to the dried glass test tube. The chloroform was evaporated from this lipid mixture by carefully blowing nitrogen gas onto the liquid and then placing the test tube under vacuum overnight.

The next day, the dried lipid cake was rehydrated by incubation in 2 mL of lipid buffer (10 mM Tris-HCl (Promega; Fitchberg, WI), pH 7.8, 100 mM NaCl (Sigma-Aldrich; St-Louis MO) for $\geq$ 5 h. The hydrated lipid mixture was then resuspended completely in solution by vortexing for 2 min to yield a milky suspension of large multilamellar vesicles (LMVs). The LMVs were then broken down into SUVs by sonication in a water bath sonicator specifically designed for preparation of SUVs

(in Ari Gafni's lab, University of Michigan), by sonicating the suspension until its appearance changed from milky white to nearly clear, but still slightly hazy. The vesicles were further broken down by a single pass through a 0.22 μm syringe filter and stored at 4 °C for up to 2 weeks. The final lipid concentrations are 10 mg/mL DOPC with 0.5 % (w/w) DOPE-biotin and 8 % (w/w) DOPE-mPEG.

Nanofabrication of Lipid Diffusion Barriers

All nanofabrication was performed by Ashwin Panday (L. Jay Guo's lab, University of Michigan). Briefly, glass coverslips (No. 1.5, 24 x 30 mm; VWR; Radnor, PA) were first spin-coated with a layer of a non-conducting polymer and then a layer of a conducting polymer. The barrier patterns were then written on the polymer layers by e-beam lithography. The polymeric coatings were then removed from the patterns by developing: rinsing with water and then a developing agent. Chromium was then deposited onto the glass laid bare by developing using e-beam evaporator to achieve a deposition (*i.e.*, barrier) thickness of $\approx$ 25 nm. Chromium was then removed from non-patterned areas (where the polymeric coating remains) using a lift-off protocol (*e.g.*, utilizing acetone).

Construction of Flowcells

Nanofabricated coverslips (see section 'Nanofabrication of Lipid Diffusion Barriers') are rinsed in filtered MilliQ water, gently agitated in 2 % Hellmanex cleaning solution (Sigma-Aldrich; St-Louis MO) for 1 h, rinsed thoroughly in water, soaked in 1M NaOH (Fisher Scientific; Waltham, MA) for 1 h, and rinsed again with water and 100 % methanol (Fisher Scientific; Waltham, MA). The coverslips are then dried under a nitrogen steam and baked at 120 °C in an oven for 1 h.

Next, a segment of double-sided tape is masked off with a 30 x 5 mm strip of paper. This double-sided tape is placed over a glass slide (Fischer Scientific, Waltham, MA),

cleaned by the same protocol above, with two holes drilled 22 mm apart using a 1.5 mm diamond coated drill bit (Shor International Corporation; Newark, NJ), so that the paper covers both drilled holes and the chromium barriers. The paper strip is then cut out of the tape using a razor. The clean and dry patterned coverslip is then placed over the double-sided tape, and excess tape not covered by the coverslip is removed with a razor. To melt the tape to achieve a uniform channel depth, the flowcell is sandwiched between two clean glass microscope slides, even pressure is applied on the taped area with four small binder clips, and the flowcell is baked in an oven at 120 °C for 45-60 min. NanoPorts (IDEX Corporation; Lake Forest, IL) are then attached to the slide side of the flowcell assembly with fast-setting Epoxy. The assembled flowcells are stored at 4 °C under vacuum for $\leq$ 1 week without significant degradation to the flowcell surface and lipid bilayer fluidity.

Preparation of DNA Curtains

First, a 5 mL syringe full of water is attached to one of the NanoPorts and the flowcell is rinsed with water, while tapping gently. Tapping the flowcell loosens and flushes out all air bubbles within the system. Air bubbles must be avoided, as even a small bubble will ruin the lipid bilayer surface. All subsequent syringes must be attached to the system by making drop-to-drop Luer lock connections. Next, the flowcell is washed with 3 ml Lipids Buffer (see section 'Preparing Mixed Lipid Stocks') by attaching a 5 ml Luer lock syringe to the second NanoPort (alternating between the two NanoPorts reduces the chance of injecting air bubbles into the tubing). Next, the mixed lipid stock (see section 'Preparing Mixed Lipid Stocks') is diluted 40 μL into 960 μL of Lipid Buffer and injected into the flowcell using a 1 mL syringe as a series of three injections, incubating 10 min between injections. The unbound lipids are then removed by rinsing the flowcell with 3 mL Lipid Buffer in a 3 mL syringe. The flowcell is then incubated for 30 min to promote vesicle fusion and bilayer growth along the

silica surface. Next, to block any remaining exposed glass, 1 mL BSA Buffer (40 mM Tris-Cl, pH 7.8, 0.2 mg/mL BSA (Sigma-Aldrich; St-Louis, MO), 1 mM $MgCl_2$, 1 mM DTT; prepare this buffer fresh just before use) is injected slowly from a 1 mL syringe and the flowcell is incubated for 10 min. To allow lipid-biotin-streptavidin-biotin-DNA linkages, 12 μL of 0.1 mg/mL streptavidin is diluted in 500 μL BSA Buffer and injected using a 1 mL syringe as a series of two injections, incubating 15 min between injections. To flush out unbound streptavidin, the flowcell is then rinsed with 3 mL of BSA buffer. Next, 1 mL of 100 pM end-labeled λ in BSA Buffer is injected into the flowcell using a 1 mL syringe as a series of three injections, incubating 5 min between injections to allow for DNA binding to the lipid bilayer surface. The amount of injected DNA may be adjusted to obtain the desired DNA surface density. Finally, the unbound DNA is rinsed out of the flowcell with 3 ml BSA Buffer.

Imaging DNA Curtains with TIRFM

The flowcell was transferred to the microscope syringe pump system and 0.5 pM POPO-3 (Invitrogen Molecular Probes; Eugene, OR) in BSA Buffer was flown onto the cell at 0.1 mL/min for 5-10 min prior to imaging. Images were taken on an inverted fluorescence microscope (model IX81, Olympus, Center Valley, PA) using a 60x objective lens. Samples were illuminated at 532 nm (type Compass 315M, Coherent Inc., Santa Clara, CA) at the critical angle, using a cellˆ TIRF^{TM} Illuminator (Olympus, Center Valley, PA). Fluorescent emissions were split into four separate channels using a QV2 Quad View Imaging System (Photometrics, Tuscon, AZ) and projected onto an EMCCD camera (model Evolve 512, Photometrics, Tuscon, AZ). Fluorescent images were viewed using MetaMorph software (Molecular Devices, Sunnyvale, CA).

Results and Discussion

DNA Does Not Bind Lipids on Coverslip Surface

No DNA curtains were formed, and no DNA was observed bound to lipids on the coverslip surface, using this protocol. Potential reasons for these technical difficulties include (1) lipid bilayer is not being formed on coverslip surface; (2) lipid bilayer is formed on coverslip surface, but is not fluid; and (3) 'end-labeled' DNA is not labeled with biotin. Improvements made to the lipid preparation protocol (reflected in the section 'Preparing Mixed Lipid Stocks' above), and TIRFM experiments done by Alex Johnson-Buck and Soma Dhakal (data not shown), show that bilayer fluidity was an issue initially, but has since been resolved by the improvements to the lipid preparation protocol. Efforts are now being made by Soma Dhakal to confirm the biotin labeling of the λ DNA.

APPENDIX C

A Study of *E. coli* RNA Polymerase Hydrolysis Efficiencies of γ-[Fluorescently]Labeled NTPs

Introduction[1]

Another type of protein-DNA interaction that is investigated in this dissertation was transcriptional elongation; more specifically, the sequence-specific kinetics of transcriptional elongation. The motivation for this specific goal was riboswitches. Genetic regulation by riboswitches—RNA domains of complex folds that switch conformation upon metabolic cues—is one recently discovered paradigm that contributes to the complex regulatory network employed by the cell. The formation of riboswitches can either cause the premature termination of transcription or prevent the initiation of translation.[119] Riboswitches regulate several metabolic pathways in bacteria by directly binding specific metabolites,[119,120] and accordingly present a potential target for novel, highly effective antibiotics, which are much needed.[121]

An appreciation for the contribution of RNA to genetic regulatory mechanisms has only recently developed, and therefore, the mechanisms employed by riboswitches

[1]This project was conducted in collaboration with Krishna Suddhala.

are not well understood. For example, little is known concerning the kinetics of riboswitching.[120] However, due to recent technological advances made by Pacific Biosciences, it is now possible to directly investigate the kinetics of riboswitch formation in real-time. Pacific Biosciences has successfully developed a technology termed single-molecule, real-time (SMRT^{TM}) sequencing to monitor DNA replication, a process very similar to RNA transcription, with single-nucleotide resolution.[122] To this end, the company developed a fluorescence assay that utilizes deoxyribonucleotides labeled on the γ-phosphate with four spectrally-distinguishable, fluorescent probes. In order to obtain background levels low enough to allow single-molecule detection, they performed the assay in zero-mode waveguides (ZMWs), nanophotonic structures that confine the fluorescent excitation volume to zeptoliters, and imaged the reaction using total internal reflection fluorescence microscopy (TIRFM).[122]

It is plausible that this system may easily be adapted to monitor RNA transcription by replacing fluorescently-labeled deoxyribonucleotides with fluorescently-labeled ribonucleotides and DNA polymerase with RNA polymerase. Binding of a complementary ribonucleotide to the DNA transcription template within the active site of RNA polymerase will be signaled by a transient, nucleotide-specific, fluorescence that ends when the nucleotide is incorporated into the growing RNA strand and the attached label diffuses into solution (with the cleaved pyrophosphate). Thus, the resulting records will define the complete, sequence-specific, kinetic information of RNA polymerase activity, including the rates of nucleotide binding and incorporation. Consequently, if using a DNA sequence known to code for a riboswitch that causes the premature termination of transcription, with the addition of the necessary metabolite, the kinetics of riboswitching and gene regulation could be monitored as transcription is proceeding. Such a single-molecule approach holds the promise for the unique dissection of the molecular basis for riboswitch-mediated bacterial gene regulation.

As a result of a collaboration with Pacific Biosciences, three different γ-phosphate labeled ribonucleotides were obtained from this company. In addition, two additional γ-phosphate labeled ribonucleotides were purchased from alternative commercial sources. Using thin-layer chromatography (TLC), the extent of hydrolysis of these ribonucleotides by *E. coli* RNA polymerase was measured, following *in vitro* transcription reactions. Preliminary data show that none of the five γ-phosphate labeled ribonucleotides could be hydrolyzed by *E. coli* RNA polymerase.

Materials and Methods

Materials

E. coli RNA polymerase core enzyme and Kool NC-45 Universal RNA Polymerase Template were purchased from Epicentre Biotechnologies (Madison, WI); ATP-hexapentaphosphate, GTP-hexapentaphosphate, and CTP-hexapentaphosphate were provided by Pacific Biosciences (Menlo Park, CA); γ-[6-Aminohexyl]-ATP-Cy3 from Jena Biosciences (Jena, Germany); Guanosine 5'-O-(3-thiotriphosphate)BODIPY FL were purchased from Invitrogen Molecular Probes (Eugene, OR); and *Crotalus adamanteus* Phosphodiesterase I from United States Biochemical (Cleveland, OH). TLC plates and all other chemicals and reagents were purchased from Sigma-Aldrich (St. Louis, MO).

In vitro Transcription Assays

E. coli core enzyme (0.1 U/μl) was mixed with Kool NC-45 Universal RNA Polymerase Template (50 nM), unlabeled ATP, GTP, CTP, and TTP (1 mM each), dithiothreitol (DTT) (5 mM), $MnCl_2$ (10 mM), and pyrophosphatase (0.01 U/μl) in transcription buffer (40 mM Tris-HCl, pH 7.5, 150 mM KCl, 10 mM $MgCl_2$, and 0.01 % Triton-X-100). One of the following γ-phosphate labeled ribonucleotides were

added to a final concentration of 10 μM: (1) ATP-hexapentaphosphate; (2) GTP-hexapentaphosphate; (3) CTP-hexapentaphosphate; (4) γ-[6-Aminohexyl]-ATP-Cy3; or (5) Guanosine 5'-O-(3-thiotriphosphate)BODIPY FL. The reaction mixture was then incubated at 37 °C for 3 h. At this point, transcription was halted by the addition of EDTA to a final concentration of 18 mM.

In vitro Phosphodiesterase Hydrolysis Assays

C. adamanteus Phosphodiesterase I (PDE) was mixed with either: (1) ATP-hexapentaphosphate; (2) GTP-hexapentaphosphate; (3) CTP-hexapentaphosphate; (4) γ-[6-Aminohexyl]-ATP-Cy3; or (5) Guanosine 5'-O-(3-thiotriphosphate)BODIPY FL in PDE reaction buffer (100 mM Tris-HCl, pH 8.9, 100 mM NaCl, and 14 mM $MgCl_2$). The reaction mixture was then incubated at room temperature for 5 min. At this point, the hydrolysis reaction was halted by placing the mixture on ice.

Thin-Layer Chromatography (TLC)

Transcription or PDE reaction samples were diluted 1:100 in either transcription buffer or PDE reaction buffer, respectively. 0.5 μl of each sample was spotted onto silica plastic-backed TLC plates containing no fluorescent indicator. The following eluent mixture was used, freshly prepared each time (modified from Draganescu *et al.*[123]): 33:33:14:20 of 2-propanol:NH_4OH:1,4-dioxane:H2O. Samples were visualized using a Typhoon Scanner (GE Healthcare Life Sciences; Pittsburgh, PA) in fluorescence mode, using the following excitation/emission combinations for each γ-phosphate labeled ribonucleotide: (1) 633 nm/670bp30 nm for ATP-hexapentaphosphate and CTP-hexapentaphosphate; (2) 532 nm/580bp40 nm for γ-[6-Aminohexyl]-ATP-Cy3; and (3) 532 nm/526sp nm for GTP-hexapentaphosphate and Guanosine 5'-O-(3-thiotriphosphate)BODIPY FL.

Results and Discussion

E. coli RNA Polymerase Does Not Hydrolyze γ-Phosphate Labeled Ribonucleotides

As a first step towards developing a transcription assay capable of real-time, single-nucleotide resolution using zero-mode waveguide (ZMW) technology, a γ-phosphate labeled ribonucleotide was sought that could be cleaved by *E. coli* RNA polymerase *in vitro*. For these experiments, five different labeled ribonucleotides were used: (1) ATP-hexapentaphosphate (FL-ATP); (2) GTP-hexapentaphosphate (FL-GTP); (3) CTP-hexapentaphosphate (FL-CTP); (4) γ-[6-Aminohexyl]-ATP-Cy3 (Cy3-ATP); and (5) Guanosine 5'-O-(3-thiotriphosphate)BODIPY FL (GpppBODIPY) (Figure C.1).

Inspired by the methods of Draganescu *et al.*, the hydrolysis efficiency of these γ-phosphate labeled ribonucleotides by *E. coli* RNA polymerase was measured using thin-layer chromatography (TLC).[123] In this previous study, the authors used TLC to monitor the hydrolysis of GpppBODIPY by the polyphosphatase Fhit. As a positive control, hydrolysis assays using the *C. adamanteus* phosphodiesterase, which is known to efficiently hydrolyze GpppBODIPY,[124] were run in parallel to all transcription reactions.

All transcription reactions (Tx+) were run with a transcription negative control which contained no polymerase (Tx-), a PDE positive control (Px+), and a PDE negative control, which contained no PDE (Px-), where "x" denotes the number of labeled ribonucleotide used. The ribonucleotides were numbered as follows: (1) FL-ATP; (2) FL-GTP; (3) FL-CTP; (4) Cy3-ATP; and (5) GpppBODIPY. Figure C.2 shows TLC plates for all five labeled ribonucleotides. Figures C.2a-c demonstrate positive ribonucleotide hydrolysis by PDE for ribonucleotides 1-3. For the transcription reactions, there is no noticeable difference in the enzyme positive and enzyme negative samples, for any of the five ribonucleotides.

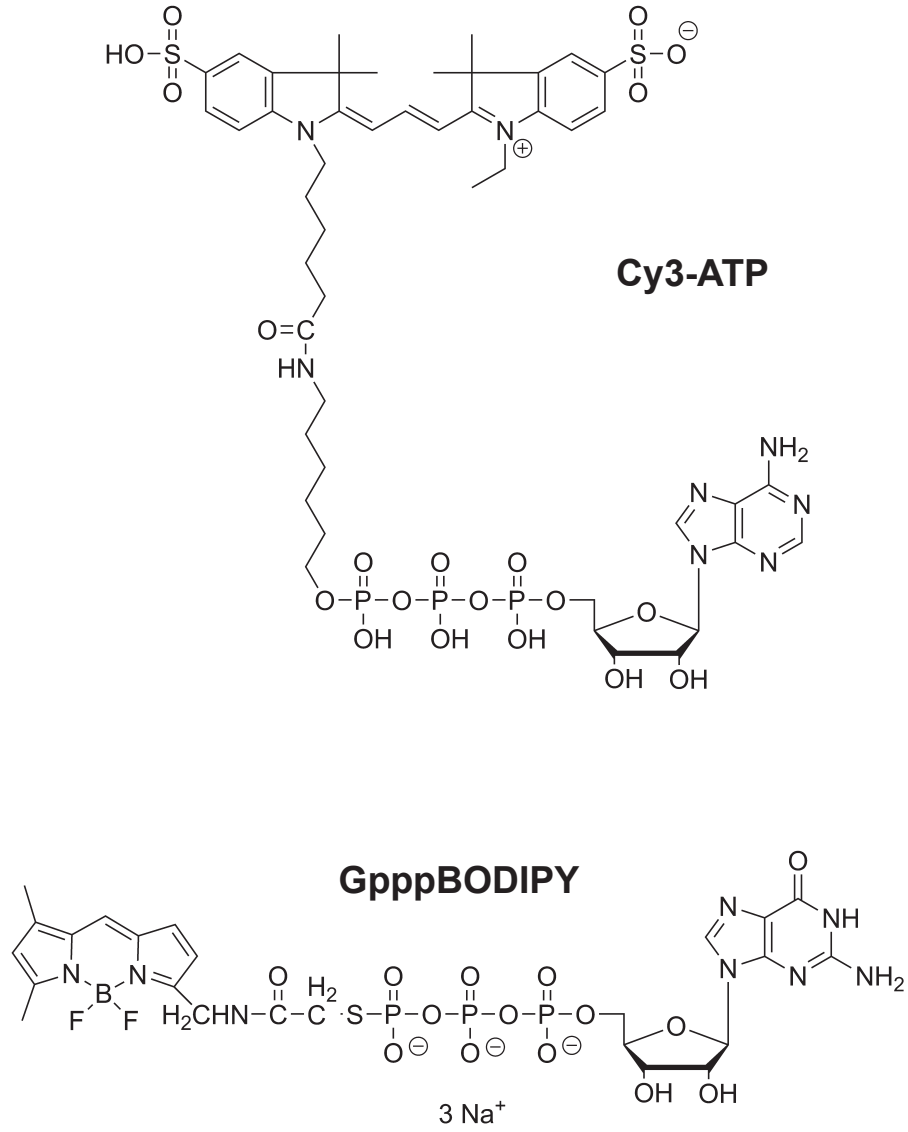

Figure C.1: Chemical structures of γ-[6-Aminohexyl]-ATP-Cy3 (Cy3-ATP) shown on top and Guanosine 5'-O-(3-thiotriphosphate)BODIPY FL (GpppBODIPY) shown on bottom. Chemical structures of the other three labeled ribonucleotides used in this study were not available.

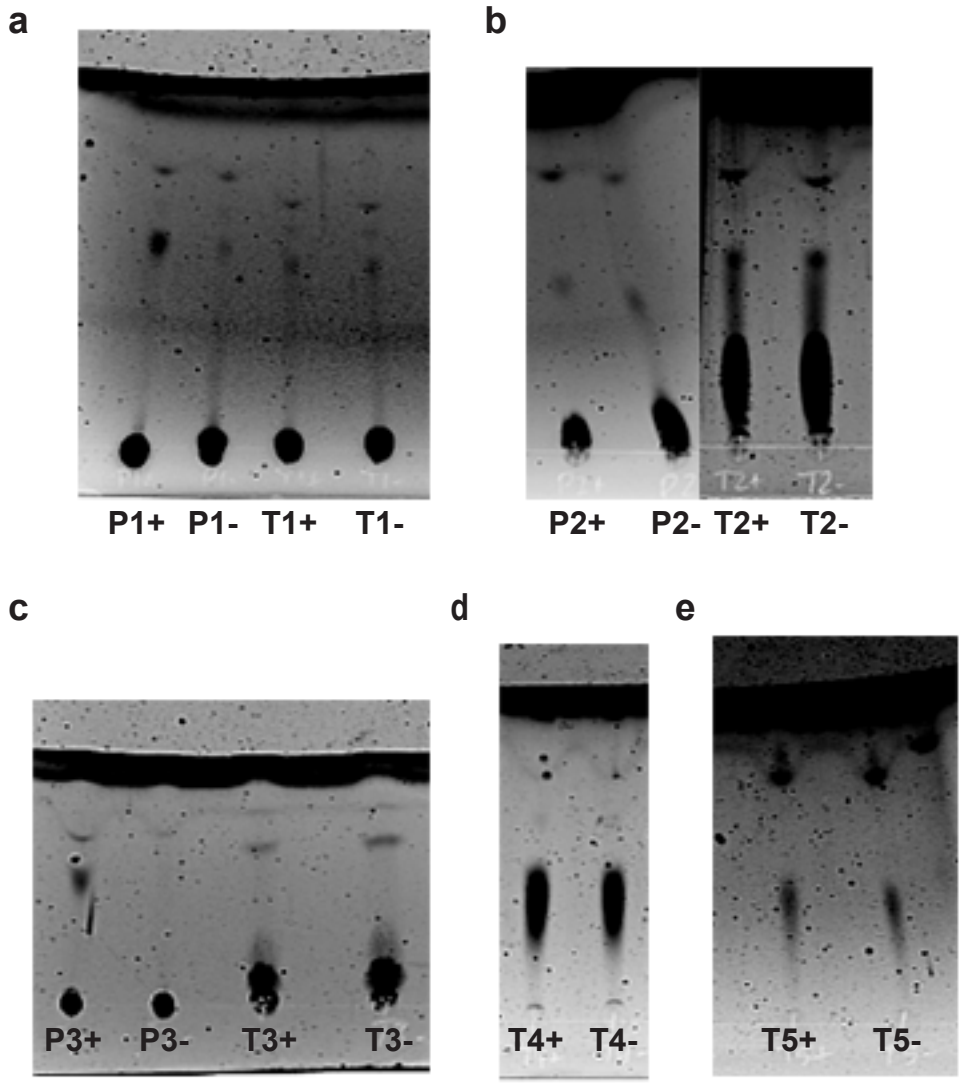

Figure C.2: Cleaved and uncleaved γ-phosphate labeled ribonucleotides separated by TLC. Samples labeled "P" are run in PDE reaction buffer, samples labeled "T" in transcription buffer. Samples labeled "+" include either PDE or *E. coli* RNA polymerase, respective of which buffer they were run in, samples labeled "-" do not include enzyme. γ-phosphate labeled ribonucleotides are numbered as follows: (1) FL-ATP (a); (2) FL-GTP (b); (3) FL-CTP (c); (4) Cy3-ATP (d); and (5) GpppBODIPY (e).

Conclusions

From the TLC separations, it does not appear that *E. coli* RNA polymerase is able to hydrolyze any of the five γ-phosphate labeled ribonucleotides used in this study. Future work should be performed to develop such a sensitive transcription assay, considering such options as: (1) future optimization of transcription conditions for hydrolysis of γ-phosphate labeled ribonucleotides by *E. coli* RNA polymerase; (2) use of a RNA polymerase from another organism; (3) mutation of RNA polymerase to better accommodate modified ribonucleotides; or (4) an alternative strategy not utilizing γ-phosphate labeled ribonucleotides.

APPENDIX D

MATLAB Code for Quantification of Microtubule Bundling from TEM Images

```
% The purpose of this script is to measure microtubule length and diameter from
% TEM images in order to estimate the degree of microtubule bundling in a
% sample.
% The diameter of a microtubule in a user-selected ROI is measured

% at n (sep) pixel intervals. Parameter 'sep' is defined on line 93. The
% diameter of a unbundled microtubule is pre-defined as the mean of an
% unbundled population within 2 standard deviations (can re-define on line
% 137). This diameter range is assigned a weight of 1. Higher weights,
% representing bundles of microtubules containing x microtubules, are
% assigned as multiples of the 1st diameter range.
% Input is a JPEG image. Output is the array length = [unbundlength

% bundlength totlength]. These parameters represent the total measured
% unbundled length, total measured bundled length, and total measured
% length, respectively.
```

```
clear all;
close all;

% Read in a JPEG image
disp('Which image do you want to analyze?')
[imagefile,imagepath,imagefi] = uigetfile('*.jpg');
imagename=strcat(imagepath,imagefile);
im = imread(imagename);
im_grayscale = rgb2gray(im);
im_complement = imcomplement(im_grayscale);

% First, morphologically open then adjust contrast of image to correct for
%"dye shadowing" around MT edges (decrease the maximum display value).
%Adjust maxdisp until shadowing can no longer be seen. Adjust mindisp until
%MT object appears solid. Values for mindisp & maxdisp must be between
%[0.0 1.0].
% SE = strel('ball',25,25,0);
% bkgnd = imopen(im_complement,SE);
% im_open = im_complement - bkgnd;
% figure,imshow(im_open,'InitialMagnification',25)

maxdisp = 0.6;
mindisp = 0.5;
con_adj_im = imadjust(im_complement,[mindisp maxdisp],[0 1]);
imshow(con_adj_im,'InitialMagnification',25), title('Contrast_Adj');
s=1;
while s == 1
```

```
strResponse = input('Adjust contrast? (y/n)','s');
if strResponse == 'y'
maxdisp = input('Maxdisp?');
mindisp = input('Mindisp?');
con_adj_im = imadjust(im_complement,[mindisp maxdisp],[0 1]);
imshow(con_adj_im,'InitialMagnification',25), title('Contrast_Adj');
else s = 0;
end
end

% Create a binary version of the image
level = graythresh(con_adj_im);
bw =  im2bw(con_adj_im,level);
bw_comp = imcomplement(bw); imshow(bw_comp,'InitialMagnification',25), title('Binary');

% Morphologically transform image so that MTs are solid objects in the bw
% image.
SE = strel('square',10);
closed_im = imclose(bw_comp,SE);
spursgone = bwmorph(closed_im,'spur',10);
imshow(spursgone,'InitialMagnification',25), title('Closed');

%Remove objects that are not MTs
MTs_only = bwareaopen(spursgone,10000);
imshow(MTs_only,'InitialMagnification',25),title('MTs_only');
```

```
%Loop remainder of program until all microtubule sections analyzed.
s = 1;
while s == 1
close all;
%Crop out MT section to be analyzed
disp('Crop out MT section to be analyzed. Enter when done.')
cropped = imcrop(MTs_only);

disp('Select MT section to be analyzed. Enter when done.')
MT = bwselect(cropped);

%Align x axis of MT section with major axis of MT section
d = diameter(MT);
[aligned,~] = x2majoraxis(d.MajorAxis, MT);
imshow(aligned,'InitialMagnification',25), title('Aligned to MajorAxis');
r=1;
while r == 1
strResponse = input('Rotate an additional 45 deg cw? (y/n)','s');
if strResponse == 'y'
aligned = imrotate(aligned,-45);
imshow(aligned,'InitialMagnification',25), title('Rotated 45 deg');
else r=0;
end
end

%Compute boundaries.
%B = Px1 cell array; P = # of boundaries.
```

```
[B,~,~,~] = bwboundaries(aligned,'noholes');
boundim = bound2im(B1,size(aligned,1),size(aligned,2));
figure, imshow(boundim,'InitialMagnification',25), title('Boundary');

% Subsample boundary, i.e. select points on boundary that are seperated by
% n (sep) pixels, for all MTs, using self-written functions.
sep = 10; MT_boundary = B1;
subsampbound = MT_boundary(1:sep:length(MT_boundary),:);
subsampboundim = bound2im(subsampbound,size(boundim,1),size(boundim,2));
figure, imshow(subsampboundim,'InitialMagnification',25), title('Subsampled Boundary');

%Crop out long edges of MT, so that ends are not included
disp('Crop out MT section, excluding edges. Double-click to finish.')
cropped2 = imcrop(subsampboundim);

% Calculate diameter at uniform pixel intervals along the diameter. Pixel
% interval determined by variable "sep" defined above.
s = size(subsampbound);
h = round(s(1)/2);
%subsampbound(1,:)=[]; flipped = flipud(subsampbound);
subsampbound(h:end,:)=[]; %subsampbound(1:35,:)=[];flipped(h:end,:)=[]; %flipped(1,:)=[];
s = size(subsampbound);
dia = zeros(s(1),1);
for t=1:s(1)
dia(t,1) = pdist2(subsampbound(t,:),flipped(t,:));
end
```

```
% Calculate mean of unbundled MT diameter & remove outliers due to errors
% in measurement routine (these outliers can occur at the MT tip or at
% locations of staining artifacts).
% Define outliers as data points which are further than 2 standard
% deviations from the mean.
mu = mean(dia);
sig = std(dia);
outliers = abs(dia-mu) ¿ 2*sig;
dia(any(outliers)) = [];
mu = mean(dia);
s = size(dia);

% Calculate diameter weights, based on mean diameter of single, unbundled
% MTs.
w1 = 32.95685423; wts = zeros(s(1),1);
for i = 1:s(1)
if dia(i,1) ≤ w1,
wts(i,1) = 1;
elseif dia(i,1) ≤ 2*w1,
wts(i,1) = 2;
elseif dia(i,1) ≤ 3*w1,
wts(i,1) = 3;
elseif dia(i,1) ≤ 4*w1,
wts(i,1) = 4;
elseif dia(i,1) ≤ 5*w1,
wts(i,1) = 5;
```

elseif dia(i,1) $\leq$ 6*w1,

wts(i,1) = 6;

elseif dia(i,1) $\leq$ 7*w1,

wts(i,1) = 7;

elseif dia(i,1) $\leq$ 8*w1,

wts(i,1) = 8;

elseif dia(i,1) $\leq$ 9*w1,

wts(i,1) = 9;

elseif dia(i,1) $\leq$ 10*w1,

wts(i,1) = 10;

elseif dia(i,1) $\leq$ 11*w1,

wts(i,1) = 11;

elseif dia(i,1) $\leq$ 12*w1,

wts(i,1) = 12;

elseif dia(i,1) $\leq$ 13*w1,

wts(i,1) = 13;

elseif dia(i,1) $\leq$ 14*w1,

wts(i,1) = 14;

elseif dia(i,1) $\leq$ 15*w1,

wts(i,1) = 15;

elseif dia(i,1) $\leq$ 16*w1,

wts(i,1) = 16;

elseif dia(i,1) $\leq$ 17*w1,

wts(i,1) = 17;

elseif dia(i,1) $\leq$ 18*w1,

wts(i,1) = 18;

elseif dia(i,1) $\leq$ 19*w1,

wts(i,1) = 19;

elseif dia(i,1) ≤ 20*w1,

wts(i,1) = 20;

elseif dia(i,1) ≤ 21*w1,

wts(i,1) = 21;

elseif dia(i,1) ≤ 22*w1,

wts(i,1) = 22;

elseif dia(i,1) ≤ 23*w1,

wts(i,1) = 23;

elseif dia(i,1) ≤ 24*w1,

wts(i,1) = 24;

elseif dia(i,1) ≤ 25*w1,

wts(i,1) = 25;

elseif dia(i,1) ≤ 26*w1,

wts(i,1) = 26;

elseif dia(i,1) ≤ 27*w1,

wts(i,1) = 27;

elseif dia(i,1) ≤ 28*w1,

wts(i,1) = 28;

elseif dia(i,1) ≤ 29*w1,

wts(i,1) = 29;

elseif dia(i,1) ≤ 30*w1,

wts(i,1) = 30;

else disp('Need to create another weight level')

end

end

```
% Calculate weighted bundled & unbundled length, in pixels.
totwtlength = sum(sep*wts);
undia = zeros(s(1),1); for i = 1:s(1),
if wts(i,1) ¿ 1,
undia(i,1) = 0;
else
undia(i,1) = 1;
end
end
unbundlength = sum(sep*undia);
bundlength = totwtlength - unbundlength;
totlength = length(wts)*sep;
lengths = [unbundlength bundlength totlength];

findr = input('Do you want to analyze another MT? (y/n)','s');
if findr == 'y'
s=1;
else
s=0;
end
end
```

APPENDIX E

MATLAB Code for Quantification of Microtubule Bundling from TIRFM Images

```
%This script takes multiple lines scans at a set pixel interval across the
%x-dimension of a rectangular ROI, which the user has defined to include a
%single microtubule. These lines scans are then fit with Gaussian functions
%to find the axis of the microtubule. The axis is then used to rotate the
%image so that the x-axis is aligned with the microtubule axis. Line scans
%are then taken again and fit with Gaussians which are then integrated to
%determine the total cross-sectional fluorescence intensity.

%Input in TIFF image (image file name on line 22).
%Output is matrix "MT_stats", see script for details.

%This script uses Matlab's Curve Fitting Toolbox.

clear all;
close all;
```

```
%User-defined parameters; to be inputted before running script.
px = 5; %Input desired pixel interval between line scans
r2 = 0.80; %R^2 threshold for acceptance of Gaussian fits when determining MT axis
endpts
res = 0.267; %Resolution of image in um/px
w1 = 1.899962; %mean diameter of 20 single MTs minus 1 standard deviation
range = 1.61836; %2*SD
imagename = '110105_MTs_3fM_80nmPAANPs_600ms_488_3.tif';
frame = 1;

%Read in a TIFF image; index = frame #
im = imread(imagename,'Index',frame);

%Crop to only include MT(TMR/Cy3) channel.
MTchannel = imcrop(im,[257 1 255 255]);

%Correct non-uniform background with morphological opening; structuring
%element is disk of radius 5
%Adjust image contrast
%Subtract background again
bkgnd = imopen(MTchannel,strel('disk',5));
bkgndcorrected = imadjust(MTchannel - bkgnd);
J = imadjust(bkgndcorrected,[0.4;1.0],[0;1.0]);

%120530 Draw rectangular ROI around a single MT
h = imshow(J);
r = imrect;
```

```
position = wait(r);
pos = getPosition(r);
width = pos(3);
height = pos(4);

%Crop out MT
%If the MT is mostly vertical, it will be rotated 90 deg.
disp('Crop out MT section to be analyzed. Press enter when done.')
MTcrop = imcrop(J,pos);
if width > height
MTcrop;
else
MTcrop = imrotate(MTcrop,90);
end
%imshow(MTcrop)
width = size(MTcrop,2)-1;
height = size(MTcrop,1)-1;

%Number of line scans taken
num_ls = floor(width/px);

%120601 Take line scans at 'px' pixel intervals along the x-axis of the
%cropped image
%120618 Determine points of MT axis by fitting intensity vectors with
%Gaussian functions
cx = zeros(height-1,num_ls);
cy = zeros(height-1,num_ls);
```

```
c = zeros(height-1,num_ls);
MTaxis = zeros(num_ls,2);
for n = 1:num_ls
[cx(:,n),cy(:,n),c(:,n)] = improfile(MTcrop,[(5*n)-4 (5*n)-4],[1 height-1]);
[gaussfit,gof] = fit(cy(:,n),c(:,n),'gauss1');
if gof.rsquare ≥ r2
MTaxis(n,1) = cx(1,n);
MTaxis(n,2) = gaussfit.b1;
end
end

%Determine endpts of MT axis
for n = 1:num_ls
if all(MTaxis(n,:))== 1
MTaxis_endpts(1,:) = MTaxis(n,:);
break
end
end
MTaxis_flipped = flipud(MTaxis);
for n = 1:num_ls
if all(MTaxis_flipped(n,:))== 1
MTaxis_endpts(2,:) = MTaxis_flipped(n,:);
break
end
end
```

```
%Rotate image so that MT axis aligns with x-axis of image.
MTangle = atand((MTaxis_endpts(2,1)-MTaxis_endpts(1,1))/(MTaxis_endpts(2,2)-MTaxis_-
endpts(1,2)));
MTrotate = imrotate(MTcrop,90-MTangle);
%figure, imshow(MTrotate)
width = size(MTrotate,2)-1;
height = size(MTrotate,1)-1;

%Number of line scans to take for image of rotated MT
num_ls_2 = floor(width/px);

%Take line scans of the rotated MT, again at 'px' pixel intervals along the
%x-axis.
%120618 Normalize intensity matrix c_2 to c_2_norm. Normalize by highest
%intensity possible for # bits in image.
%Fit Gaussian functions to each line scan. Store the xmin, ymin, width, and
%height of the original, user selected ROI into columns 1-4, respectively,
%of the matrix,MT_stats. Store the R^2, mean, standard error, and area
%under curve of the 2nd round of Gaussian fits in columns 5-8,
%respectively, of MT_stats.
info = imfinfo(imagename);
bits = info.BitsPerSample;
int_max = (2^bits)-1;
cx_2 = zeros(height-1,num_ls_2-1);
cy_2 = zeros(height-1,num_ls_2-1);
c_2 = zeros(height-1,num_ls_2-1);
MT_stats = zeros(num_ls_2-1,9);
```

```
MT_stats(1,1:4) = [pos(1) pos(2) pos(3) pos(4)];
for i = 1:2
for n = 2:num_ls_2
[cx_2(:,n),cy_2(:,n),c_2(:,n)] = improfile(MTrotate,[(5*n)-4 (5*n)-4],[1 height-1]);
c_2_norm = c_2/int_max;
[gaussfit,gof] = fit(cy_2(:,n),c_2_norm(:,n),'gauss1');
int = integrate(gaussfit,cx_2(1,:),cx_2(1,1));
area = int(num_ls_2-1)-int(1);

% Calculate diameter weights, based on mean diameter of single, unbundled
% MTs.
if area ≤ w1,
wt = 0;
elseif area ≤ range+w1,
wt = 1;
elseif area ≤ (2*range)+w1,
wt = 2;
elseif area ≤ (3*range)+w1,
wt = 3;
elseif area ≤ (4*range)+w1,
wt = 4;
elseif area ≤ (5*range)+w1,
wt = 5;
elseif area ≤ (6*range)+w1,
wt = 6;
elseif area ≤ (7*range)+w1,
wt = 7;
```

elseif area ≤ (8*range)+w1,

wt = 8;

elseif area ≤ (9*range)+w1,

wt = 9;

elseif area ≤ (10*range)+w1,

wt = 10;

elseif area ≤ (11*range)+w1,

wt = 11;

elseif area ≤ (12*range)+w1,

wt = 12;

elseif area ≤ (13*range)+w1,

wt = 13;

elseif area ≤ (14*range)+w1,

wt = 14;

elseif area ≤ (15*range)+w1,

wt = 15;

elseif area ≤ (16*range)+w1,

wt = 16;

elseif area ≤ (17*range)+w1,

wt = 17;

elseif area ≤ (18*range)+w1,

wt = 18;

elseif area ≤ (19*range)+w1,

wt = 19;

elseif area ≤ (20*range)+w1,

wt = 20;

elseif area ≤ (21*range)+w1,

wt = 21;

elseif area ≤ (22*range)+w1,

wt = 22;

elseif area ≤ (23*range)+w1,

wt = 23;

elseif area ≤ (24*range)+w1,

wt = 24;

elseif area ≤ (25*range)+w1,

wt = 25;

elseif area ≤ (26*range)+w1,

wt = 26;

elseif area ≤ (27*range)+w1,

wt = 27;

elseif area ≤ (28*range)+w1,

wt = 28;

elseif area ≤ (29*range)+w1,

wt = 29;

else disp('Need to create another weight level')

end

MT_stats(n-1,5:9) = [gof.rsquare gaussfit.b1 gof.rmse area wt];

end

end

BIBLIOGRAPHY

BIBLIOGRAPHY

[1] Lander, E. S. et al. *Nature* **2001**, *409*, 860–921.

[2] Benbow, R. M. *Sci Prog* **1992**, *76*, 425–50.

[3] Mirny, L. A.; Slutsky, M.; Wunderlich, Z.; Tafvizi, A.; Leith, J.; Kosmrlj, A. *J. Phys. A: Math. Theor.* **2009**, *42*, 4304013.

[4] Halford, S. E.; Marko, J. F. *Nucleic Acids Res* **2004**, *32*, 3040–52.

[5] Kolomeisky, A. B. *Phys Chem Chem Phys* **2011**, *13*, 2088–95.

[6] Halford, S. E. *Biochem Soc Trans* **2009**, *37*, 343–8.

[7] Wang, F.; Redding, S.; Finkelstein, I. J.; Gorman, J.; Reichman, D. R.; Greene, E. C. *Nat Struct Mol Biol* **2013**, *20*, 174–81.

[8] Blainey, P. C.; van Oijen, A. M.; Banerjee, A.; Verdine, G. L.; Xie, X. S. *Proc Natl Acad Sci U S A* **2006**, *103*, 5752–7.

[9] Jiao, Y.; Cherny, D. I.; Heim, G.; Jovin, T. M.; Schaffer, T. E. *J Mol Biol* **2001**, *314*, 233–43.

[10] Kim, J. H.; Larson, R. G. *Nucleic Acids Res* **2007**, *35*, 3848–58.

[11] Ramanathan, S. P.; van Aelst, K.; Sears, A.; Peakman, L. J.; Diffin, F. M.; Szczelkun, M. D.; Seidel, R. *Proc Natl Acad Sci U S A* **2009**, *106*, 1748–53.

[12] Wang, Y. M.; Austin, R. H.; Cox, E. C. *Phys Rev Lett* **2006**, *97*, 048302.

[13] Hammar, P.; Leroy, P.; Mahmutovic, A.; Marklund, E. G.; Berg, O. G.; Elf, J. *Science* **2012**, *336*, 1595–8.

[14] Yin, Y. W.; Steitz, T. A. *Science* **2002**, *298*, 1387–95.

[15] Schonhoft, J. D.; Stivers, J. T. *Nat Chem Biol* **2012**, *8*, 205–10.

[16] Francis, A. W.; David, S. S. *Biochemistry* **2003**, *42*, 801–10.

[17] Gowers, D. M.; Wilson, G. G.; Halford, S. E. *Proc Natl Acad Sci U S A* **2005**, *102*, 15883–8.

[18] Rohs, R.; Jin, X.; West, S. M.; Joshi, R.; Honig, B.; Mann, R. S. *Annu Rev Biochem* **2010**, *79*, 233–69.

[19] Sidorova, N. Y.; Rau, D. C. *J Mol Biol* **2001**, *310*, 801–16.

[20] Norberg, J. *Arch Biochem Biophys* **2003**, *410*, 48–68.

[21] Wang, J.; Gao, W. *ACS Nano* **2012**, *6*, 5745–51.

[22] Hong, Y. Y.; Velegol, D.; Chaturvedi, N.; Sen, A. *Physical Chemistry Chemical Physics* **2010**, *12*, 1423–1435.

[23] Kotov, N. A. *Science* **2010**, *330*, 188–9.

[24] Fant, K.; Esbjorner, E. K.; Lincoln, P.; Norden, B. *Biochemistry* **2008**, *47*, 1732–40.

[25] Minoura, I.; Katayama, E.; Sekimoto, K.; Muto, E. *Biophys J* **2010**, *98*, 1589–97.

[26] Kampmann, M. *J Biol Chem* **2004**, *279*, 38715–20.

[27] Shimamoto, N. *J Biol Chem* **1999**, *274*, 15293–6.

[28] Blainey, P. C.; Luo, G.; Kou, S. C.; Mangel, W. F.; Verdine, G. L.; Bagchi, B.; Xie, X. S. *Nat Struct Mol Biol* **2009**, *16*, 1224–9.

[29] Wang, T. H.; Wang, H. S.; Soong, Y. K. *Cancer* **2000**, *88*, 2619–2628.

[30] Marupudi, N. I.; Han, J. E.; Li, K. W.; Renard, V. M.; Tyler, B. M.; Brem, H. *Expert Opin. Drug Saf.* **2007**, *6*, 609–621.

[31] Liu, Y. J.; Zhang, B.; Yan, B. *Int. J. Mol. Sci.* **2011**, *12*, 4395–4413.

[32] Ali, I.; Rahis, U.; Salim, K.; Rather, M. A.; Wani, W. A.; Haque, A. *Curr. Cancer Drug Targets* **2011**, *11*, 135–146.

[33] Riggs, A. D.; Bourgeois, S.; Cohn, M. *J Mol Biol* **1970**, *53*, 401–17.

[34] Castoldi, M.; Popov, A. V. *Protein Expression Purif.* **2003**, *32*, 83–88.

[35] Kim, T.; Kao, M. T.; Hasselbrink, E. F.; Meyhofer, E. *Nano Lett.* **2007**, *7*, 211–217.

[36] Qin, M.; Hah, H. J.; Kim, G.; Nie, G.; Lee, Y. E.; Kopelman, R. *Photochem Photobiol Sci* **2011**, *10*, 832–41.

[37] Lund, K.; Manzo, A. J.; Dabby, N.; Michelotti, N.; Johnson-Buck, A.; Nangreave, J.; Taylor, S.; Pei, R.; Stojanovic, M. N.; Walter, N. G.; Winfree, E.; Yan, H. *Nature* **2010**, *465*, 206–10.

[38] Mullen, D. G.; Desai, A.; van Dongen, M. A.; Barash, M.; Baker, J., J. R.; Banaszak Holl, M. M. *Macromolecules* **2012**, *45*, 5316–5320.

[39] Majoros, I. J.; Thomas, T. P.; Mehta, C. B.; Baker, J. R. *J. Med. Chem.* **2005**, *48*, 5892–5899.

[40] Kusumi, A.; Sako, Y.; Yamamoto, M. *Biophys J* **1993**, *65*, 2021–40.

[41] Qian, H.; Sheetz, M. P.; Elson, E. L. *Biophys J* **1991**, *60*, 910–21.

[42] Saxton, M. J.; Jacobson, K. *Annu Rev Biophys Biomol Struct* **1997**, *26*, 373–99.

[43] Esfand, R.; Tomalia, D. A. *Drug Discovery Today* **2001**, *6*, 427–436.

[44] Tomalia, D. A.; Naylor, A. M.; Goddard, r., W. A. *Angew. Chem. Int. Ed. Engl.* **1990**, *29*, 138–175.

[45] Hu, L.; Grosberg, A. Y.; Bruinsma, R. *Biophys J* **2008**, *95*, 1151–6.

[46] Rohs, R.; West, S. M.; Sosinsky, A.; Liu, P.; Mann, R. S.; Honig, B. *Nature* **2009**, *461*, 1248–53.

[47] Tomalia, D. A.; Baker, H.; Dewald, J.; Hall, M.; Kallos, G.; Martin, S.; Roeck, J.; Ryder, J.; Smith, P. *Polym. J.* **1985**, *17*, 117–132.

[48] Baker, J. R. *Hematology Am. Soc. Hematol. Educ. Program* **2009**, 708–719.

[49] Yellepeddi, V. K.; Kumar, A.; Palakurthi, S. *Expert Opin. Drug Delivery* **2009**, *6*, 835–850.

[50] Cheng, Y.; Wang, J.; Rao, T.; He, X.; Xu, T. *Front. Biosci.* **2008**, *13*, 1447–1471.

[51] Tekade, R. K.; Kumar, P. V.; Jain, N. K. *Chem. Rev.* **2009**, *109*, 49–87.

[52] Nourse, A.; Millar, D. B.; Minton, A. P. *Biopolymers* **2000**, *53*, 316–328.

[53] Majoros, I. J.; Myc, A.; Thomas, T.; Mehta, C. B.; Baker, J. R. *Biomacromolecules* **2006**, *7*, 572–579.

[54] Mellado, W.; Magri, N. F.; Kingston, D. G.; Garcia-Arenas, R.; Orr, G. A.; Horwitz, S. B. *Biochem. Biophys. Res. Commun.* **1984**, *124*, 329–336.

[55] Gueritte-Voegelein, F.; Guenard, D.; Lavelle, F.; Le Goff, M. T.; Mangatal, L.; Potier, P. *J. Med. Chem.* **1991**, *34*, 992–998.

[56] Mathew, A. E.; Mejillano, M. R.; Nath, J. P.; Himes, R. H.; Stella, V. J. *J. Med. Chem.* **1992**, *35*, 145–151.

[57] Lim, J.; Chouai, A.; Lo, S. T.; Liu, W.; Sun, X.; Simanek, E. E. *Bioconjugate Chem.* **2009**, *20*, 2154–2161.

[58] Vrudhula, V. M.; MacMaster, J. F.; Li, Z.; Kerr, D. E.; Senter, P. D. *Bioorg. Med. Chem. Lett.* **2002**, *12*, 3591–3594.

[59] Davis, A.; Martinez, S.; Nelson, D.; Middleton, K. *Methods Cell Biol.* **2010**, *95*, 331–351.

[60] Ohi, M.; Li, Y.; Cheng, Y.; Walz, T. *Biol. Proced. Online* **2004**, *6*, 23–34.

[61] Zhao, F. Q.; Craig, R. *J. Struct. Biol.* **2003**, *141*, 43–52.

[62] Walter, N. G.; Huang, C. Y.; Manzo, A. J.; Sobhy, M. A. *Nat. Methods* **2008**, *5*, 475–489.

[63] Yang, J.; Chen, H.; Vlahov, I. R.; Cheng, J. X.; Low, P. S. *Proc. Natl. Acad. Sci. U. S. A.* **2006**, *103*, 13872–13877.

[64] Austin, C. D.; Wen, X.; Gazzard, L.; Nelson, C.; Scheller, R. H.; Scales, S. J. *Proc. Natl. Acad. Sci. U. S. A.* **2005**, *102*, 17987–17992.

[65] Li, M. H.; Choi, S. K.; Thomas, T. P.; Desai, A.; Lee, K. H.; Kotlyar, A.; Banaszak Holl, M. M.; Baker, J. R. *Eur. J. Med. Chem.* **2012**, *47*, 560–572.

[66] Leroueil, P. R.; Berry, S. A.; Duthie, K.; Han, G.; Rotello, V. M.; McNerny, D. Q.; Baker, J. R.; Orr, B. G.; Holl, M. M. *Nano Lett.* **2008**, *8*, 420–424.

[67] Jain, K.; Kesharwani, P.; Gupta, U.; Jain, N. K. *Int. J. Pharm.* **2010**, *394*, 122–142.

[68] Lakamper, S.; Kallipolitou, A.; Woehlke, G.; Schliwa, M.; Meyhofer, E. *Biophys. J.* **2003**, *84*, 1833–1843.

[69] Hiller, G.; Weber, K. *Cell* **1978**, *14*, 795–804.

[70] Van de Water, r., L.; Olmsted, J. B. *J. Biol. Chem.* **1980**, *255*, 10744–10751.

[71] Parness, J.; Horwitz, S. B. *J. Cell Biol.* **1981**, *91*, 479–487.

[72] Gaskin, F.; Cantor, C. R.; Shelanski, M. L. *J. Mol. Biol.* **1974**, *89*, 737–755.

[73] Hyman, A. A.; Salser, S.; Drechsel, D. N.; Unwin, N.; Mitchison, T. J. *Mol. Biol. Cell* **1992**, *3*, 1155–1167.

[74] Ross, J. L.; Fygenson, D. K. *Biophys. J.* **2003**, *84*, 3959–3967.

[75] Odde, D. *Eur. Biophys. J.* **1998**, *27*, 514–520.

[76] Diaz, J. F.; Valpuesta, J. M.; Chacon, P.; Diakun, G.; Andreu, J. M. *J. Biol. Chem.* **1998**, *273*, 33803–33810.

[77] Magnani, M.; Maccari, G.; Andreu, J. M.; Diaz, J. F.; Botta, M. *FEBS J* **2009**, *276*, 2701–12.

[78] Diaz, J. F.; Strobe, R.; Engelborghs, Y.; Souto, A. A.; Andreu, J. M. *J Biol Chem* **2000**, *275*, 26265–76.

[79] Nogales, E.; Wolf, S. G.; Khan, I. A.; Luduena, R. F.; Downing, K. H. *Nature* **1995**, *375*, 424–7.

[80] Diallo, M. S.; Christie, S.; Swaminathan, P.; Balogh, L.; Shi, X.; Um, W.; Papelis, C.; Goddard, r., W. A.; Johnson, J., J. H. *Langmuir* **2004**, *20*, 2640–2651.

[81] Jordan, M. A.; Wendell, K.; Gardiner, S.; Derry, W. B.; Copp, H.; Wilson, L. *Cancer Res.* **1996**, *56*, 816–825.

[82] Walczak, C. E.; Shaw, S. L. *Cell* **2010**, *142*, 364–367.

[83] Nogales, E.; Whittaker, M.; Milligan, R. A.; Downing, K. H. *Cell* **1999**, *96*, 79–88.

[84] Gaertig, J.; Wloga, D. *Curr. Biol.* **2012**, *22*, R483–R485.

[85] Shida, T.; Cueva, J. G.; Xu, Z.; Goodman, M. B.; Nachury, M. V. *Proc. Natl. Acad. Sci. U. S. A.* **2010**, *107*, 21517–21522.

[86] Chretien, D.; Metoz, F.; Verde, F.; Karsenti, E.; Wade, R. H. *J. Cell Biol.* **1992**, *117*, 1031–1040.

[87] Chretien, D.; Wade, R. H. *Biol. Cell* **1991**, *71*, 161–174.

[88] Ray, S.; Meyhofer, E.; Milligan, R. A.; Howard, J. *J. Cell Biol.* **1993**, *121*, 1083–1093.

[89] Hamon, L.; Savarin, P.; Curmi, P. A.; Pastre, D. *Biophys. J.* **2011**, *101*, 205–216.

[90] Mecke, A.; Lee, I.; Baker, J. R.; Holl, M. M. B.; Orr, B. G. *Eur. Phys. J. E: Soft Matter Biol. Phys.* **2004**, *14*, 7–16.

[91] Regula, C. S.; Pfeiffer, J. R.; Berlin, R. D. *J. Cell Biol.* **1981**, *89*, 45–53.

[92] Skiniotis, G.; Cochran, J. C.; Muller, J.; Mandelkow, E.; Gilbert, S. P.; Hoenger, A. *EMBO J.* **2004**, *23*, 989–999.

[93] Thomas, T. P.; Majoros, I.; Kotlyar, A.; Mullen, D.; Holl, M. M. B.; Baker, J. R. *Biomacromolecules* **2009**, *10*, 3207–3214.

[94] Card, J. W.; Jonaitis, T. S.; Tafazoli, S.; Magnuson, B. A. *Crit. Rev. Toxicol.* **2011**, *41*, 20–49.

[95] Clift, M. J. D.; Gehr, P.; Rothen-Rutishauser, B. *Arch. Toxicol.* **2011**, *85*, 723–731.

[96] Hubbs, A. F.; Mercer, R. R.; Benkovic, S. A.; Harkema, J.; Sriram, K.; Schwegler-Berry, D.; Goravanahally, M. P.; Nurkiewicz, T. R.; Castranova, V.; Sargent, L. M. *Toxicol. Pathol.* **2011**, *39*, 301–324.

[97] Oberdorster, G.; Stone, V.; Donaldson, K. *Nanotoxicology* **2007**, *1*, 2–25.

[98] Mahmoudi, M.; Lynch, I.; Ejtehadi, M. R.; Monopoli, M. P.; Bombelli, F. B.; Laurent, S. *Chem. Rev.* **2011**, *111*, 5610–5637.

[99] Cline, E. N.; Li, M. H.; Choi, S. K.; Herbstman, J. F.; Kaul, N.; Meyhofer, E.; Skiniotis, G.; Baker, J. R.; Larson, R. G.; Walter, N. G. *Biomacromolecules* **2013**, *14*, 654–664.

[100] Alsop, G. B.; Zhang, D. *J Cell Biol* **2003**, *162*, 383–90.

[101] Kanai, Y.; Takemura, R.; Oshima, T.; Mori, H.; Ihara, Y.; Yanagisawa, M.; Masaki, T.; Hirokawa, N. *J Cell Biol* **1989**, *109*, 1173–84.

[102] Goodman, J.; Walsh, V. *The story of taxol : nature and politics in the pursuit of an anti-cancer drug*; Cambridge University Press: Cambridge ; New York, 2001.

[103] Wani, M. C.; Taylor, H. L.; Wall, M. E.; Coggon, P.; McPhail, A. T. *J Am Chem Soc* **1971**, *93*, 2325–7.

[104] Schiff, P. B.; Fant, J.; Horwitz, S. B. *Nature* **1979**, *277*, 665–7.

[105] Parveen, S.; Misra, R.; Sahoo, S. K. *Nanomedicine* **2012**, *8*, 147–66.

[106] Vigderman, L.; Zubarev, E. R. *Adv Drug Deliv Rev* **2012**,

[107] Brahmachari, B.; Hazra, A.; Majumdar, A. *Indian J Pharmacol* **2011**, *43*, 126–30.

[108] Kumar, A.; Zhang, X.; Liang, X. J. *Biotechnol Adv* **2012**,

[109] Duncan, B.; Kim, C.; Rotello, V. M. *J Control Release* **2010**, *148*, 122–7.

[110] Dreaden, E. C.; Austin, L. A.; Mackey, M. A.; El-Sayed, M. A. *Ther Deliv* **2012**, *3*, 457–78.

[111] Doane, T. L.; Burda, C. *Chem Soc Rev* **2012**, *41*, 2885–911.

[112] Turner, P. F.; Margolis, R. L. *J Cell Biol* **1984**, *99*, 940–6.

[113] Zhao, H.; Yang, S.; You, H.; Wu, Y.; Ding, B. *Geen Chem.* **2012**, *14*, 3197–3203.

[114] Berkovitch, N.; Ginzburg, P.; Orenstein, M. *Nano Lett* **2010**, *10*, 1405–8.

[115] Finkelstein, I. J.; Greene, E. C. *Methods Mol Biol* **2011**, *745*, 447–61.

[116] Gorman, J.; Plys, A. J.; Visnapuu, M. L.; Alani, E.; Greene, E. C. *Nat Struct Mol Biol* **2010**, *17*, 932–8.

[117] Gorman, J.; Chowdhury, A.; Surtees, J. A.; Shimada, J.; Reichman, D. R.; Alani, E.; Greene, E. C. *Mol Cell* **2007**, *28*, 359–70.

[118] Finkelstein, I. J.; Visnapuu, M. L.; Greene, E. C. *Nature* **2010**, *468*, 983–7.

[119] Vitreschak, A. G.; Rodionov, D. A.; Mironov, A. A.; Gelfand, M. S. *Trends Genet* **2004**, *20*, 44–50.

[120] Garst, A. D.; Batey, R. T. *Biochim Biophys Acta* **2009**, *1789*, 584–91.

[121] Blount, K. F.; Breaker, R. R. *Nat Biotechnol* **2006**, *24*, 1558–64.

[122] Eid, J. et al. *Science* **2009**, *323*, 133–8.

[123] Draganescu, A.; Hodawadekar, S. C.; Gee, K. R.; Brenner, C. *J Biol Chem* **2000**, *275*, 4555–60.

[124] Korlach, J.; Baird, D. W.; Heikal, A. A.; Gee, K. R.; Hoffman, G. R.; Webb, W. W. *Proc Natl Acad Sci U S A* **2004**, *101*, 2800–5.